~~Radiative effect by~~ Sensitivity of cirrus and contrail radiative effect on cloud microphysical and ~~contrails – A comprehensive sensitivity study~~environmental parameters.

Kevin Wolf[1], Nicolas Bellouin[1,2], and Olivier Boucher[1]

[1]Institut Pierre-Simon Laplace, Sorbonne Université / CNRS, Paris, France
[2]Department of Meteorology, University of Reading, Reading, United Kingdom

Correspondence: Kevin Wolf (kevin.wolf@ipsl.fr)

Abstract. Natural cirrus clouds and contrails cover about 30% of the Earth's mid-latitudes and up to 70% of ~~its~~ the Tropics. Due to their widespread occurrence, cirrus have a considerable impact on the Earth energy budget, which, on average, leads to a warming net radiative effect (solar + thermal-infrared). However, whether the instantaneous radiative effect (RE), which in some cases corresponds to a radiative forcing, of natural cirrus or contrails is positive or negative depends on their microphysical, macrophysical, and optical properties, as well as the radiative properties of the environment. This is further complicated by the fact that the actual ice crystal shape is often unknown and thus ice clouds remain one of the components that are least understood in the Earth's radiative budget.

The present study aims to ~~separate~~ investigate the dependency of the effect on cirrus RE ~~of~~ on eight parameters: solar zenith angle, ice water content, ice crystal effective radius, cirrus temperature, surface albedo, surface temperature, ~~liquid water~~ cloud optical thickness of an underlying liquid water cloud, and three ice crystal shapes. In total, ~~94~~283,500 radiative transfer simulations have been performed, spanning the parameter ranges that are typically associated with natural cirrus and contrails. In addition, the effect of variations in the relative humidity profile and the ice cloud geometric thickness have been investigated for a sub-set of the simulations. The multi-dimensionality and complexity of the 8-dimension parameter space makes it impractical to discuss all potential configurations in detail. Therefore, specific cases are selected and discussed.

~~The ice~~ Ice crystal effective radius has the largest impact on solar, thermal-infrared (TIR), and net RE. The second most important parameter is ~~the~~ ice water content, which equally impacts the solar and terrestrial RE~~equally~~. Solar and TIR RE have opposite signs, meaning that the ice water content has a relatively small impact on net RE. ~~Beyond the ice crystal effective radius and the ice water content, the solar~~ Solar RE of cirrus is also determined by solar zenith angle, surface albedo, liquid cloud optical thickness, and ~~the~~ ice crystal shape in descending priority. RE in the TIR spectrum is dominated by ~~the~~ surface temperature, ~~the~~ ice cloud temperature, ~~the~~ liquid water cloud optical thickness, and ~~the~~ ice crystal shape. Net RE is controlled by ~~the~~ surface albedo, ~~the~~ solar zenith angle, and ~~the surface albedo~~ surface temperature in decreasing importance. The relative importance of the studied parameters differs depending on the ambient conditions and during nighttime the net RE is equal to the TIR RE.

The data set generated in this work is publicly available. It can be used ~~to compute the radiative effect~~ as a look-up-table to extract the RE of cirrus clouds, contrails, and contrail cirrus instead of full radiative transfer calculations.

1 Introduction

Cirrus clouds cover large areas of the Earth, with cloud cover estimates of 30 % in the mid-latitudes and up to 70 % in the tropics (Liou, 1986; Wylie and Menzel, 1999; Chen et al., 2000; Sassen et al., 2008; Nazaryan et al., 2008). Due to their widespread occurrence, cirrus can have a considerable impact on the global energy budget. In addition to cirrus, air traffic leads to the formation of condensation trails, also termed contrails, which are optically and geometrically geometrically and optically thin clouds with similar radiative effects as thin natural cirrus (Liou, 1986). For the sake of simplicity, the term cirrus is used interchangeably for natural cirrus, contrail-induced cirrus, and contrails throughout this article.

Depending on ambient conditions, contrails are short lived (t < 10 min) but can persist up to a day when the surrounding air mass is sufficiently cold and moist (Jensen et al., 1994; Schumann, 1996; Haywood et al., 2009)(Schumann, 1996; Haywood et al., 2009; S . In such conditions, persistent contrails transition from line-shaped clouds to larger cloud fields (Unterstrasser and Stephan, 2020). Modeling and satellite studies have estimated that contrail and contrail-induced cirrus cloud cover can reach up to 6 to 10 % over Europe (Burkhardt and Kärcher, 2011; Quaas et al., 2021) and significantly contribute to high-level cloudiness over Europe (Schumann et al., 2015, 2021).

Under most circumstances cirrus have a cooling effect in the solar wavelength range (0.2–3.5 μm, sometimes called shortwave) and a heating effect in the thermal-infrared (TIR) wavelength range (3.5–100 μm, sometimes also termed longwave or terrestrial). The net radiative effect (solar cooling + TIR warming) is often a warming as the TIR effect dominates (Chen et al., 2000). By combining satellite observations and radiative transfers transfer (RT) simulations, Chen et al. (2000) estimated a global annual mean cirrus cloud radiative effect (RE) of -25.3 W m^{-2} in the solar wavelength range and 30.7 W m^{-2} in the TIR wavelength range, leading to a positive net effect of 5.4 W m^{-2}. However, whether the instantaneous RE of natural cirrus or contrails is positive or negative depends on their microphysical, macrophysical, and optical, as well as radiative properties of the environment. The cloud properties relevant to the RE of the cloud are primarily cloud altitude, cloud temperature, ice water content, ice crystal shape (also called crystal habit), and the orientation of the ice crystals (Fu and Liou, 1993; Stephens et al., 2004; Campbell et al., 2016). Furthermore, the underlying surface properties, i.e., surface albedo and surface temperature, as well as gaseous absorption and additional underlying cloud layers, also have an effect on the cirrus RE. Dynamical processes in the atmosphere have a strong influence on those parameters, for example lifting of air masses along warm conveyor belts or cloud anvils, that lead to a variety of ice crystal shapes and crystal surface roughness (Freudenthaler et al., 1996; Wendisch et al., 2007; Yang et al., 2010; Krämer et al., 2016; Luebke et al., 2016). As a result, the actual distribution of crystal shapes within a cirrus and the related RE are often unclear. Thus ice clouds remain one of the components that are is least understood in the Earth's radiative budget (Stevens and Bony, 2013; Bauer et al., 2015; Bickel et al., 2020) and this lack of understanding contributes to uncertainties in the climate impact of aviation (Lee et al., 2021).

To estimate the radiative impact of a cloud as well as related potential uncertainties and sensitivities, RT simulations represent a helpful tooldespite their complexity as in the case of ice clouds. While the atmospheric RT in liquid water clouds composed of spherical cloud droplets can rely on geometric optics or Mie-scattering theory (Mie, 1908; van de Hulst, 1981), RT simulations in ice clouds are made complicated by the non-spherical shape of ice crystals. The way non-spherical crystals

~~interact with~~ crystal shape and the interaction with incoming radiation, i.e., through their single-scattering phase function. The single-scattering phase function, for example, has to be determined by computationally-expensive methods, like ray tracing (Bi et al., 2014), Monte Carlo simulations ~~(Macke et al., 1996b, a)~~(Macke et al., 1996a, b), or the T-matrix method (Mishchenko, 2020). Due to the computational burden of such accurate simulations, ~~approximations, i.e., ice crystal parameterizations of radiative properties ,~~ parameterizations of ice crystal properties are often developed and validated against the more precise calculations (Takano and Liou, 1989; Fu, 1996; Yang et al., 2000, 2013). More recent ice crystal parameterizations by Yang et al. (2000), ~~?~~Baum et al. (2005a, b), Baum et al. (2007), and Yang et al. (2013) in combination with the latest RT models allow to determine the radiative impact of cirrus clouds with acceptable computational cost and accuracy. By varying the microphysical and macrophysical properties of the cirrus, as well as the surface properties in the RT model, the natural range of cirrus and their environment can be represented and the RE can be estimated. Furthermore, uncertainties due to the insufficiently known crystal shape can be assessed.

Multiple studies that aimed to investigate the impact of a certain parameter ~~, like the crystal size distribution, on the~~ on cloud RE have been performed in the past. Fu and Liou (1993) as well as Yang et al. (2010) focused on the effects of the selected ice crystal habit and ~~the~~ ice water path. The effect of the ice crystal size ~~was analyzed by Zhang et al. (1999), while Mitchell et al. (2011)looked into the implications of the crystal size distribution~~distribution was analyzed, for example, by Zhang et al. (1999) or Mitchell et al. (2011). A comprehensive study of cirrus radiative effects was conducted by Schumann (2012), who aimed to derive ~~an approximate model~~ a parameterization to estimate the cloud RE. While those studies are valuable, none of them ~~presents a comprehensive sensitivity study across all~~ investigate the effect of multiple factors, like relevant cloud and environmental input parameters.

~~Therefore, we present a study that separates the effect of eight selected parameters on the cirrus RE~~These studies have identified parameters that affect cirrus RE, but all these parameters need to be considered together, including both cloud and environmental parameters. This article is intended as a parametric sensitivity study ~~and~~ that aims to compare the effects of ~~different input parameterswith different units and value ranges. We sample~~ major parameters. Furthermore, we identify the driving parameters of RE by sampling the input parameter range, restricted to values that are typically associated with ice clouds~~, to identify the relative importance of the different input parameters. Furthermore, we aim to~~ . Finally, we provide an open-access data set, which allows the user to extract cloud REs for user-specific combinations of the input parameters. The data set might be coupled with cloud microphysical models, e.g, the Contrail Cirrus Prediction Tool (CoCiP) from Schumann (2012) , to estimate the RE of the simulated contrails.

The study is structured in the following way. Section 2 introduces the selected parameter space, the RT model, and outlines basic definitions as well as methods used in the paper. Subsequently, Section 3 presents the results from the RT simulations. Because our simulations assume plane-parallel atmosphere and homogeneous clouds, Section 4 discusses 3-dimensional RT. That is followed by the summary in Sec. 5.

2 Methods and Definitions

2.1 ~~Concept~~ Definition of radiative effect and albedo

The radiative impact of ~~any~~ a perturbation, e.g., clouds, is quantified by the concept of the radiative effect~~(RE)~~. The RE is defined as the net difference in downward and upward irradiance ($F^{\downarrow} - F^{\uparrow}$) between the perturbed and unperturbed condition. In the case of clouds, the cloud radiative effect (CRE, denoted here as ΔF) is the difference in fluxes between the ~~cirrus~~ cloud (F_{c}) and ~~cirrus-free~~ cloud-free (F_{cf}) atmosphere at a given altitude z (Ramanathan et al., 1989; Stapf et al., 2021; Luebke et al., 2022):

$$\Delta F(z) = F_{\mathrm{c}}(z) - F_{\mathrm{cf}}(z) = \left[F^{\downarrow}(z) - F^{\uparrow}(z)\right]_{\mathrm{c}} - \left[F^{\downarrow}(z) - F^{\uparrow}(z)\right]_{\mathrm{cf}}, \tag{1}$$

where the upward and downward~~irradiances are both~~, cloudy and cloud-free irradiances are all counted positive. The net RE given by:

$$\Delta F_{\mathrm{net}}(z) = \Delta F_{\mathrm{sol}}(z) + \Delta F_{\mathrm{TIR}}(z), \tag{2}$$

which can can be split into a solar ~~:~~

$$\Delta F_{\mathrm{sol}}(z) = \left[F^{\downarrow}_{\mathrm{sol}}(z) - F^{\uparrow}_{\mathrm{sol}}(z)\right]_{\mathrm{c}} - \left[F^{\downarrow}_{\mathrm{sol}}(z) - F^{\uparrow}_{\mathrm{sol}}(z)\right]_{\mathrm{cf}}$$

and a thermal-infrared component~~:~~

$$\Delta F_{\mathrm{tir}}(z) = \left[F^{\downarrow}_{\mathrm{tir}}(z) - F^{\uparrow}_{\mathrm{tir}}(z)\right]_{\mathrm{c}} - \left[F^{\downarrow}_{\mathrm{tir}}(z) - F^{\uparrow}_{\mathrm{tir}}(z)\right]_{\mathrm{cf}}.$$

. Within this study, the CRE is calculated for the top of atmosphere (TOA)~~at 15 kmif not~~, which is set in the radiative transfer calculations to an altitude of 120 km, which is set in the RT calculations to an altitude of 120 km, unless stated otherwise.

In addition to the RE, the albedo α describes the interaction of a ~~cloud~~ cloudy scene or a surface with the solar, incident radiation. The scene albedo ~~$\alpha(\lambda)$~~ $\alpha_{\mathrm{sol}}(z = TOA)$ at the TOA is defined as the ratio of the reflected, upward irradiance ~~$F^{\uparrow}$~~ $F^{\uparrow}_{\mathrm{sol}}$ at TOA in relation to the incident, downward irradiance ~~$F^{\downarrow}$~~ $F^{\downarrow}_{\mathrm{sol}}$ at TOA and is given by:

$$\alpha(\lambda)_{\mathrm{sol,TOA}} = \frac{F^{\uparrow}(\lambda)}{F^{\downarrow}(\lambda)} \frac{F^{\uparrow}_{\mathrm{sol}}(z = \mathrm{TOA})}{F^{\downarrow}_{\mathrm{sol}}(z = \mathrm{TOA})}. \tag{3}$$

~~The scene albedo depends on the surface albedo that varies spectrally. Nevertheless, the spectral variation of the surface albedo is kept constant in this study. In the TIR wavelength range α_{srf} is assumed to be~~ Similarly, the surface albedo $\alpha_{\mathrm{sol,srf}}$ is calculated with $F^{\uparrow}_{\mathrm{sol,srf}}$ and $F^{\downarrow}_{\mathrm{sol,srf}}$ the respective irradiances at the surface ($z =$ 0~~, which leads to an emissivity $\epsilon = 1$ with the Earth's surface thus acting as a blackbody (Wilber, 1999)~~ km).

2.2 Radiative transfer simulation set-up

Upward and downward irradiances $F^{\uparrow}$ / $F^{\downarrow}$ were simulated with the library for Radiative transfer (libRadtran, Emde et al., 2016). The solar irradiances F_{sol} cover a wavelength range from 0.3 to 3.5 μm, which represents 97.7 % of the total incoming solar radiation (0–10 μm) calculated from the spectrum providede by Kurucz (1992). The TIR irradiances include wavelengths from 3.5 to 75 μm, representing 99.3 % of the integrated blackbody radiation (3.5 to 100 μm) at 285 K (12°C). ~~libRadtran was run as a one-dimensional (1D) RT solver in which clouds are uniform on the horizontal~~

The RT simulations are performed with the 1D solver DISORT (Buras et al., 2011), which is part of libRadtran. Clouds are assumed to be horizontally uniform and lateral photon transport between columns is ~~not considered. This approximation is called~~ neglected, which is called the independent pixel approximation (IPA, Stephens et al., 1991; Cahalan et al., 1994). ~~We regard 1D simulations as appropriate as we focus on~~ As the main objective of this study is to map the basic dependencies of ΔF on the driving parameters, we neglect any variability in the spatial ice water content (IWC) distribution that exists in cirrus (Minnis et al., 1999). We also ~~restrain~~ restrict the simulations to fully cloud covered scenes. ~~Irradiances are therefore calculated with the Discrete Ordinate Radiative Transfer model (DISORT) 2.0 solver by Stamnes et al. (2000).~~ The required number of streams was iteratively determined and set to 16 streams, which provides sufficient accuracy while limiting computational time. The trade-off between accuracy and computational time is detailed in Appendix C. The spectral TOA solar irradiance is provided by Kurucz (1992). The RT simulations consider molecular absorption using the ~~medium~~ 'coarse' resolution REPTRAN parameterization from Gasteiger et al. (2014). Absorption by water vapor, carbon dioxide, ozone, nitrous oxide, carbon monoxide, methane, oxygen, and nitrogen and nitrogen dioxide is included in the simulations (Anderson et al., 1986; Emde et al., 2016).

The sensitivity of solar, TIR, and net cloud RE ΔF is estimated by varying eight parameters. The parameter ranges were chosen to represent commonly observed cirrus ~~,~~ and contrail cirrus properties, ~~and environment~~ as well as environmental parameters.

- The daily course of the Sun position is represented by solar zenith angles θ ranging from 0° and ~~70~~85°. Larger θ values are omitted to avoid numerical instability that would require more streams in the calculation. Furthermore, RT simulations with the DISORT solver for $\theta > 85°$ have to be interpreted with caution as DISORT does not consider the sphericity of the Earth and treats atmospheric layers as plane-parallel (Stamnes et al., 2000; Buras et al., 2011). In addition, the deviations and biases between 1D and 3D RT simulations increase significantly with values of up to 40 % (Gounou and Hogan, 2007; Forster et al., 2012).

- The Earth's surface albedo, ~~α_{srf}~~ α_{srf} ranges from 0 to 1, which represents the full possible range. ~~Therefore, the α_{srf} in the solar wavelengthrange is varied from~~ In general, α_{srf} varies spectrally but here is kept constant for all solar wavelength. It is varied between 0 ~~to~~ and 1 to include surface conditions ranging from open ocean ~~over marginal sea ice zones to domains with~~ to full sea ice or snow ~~cover. (Baldridge et al., 2009; Gardner and Sharp, 2010; Meerdink et al., 2019; Gueyma~~ ~~.~~ (Baldridge et al., 2009; Gardner and Sharp, 2010; Meerdink et al., 2019; Gueymard et al., 2019). Values of α_{srf} are given

Table 1. Cirrus Surface temperature, cloud top temperature, cloud top altitude, and cloud top pressure level at 223, 233, of the liquid water and 243 K ice water cloud depending on the surface temperature and associated atmosphere profile.

Cirrus US Standard Tropical	Subarctic winter	Profiles	
temperature	US Standard (`afglus`)	Tropical (`afglt`)	Subarctic winter (`afglsw`)
223Surface temperature	288 K (-5015°C)	10.0 km | 260 hPa 300 K (27°C)	258 K (-15°C)
Cirrus pressure (hPa) / altitude (km)		12.1 km | 210 hPa	7.6 km| 350 hPa
233219 K (-40−54°C)	10.7 / 240	12.7 / 191	8.5 km | 333 hPa / 308
225 K (−48°C)	10.6 km | 263 hPa 9.7 / 276	6.2 km | 437 hPa 11.8 / 220	7.3 / 367
231 K (−42°C)	8.8 / 318	10.9 / 252	6.5 / 419
237 K (−36°C)	7.9 / 363	10.0 / 286	5.6 / 476
243 K (-30−30°C)	7.0 km | / 414 hPa	9.0 km | 9.1 / 325 hPa	4.7 km | 540 hPa / 540
Cloud top temperature (°C / K) for liquid cloud at 1.5 km	278.5 K / 5.4°C	290.7 K / 17°C	257.5 K / −15.7°

in Table 4. In the TIR wavelength range α_{srf} is assumed to be 0, which leads to an emissivity $\epsilon = 1$ with the Earth's surface thus acting as a blackbody (Wilber, 1999).

– The surface temperature T_{srf} is set to -40°C, 0°C, and 40°C representing ArcticThree atmospheric profiles (AP) are selected to represent subarctic, mid-latitude, and tropical or desert conditions, respectively. The atmospheric profiles are selected depending on T_{srf} using conditions. The simulations are based on the subarctic winter (`afglsw`, $T_{\mathrm{srf}} = 273$ K),), the US standard (`afglus`), and the tropical (`afglt`,) profile after Anderson et al. (1986). Surface temperatures T_{srf} = 313 K), or the US standard(`afglus`, elsewhere)profiles after Anderson et al. (1986). Directly related to different temperature profiles is a variation in the relative humidity profile, which primarily impacts are set to -15.8°C (subarctic winter), 15.05°C (US standard), and 26.5°C (tropical), respectively, to match the lower most temperature in the APs. The profile of relative humidity is linked to the AP via the Clausius–Clapeyron-equation (Corti and Peter, 2009). Variations in the water vapor (WV) profile primarily impact the RT in the TIR wavelength rangebut also, to a minor extent, , particularly in WV absorption bands, while RT in the solar wavelength range by water vapor absorption. This effect is not separated from the temperature variationis less affected (Liou, 1992). The altitude of the cirrus cloud base depends on the selected atmosphere profile (T_{srf}) and the selected cirrus temperatures $T_{\mathrm{cld,ice}}$. cirrus cloud top temperatures $T_{\mathrm{cld,ice}}$ are selected to span the temperature range in which contrails and cirrus typically form (Krämer et al., 2020). The resulting cirrus cloud base is Here we cover a range from 219 to 243 K. The resulting ice cloud top altitudes $z_{\mathrm{ice,CT}}$ are set to the altitude, where the temperature of the profile in the APs equals the desired $T_{\mathrm{cld,ice}}$. The cloud geometric thickness Δz is not varied in this study and set to 0.2 km. Cirrus temperatures and related cirrus base altitudes $z_{\mathrm{ice,CT}}$ are listed in Table 1. Within the simulations, the ice cloud geometric thickness dz is set to 1000 m for all simulations, which represents an average for observed contrails as well as natural cirrus (Freudenthaler et al., 1995; Sassen and Campbell, 2001; Noël and Haeffelin, 2 . Meerkötter et al. (1999) reported that variations in $\mathrm{d}z$ have only a minor impact on the cloud RE. However, to check this we performed a dedicated sensitivity study on $\mathrm{d}z$ for a sub-set of the parameter range.

– Three different ice crystal shapes~~are considered in this study. The tables after Yang et al. (2000) are selected among the available set of ice optics parameterizations in libRadtran.'Rough-aggregates' were chosen~~ , namely: 'rough-aggregates', agglomerations of columnar ice crystals with a rough surface; 'droxtals', almost spherical ice crystals; and 'plates' are used. These three shapes are selected to represent different stages in the temporal evolution of contrails. Several airborne in-situ measurement campaigns that targeted cirrus and contrails imply that aggregates are the dominating ice crystal habit (Liu et al., 2014; Holz et al., 2016; Järvinen et al., 2018). For example, Järvinen et al. (2018) found that 61 to 81 % of the sampled ice crystals were rough aggregates. 'rough-aggregates' are also assumed in current remote sensing applications of ice cloud, e.g., in the re-defined ice optical properties used by the Moderate Resolution Imaging Spectroradiometer (MODIS) Collection 6 product (Yang et al., 2013; Holz et al., 2016; Platnick et al., 2017). Therefore, 'rough-aggregates', are selected as the primary ice crystal habit. The ~~ice parameterization is assumed to represent complex-shaped, non-spherical ice crystals that can be found in aged contrails and cirrus. In addition, 'plate' -like ice crystals with a characteristic single-scattering phase function $\mathcal{P}$ were also considered. To~~ second most observed habit are plate-like ice crystals (Holz et al., 2016; Forster et al., 2017; Järvinen et al., 2018). Furthermore, Forster and Mayer (2022) used ground-based halo observations and found that cirrus are frequently comprised of mixtures of 'rough-aggregates' and 'plates'. Therefore, plate-like ice crystals are included as a second shape. The 'droxtal' parameterization is selected to estimate ΔF of young contrails, which primarily consist of near-spherical ice crystals (Goodman et al., 1998; Lawson et al., 1998; Gayet et al., 2012)~~, the 'droxtal' parameterization after Yang et al. (2013) was added as a third choice. The three different ice habits can be interpreted as representing different stages in the temporal evolution of contrails.~~ . We emphasize that contrails can be comprised of other ice crystal shapes, like single columns, hollow columns, 3D bullet rosettes, or mixtures of these (Lawson et al., 1998; Baum et al., 2005a), but the simulated shapes cover the majority of observed cirrus situations. The utilized ice optical properties of the three selected shapes are based on the parameterization from Yang et al. (2013) that assume randomly oriented ice crystals with a 'moderate' surface roughness.

– Within libRadtran clouds are defined by their geometric thickness $\mathrm{d}z$, effective radius r_{eff}, and IWC. Typical IWC of contrails and in situ cirrus can range from 10^{-5} to $0.2\ \mathrm{g\,m^{-3}}$ as found during the Mid–Latitude Cirrus campaign (Luebke et al., 2016; Krämer et al., 2016, 2020). For our simulations, we span a similar range of IWC from $7 \cdot 10^{-7}$ to $0.1\ \mathrm{g\,m^{-3}}$.

– Aircraft in situ observations of young ($t < 120$ s) contrails showed that these consist of ice crystals with diameters up to a few micrometers (Petzold et al., 1997; Sassen, 1997; Lynch et al., 2002). Shortly thereafter these ice crystals grow in size and reach ice crystal radius r_{eff} between 2 and 5 μm (Jeßberger et al., 2013; Bräuer et al., 2021). The majority of ice crystals in older ($t > 120$ s) contrails and cirrus have r_{eff} between 10 and 150 μm (Krämer et al., 2020), while ~~developed~~

mature cirrus can be composed of ice crystals with diameters larger than 150 μm (Schröder et al., 2000). The conducted simulations cover only the lower selected ice optical properties allow for simulations between 5 to 85 μm and thus cover the lower and mid range of the natural crystal size spectrumdue to limitation in the provided ice optics parameterizations. Our simulations range from 5 to 45 μm for all three shapes and, therefore, focus on young contrails and cirrus.

The Within libRadtran the bulk-scattering properties of ice clouds are obtained by integrating the single-scattering properties over the entire ice crystal / particle size distribution (PSD)is defined such that $n(r)\mathrm{d}r$ represents the number of cloud droplets or ice crystals in a cloud with a size between r and $r+\mathrm{d}r$. The PSD of liquid water and ice clouds is typically represented an ice cloud can be approximated by a gamma distribution of the form:

$$n(r) = N_0 \cdot r^{\mu} \cdot \exp\left(-\Lambda \cdot r\right),$$

(Hansen and Travis, 1974; Evans, 1998; Heymsfield et al., 2002; Baum et al., 2005a, b), which is given by:

$$n(r_\mathrm{e}) = N \cdot r_\mathrm{e}^{\mu} \cdot \exp\left(-\Lambda \cdot r_\mathrm{e}\right), \quad (4)$$

e.g., by Hansen and Travis (1974) or Petty and Huang (2011). N_0 is a constant factor, which with $n(r_\mathrm{e})\mathrm{d}r$ the number of ice crystals with radii in the range of r_e and $r_\mathrm{e}+\mathrm{d}r$. N is a normalization constant such that the integral over the PSD yields the number of crystals in a unit volume (Emde et al., 2016). N itself results from the choice of the parameters in Eq. 4 that are given by the slope Λ and dispersion μ by:

$$\Lambda = \frac{1}{r_\mathrm{eff} \cdot \nu_\mathrm{eff}}; \mu = \frac{1 - 3 \cdot \nu_\mathrm{eff}}{\nu_\mathrm{eff}}$$

(Deirmendjian, 1962; Petty and Huang, 2011). The calculation of ν_eff is detailed in $\Lambda = -\frac{1}{a \cdot b}$ and dispersion $\mu = \frac{1-3b}{b}$. Inserting a and b into Eq. 15 of the paper by Petty and Huang (2011)4 leads to:

$$n(r_\mathrm{e}) = N \cdot r_\mathrm{e}^{\left(\frac{1}{b}-3\right)} \cdot \exp\left(-\frac{r}{ab}\right), \quad (5)$$

Parameter b corresponds to the effective variance ν_eff (unitless), with typical values between 0.1 and 0.5 (Evans, 1998; Heymsfield et a . In libRadtran , μ ν_eff is set to unity, while N_0 and μ are found iteratively such that the PSD yields the mean r_eff (Emde et al., 2016).

0.25 (Emde et al., 2016). Parameter a corresponds to the targeted effective radius r_eff of the particle size distributions. Multiple definitions for the effective crystal radius r_eff exist in the case of non-spherical crystals. Here we follow the definition from Yang et al. (2000), Key et al. (2002), and ?Baum et al. (2007)Baum et al. (2005b), Baum et al. (2007), and Schumann et al. (2011), which describe D_eff and r_eff the diameter D_e and radius r_e of a non-spherical ice crystal population as: as:

$$D_\mathrm{e} = 2 \cdot r_\mathrm{e} = \frac{D_\mathrm{V}^3}{D_\mathrm{A}^2}, \quad (6)$$

with D_V the diameter of a spherical crystal with the same average volume as the ice crystal and D_A the diameter of a spherical crystal with the same projected area as the ice crystal. D_A is defined by:

$$D_\mathrm{A} = 2 \cdot r_\mathrm{A} = 2 \cdot \left(\frac{A}{\pi}\right)^{1/2} \tag{7}$$

and D_V is given by:

$$D_\mathrm{V} = 2 \cdot r_\mathrm{V} = \left(\frac{6 \cdot V}{\pi}\right)^{1/3}, \tag{8}$$

where V and A are the ~~average volume and~~ volume and the mean projected area of the ~~crystal population~~ice crystal, respectively. ~~In practical application, the relationship between r_eff and D_A as well as D_V is derived from in situ observations for a given crystal shape.~~ As demonstrated by Mitchell (2002) the definition of D_e and r_e of a single crystal can be applied to a PSD, when evaluated at a bulk ice density of 917 kg m^{-3}, which finally leads to:

$$r_\mathrm{eff} = \frac{3 \cdot \int_{L1}^{L2} V(L) n(L) \mathrm{d}L}{4 \cdot \int_{L1}^{L2} A(L) n(L) \mathrm{d}L}, \tag{9}$$

with $L1$ and $L2$ the minimum and maximum crystal size of the distribution.

The original ice optical properties from ~~Yang et al. (2000) and Yang et al. (2013) are post-processed~~ Yang et al. (2013) are processed by weighting the size dependent single-scattering phase function with the gamma distribution (Emde et al., 2016). For the gamma size distribution a minimum and maximum r_eff of 5 and 90 μm are selected. Parameter a in Eq. 5 is found iteratively such that the desired r_eff of the distribution is achieved. The obtained bulk optical properties are used for RT in the solar and the TIR wavelength range. Examples of phase functions $\mathcal{P}$ for four different crystal shapes and their characteristic features are visualized in Appendix D.

– ~~Within libRadtran clouds are defined by their geometric thickness Δz, r_eff, and ice water content IWC. Typical IWC of contrails and in situ cirrus can range from 10^{-5} to 0.2 g~~Cloud geometric thickness dz is set to 1000 m. That represents a contrail after approximately 30 min lifetime (Freudenthaler et al., 1995) and an average cirrus or aged contrail as confirmed by climatologies from lidar (Noël and Haeffelin, 2007; Iwabuchi et al., 2012) and satellite observations, for example, by Sassen and Campbell (2001). During the cloud life time the ice crystals might grow due to supersaturation and WV deposition, and start to sediment. Sedimentation lowers the cloud base altitude and increases dz. To investigate the effect of variations in dz on solar, TIR, and net RE, a separate sensitivity study for a sub-set of the full parameter space is performed with dz of 500 and 1500 m, while keeping the total ice water path (IWP) constant and, thus, the solar cloud optical thickness τ_ice constant. The total IWP and the scaled IWC are provided in Table 2. τ_ice can be approximated by:

$$\tau_\mathrm{ice} = \frac{3 \cdot Q_\mathrm{e} \cdot IWC \cdot \mathrm{d}z}{4 \cdot \rho_\mathrm{ice} \cdot r_\mathrm{eff}} = \frac{3 \cdot Q_\mathrm{e} \cdot IWP}{4 \cdot \rho_\mathrm{ice} \cdot r_\mathrm{eff}} \tag{10}$$

Table 2. Ice water path IWP (in $\mathrm{g\,m^{-2}}$) and ice water content IWC (in $\mathrm{g\,m^{-3}}$) for the reference case with $\mathrm{d}z = 1000$ m and the two additional clouds with $\mathrm{d}z$ of 500 and 1500 m.

	IWP [$\mathrm{g\,m^{-2}}$]						
	0.7	1.5	3	6	12	24	100
IWC (dz = 500 m) [$\mathrm{g\,m^{-3}}$]	0.0014	0.003	0.006	0.012	0.024	0.048	0.2
IWC (dz = 1000 m) [$\mathrm{g\,m^{-3}}$]	0.0007	0.0015	0.003	0.006	0.012	0.024	0.1
IWC (dz = 1500 m) [$\mathrm{g\,m^{-3}}$]	0.00045	0.001	0.002	0.004	0.008	0.016	0.0667

with density of ice $\rho_{\mathrm{ice}} = 917\,\mathrm{kg\,m^{-3}}$ ~~as found during the Mid–Latitude Cirrus campaign (Luebke et al., 2016; Krämer et al., 2016, 2~~ ~~. For our simulations, we span a similar range of IWC from $15 \cdot 10^{-4}$ to $0.1\,\mathrm{g\,m^{-3}}$.~~

and Q_{e} the average extinction efficiency factor of ice crystals (Horváth and Davies, 2007; Wang et al., 2019). It has to be noted that Eq. 10 does not hold for the TIR wavelength range.

– The parameter sensitivity study is complemented by investigating the influence of a second cloud layer~~, with a cloud base at 3 km. In case of the subarctic winter profile the temperature at 3 km~~. The second cloud layer is implemented as a stratiform, low-level liquid water cloud with a constant cloud top altitude $z_{\mathrm{liq,CT}}$ at 1500 m and a geometric thickness of 500 m. The altitude of 1500 k was selected as a compromise between typical conditions of low-level stratiform clouds in the Subarctic, the mid-latitudes, and tropical regions. McFarquhar et al. (2007) and van Diedenhoven et al. (2009) found $z_{\mathrm{liq,CT}} = 1000$ m for Arctic clouds. Slightly higher $z_{\mathrm{liq,CT}}$ between 1000 and 1500 m are found in the mid-latitudes (Rémillard et al., 2012; Muhlbauer et al., 2014). Low-level clouds in the tropics also range between 500 and 1700 m even though some cloud tops can reach up to 2000 m (Medeiros et al., 2010; Stevens et al., 2016). Fixing $z_{\mathrm{liq,CT}}$ at 1500 m leads to liquid cloud top temperature T_{liq} of 278.5 and 290.7 K for the mid-latitude and tropical profile, respectively. In the Subarctic profile however, T_{liq} reaches 257.5 K (−15.65 K), which is below freezing ~~but it is assumed that the cloud still consists of~~ and implies a super-cooled liquid water cloud. This agrees with observations from Hogan et al. (2004) and Hu et al. (2010), who found that the majority of clouds in the Arctic (≈ 70 %) are characterized by super-cooled droplets at cloud top. Furthermore, 95 % of the observed clouds that have a T_{liq} between −15 and 0°C have super-cooled droplets ~~. The optical depth τ_{wc}~~ at the top. The cloud optical thickness τ_{liq} at 550 nm wavelength of the liquid water cloud is varied between 0 and ~~20 at 550 nm wavelength.~~ 20. Within the RT simulations the optical properties of liquid water clouds are represented by pre-calculated Mie tables ~~(Mie, 1908; van de Hulst, 1981)~~(Mie, 1908; van de Hulst, 1981).

An overview of the model configuration is given in Table 3 and the input parameter space is listed in Table 4. An example libRadtran ~~input-file~~ input file is provided as supplementary ~~document~~material.

For each of the three simulated ice crystal shapes a NetCDF file is provided ~~(Wolf et al., 2023a)~~(Wolf et al., 2023b). The files include ice cloud optical thickness τ_{ice}, the simulated upward and downward irradiances F at TOA with 120 km (with and without the presence of the ice cloud), and the calculated ice cloud radiative effect ΔF (solar, TIR, net). The available cloudy

Table 3. Basic model configuration and selected settings.

Model configuration	Selected value / setting
Radiative transfer solver	fdisort2 (Stamnes et al., 2000)DISORT (Buras et al., 2011)
Number of streams	16
Extraterrestrial solar spectrum	Kurucz (1992)
Wavelength range	0.3–3.5 μm (solar) & 3.5–75 μm (thermal-infrared)
Molecular absorption	Fu and Liou (1992, 1993)
Ice properties	Yang et al. (2000)Ice habit aggregates, plates, droxtals Yang et al. (2013)
Output altitude	15120 km = TOA , 1 km resolution

Table 4. Simulated parameter space(range), actual values selected (steps) and number of values selected.

Model parameter	Symbol	Range Steps Simulated values	Total number of comb
Solar zenith angle (°)	θ	0–70 0, 10, 30, 50, 70, 85	56
Ice water content (g m^{-3})	IWC	15 · 10^{-4} – 0.1 0.0007, 0.0015, 0.003, 0.006, 0.012, 70.024, 0.05, 0.1	7
crystal Crystal effective radius (μm)	r_{eff}	5–45 5, 10, 15, 30, 45 25, 60, 85	46
Cirrus temperature (K)	$T_{\text{cld,ice}}$	223–243 223, 233219, 225, 231, 237, 243	35
Surface albedo	α_{srf}	0–1 0, 0.15, 0.3, 0.6, 1.0	5
Surface temperature (K)	T_{srf}	233–313 233, 273, 313 257, 288, 300	3
Atmosphere profiles	-	US Standard atmosphere , tropicalafglus, tropical afglt, subarctic winter (Anderson et al., 1986) afglsw	-3
Second cloud layer optical depth	τ_{wc} 0–20 τ_{liq}	0, 1, 5, 10, 20	5
Ice crystal shapes	-	aggregates (column_8elements), droxtals, plates	3
			Total number of comb

and cloud-free irradiances further allow to calculate the cirrus RE by scaling the 'cloudy' RE with the required cloud cover. An overview of all variables provided in the NetCDF files are given in Table 5. The data set allows the user to extract ΔF values for their parameter combinations. The available cloudy and cloud-free irradiances further allow to calculate the cirrus RE by scaling the 'cloudy' RE with , instead of running costly RT simulations. Potential applications are the investigation of the provided input parameters on ΔF and the required cloud cover. This serves as a first-approximation because, as 3D effects are neglected. coupling of the data set with contrail prediction models, for example, the Contrail Cirrus Prediction Tool (CoCiP) (Schumann, 2012).

The simulations base on three relative humidity profiles, which were selected to represent subarctic, mid-latitude, and tropical conditions. A estimation in RE variability due to variations in the RH profile showed an effect of less than 1 % for ΔF_{sol} but

Table 5. List of variables that are provided in the NetCDF. The output is provided at TOA top of atmosphere located at 15120 km altitude.

Long name	Variable name Symbol	Variable name in NetCDF file	Unit
Dimensions			
Solar zenith angle	θ	*solar_zenith_angle*	°
Ice cloud temperature	T_{ice}	*ice_cloud_temp*	K
Surface albedo	α_{srf}	*surface_albedo*	-
Ice water content	IWC	*ice_water_content*	$g\,m^{-3}$
Surface temperature	T_{srf}	*surface_temperature*	K
Ice crystal effective radius	r_{eff}	*crystal_effective_radius*	µm
Liquid water cloud optical thickness	τ_{liq}	*optical_thickness_liquid_water_cloud*	-
Cloudy or cloud-free	-	*cloudy_cloudfree*	-
Variables			
Downward solar total (direct + diffuse) irradiance	$F^{\downarrow}_{sol}$	*Fdn_sol*	$W\,m^{-2}$
Upward solar irradiance	$F^{\uparrow}_{sol}$	*Fup_sol*	$W\,m^{-2}$
Downward thermal-infrared irradiance	$F^{\downarrow}_{tir}$	*Fdn_tir*	$W\,m^{-2}$
Upward thermal-infrared irradiance	$F^{\uparrow}_{tir}$	*Fup_tir*	$W\,m^{-2}$
Solar cloud radiative effect	ΔF_{sol}	*RF_sol*	$W\,m^{-2}$
Thermal-infrared cloud radiative effect	ΔF_{tir}	*RF_tir*	$W\,m^{-2}$
Net radiative effect	ΔF_{net}	*RF_net*	$W\,m^{-2}$
Ice cloud optical thickness	τ τ_{ice}		-

can range up to 4 % for ΔF_{tir} and 8 % for ΔF_{net} especially for the warm and moist tropical profile. These variations have to be considered, when using the data set.

2.3 Relationship between effective radius, ice water content, crystal number concentration, and cloud optical thickness

Assuming spherical crystals the IWC of an ice cloud is calculated as: The liquid water content of a liquid water cloud can be obtained by:

$$\mathrm{IWC}\,\mathrm{LWC} = \frac{4}{3}\cdot\pi\cdot\rho_{\mathrm{ice}\,\mathrm{liq}}\cdot\int_0^\infty n(r)\cdot r_{\mathrm{vol}}{}^3\cdot \mathrm{d}r \tag{11}$$

with $\rho_{ice} = 917\,\mathrm{kg\,m^{-3}}$ $\rho_{liq} = 1000\,\mathrm{kg\,m^{-3}}$ the density of ice, liquid water, r the radius, and $n(r)$ the PSD, and r_{vol} the volumetric radius. Rearranging Eq. 11 leads to the ice crystal number concentration of:

$$N_{ice} = \frac{3\cdot IWC}{4\cdot\pi\cdot\rho_{ice}\cdot r_{vol}^3\cdot\beta}.$$

By adding a correction factor β the non-spherical shape of ice crystalsis taken into account. Yang et al. (2003) determined that the volume ratio of a crystal with respect to a circumscribing sphere reaches a maximum value of 0.7 number of droplets with size r. Equation 11 assumes spherical ice crystals, so might be valid for droxtals, which we use in the following. One has to keep in mind that the resulting N_{ice} represents a lower boundary as β is smaller than 0.7 for all are almost spherical ice crystals, but it is invalid for other ice crystal shapes. Equation 14 can also be used for liquid water clouds setting $\beta = 1$ and using the liquid water density $\rho_{\mathrm{liq}} = 1000\,\mathrm{kg\,m^{-3}}$.

2.4 Blackbody emission

The RT in the TIR is primarily driven by the surface temperature T_{srf} and the (ice) cloud temperature $T_{\mathrm{cld,ice}}$ with the latter one being directly linked to the vertical location of the cloud in the atmosphere and the atmospheric temperature profile. In a first order approximation, the emitted irradiance of a blackbody can be calculated bythe Stefan–Boltzmann-law: To obtain the particle number concentration N_{ice} for non-spherical crystals, appropriate power-law mass-dimension relations are needed. Here we employ Eq. 29 from Mitchell et al. (2006) but modify the notation to be consistent with the previous equations from the present study. Equation 29 from Mitchell et al. (2006) is then given by:

$$F\,\mathrm{IWC} = \sigma\cdot\epsilon\cdot T^4 \frac{\alpha\cdot\Gamma(\beta+\mu+1)\cdot N_{\mathrm{ice}}}{\Gamma(\mu+1)\cdot\Lambda^{\beta}}, \qquad (12)$$

which is obtained by integrating the Planck function over all wavelengths and $2\cdot\pi$ of a hemispheric solid angle. In Eq. **??** the Stefan–Boltzmann-constant is represented by σ in units of $\mathrm{W\,m^{-2}\,K^{-4}}$ and with Γ the result of the emissivity ϵ of a body. While sufficiently geometrical thick liquid and ice water clouds might be treated as black bodies with $\epsilon \approx 0.95$, geometrically thin clouds with low liquid or ice water path act as gray bodies. The cirrus emissivity of such thin clouds might be approximated by: numerically solved gamma function. The constants α and β are the prefactor and the power in the mass–dimensional relationship, respectively. They are related by:

$$\epsilon m = 1-\exp\left(-\zeta\cdot CWP\right)\alpha\cdot D^{\beta}, \qquad (13)$$

with factor $\zeta = 0.144\,\mathrm{m^2\,g^{-1}}$ from Stephens (1978) and the cloud water path CWP in units of $\mathrm{g\,m^{-2}}$ (Lohmann and Roeckner, 1995). Nevertheless, the maximum of emitted radiation might be estimated on basis of a black body, knowing that the truly emitted radiation is smaller. Equation **??** therefore states the total irradiance emitted by an object is proportional to T^4 m the mass of the ice crystal and D the maximum dimension of the ice crystal. Both constants depend on the ice crystal shape and are, for example, listed in Mitchell (1996). Using Eq. **??**, ΔF_{tir} can be approximated by:

$$\Delta F_{\mathrm{tir}} \approx F_{\mathrm{srf}} - F_{\mathrm{cld}} = \sigma\cdot\epsilon\cdot\Delta T^4 = \sigma\cdot\epsilon\cdot\left(T_{\mathrm{srf}}^4 - T_{\mathrm{cld,ice}}^4\right).$$

13 and assuming an exponential PSD with the special case $\mu = 0$ and $\Lambda = \frac{3}{r_{\mathrm{e}}}$ (Deirmendjian, 1962; Petty and Huang, 2011), finally leads to:

$$N_{\mathrm{ice}} = \frac{3^{\beta}\cdot\mathrm{IWC}}{\alpha\cdot\Gamma(\beta+1)\cdot r_{\mathrm{e}}^{\beta}}. \qquad (14)$$

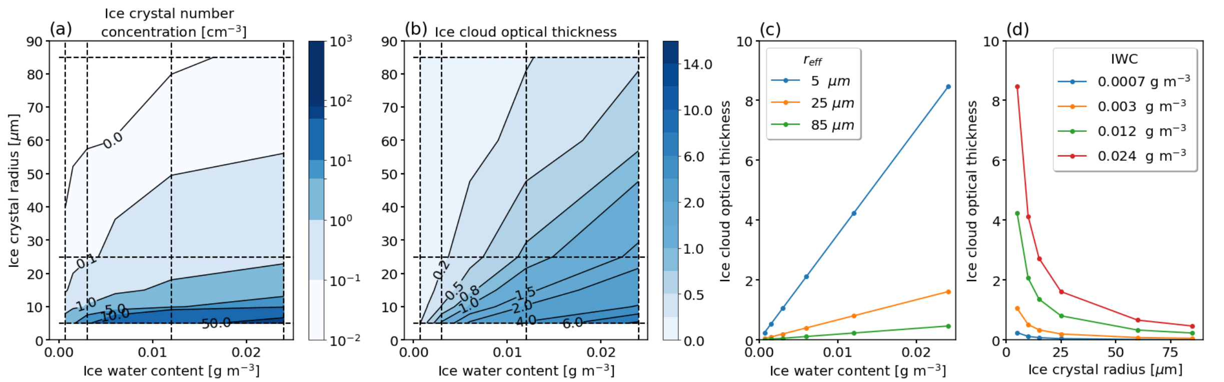

Figure 1. (a–b) ~~Ice~~ Calculated ice crystal number concentration N_{ice} (in cm^{-3}) and simulated cloud optical thickness ~~τ~~ τ_{ice} at ~~640~~550 nm wavelength as a function of ice water content IWC (in g m^{-3}) and effective crystal radius r_{eff} (in μm). A cloud geometric thickness dz of 1000 m is selected. **(c–d)** Cross-sections along lines of constant r_{eff} or IWC that are indicated as dashed lines in panel a ~~or~~ and b, respectively.

~~Consequently, ΔF_{tir} of an ice cloud results from the temperature difference between surface (T_{srf}) and cirrus ($T_{\mathrm{cld,ice}}$). When a second cloud layer is involved and the liquid water cloud cloud is optically opaque in the TIR then T_{srf} is replaced by the temperature $T_{\mathrm{cld,wc}}$ of the underlying cloud layer~~Therefore N_{ice} is proportional to $\frac{\mathrm{IWC}}{r_e^\beta}$, with β around 2 for aggregates, 2.4 for hexagonal-plates, and 3 for almost spherical droxtals (Mitchell, 1996).

3 Results

~~Separating the intertwined dependencies of ΔF on the input parameters is key to understanding the cirrus and contrail RE. To provide a first overview~~ We first provide an overview of how r_{eff} and IWC determine the cloud optical and microphysical properties~~, Fig.~~. Figure 1a–d illustrates the dependence ~~between~~ of N_{ice} and τ_{ice} as a function of r_{eff} and IWC. ~~While~~ N_{ice} is approximated by Eq. 14, assuming droxtals (almost spherical ice crystals), a mono-disperse particle size distribution, and a cloud geometric thickness dz of 1000 m. The ice cloud optical thickness τ_{ice} ~~is directly diagnosed by libRadtran .~~ at 550 nm wavelength, given in Fig. 1b–d, is directly calculated by libRadtran using optical properties from droxtals.

~~Figure 1a visualizes the linear dependency of N_{ice} on IWC and a dependency on the power of -3 on r_{eff}.~~ The largest N_{ice} values result from the smallest ice crystals sizes (~~$r_{\mathrm{eff}} < 20$~~$r_{\mathrm{eff}} \le 10$ μm), particularly in combination with large IWC ~~. For those combinations (small r_{eff}~~ (Fig. 1a). For combinations of small $r_{\mathrm{eff}} < 15$ μm and large IWC~~)~~, N_{ice} is most sensitive to r_{eff}, which is indicated by the narrowing contour lines that align along the x-axis. For a constant r_{eff} ~~value~~ of 5 μm, the estimated N_{ice} ranges from 1 to over ~~100~~80 cm^{-3}. Such concentrations of ~~$N_{\mathrm{ice}} > 100$~~$N_{\mathrm{ice}} > 80$ cm^{-3} are rarely observed in natural cirrus though they can occur in very young contrails and contrail-induced cirrus (Krämer et al., 2016). Generally smaller N_{ice} and a reduced sensitivity to r_{eff} and IWC is found for $r_{\mathrm{eff}} > 20$ μm, where N_{ice} ~~ranges below 1~~mostly ranges below 10 cm^{-3}.

The ~~observed~~ inherent dependencies of N_{ice} presented in Fig. 1a are also found in the distribution of the ice cloud optical thickness τ_{ice} at ~~640 nm given~~ 550 nm shown in Fig. 1b. Following lines of constant r_{eff} (Fig. 1c), the increase in IWC corresponds to a linear increase in N_{ice} and, therefore, to a gain in the total scattering and absorption particle cross-sections. The absorption of radiation by liquid water and ice (as characterized by the complex refractive index) at ~~640~~550 nm wavelength is weak and~~therefore scattering is dominating~~ , therefore, scattering dominates τ_{ice}. Alternatively, going along lines of constant IWC towards larger r_{eff} leads to a decrease in N_{ice} and a related decrease of the total scattering particle cross-section (cloud albedo effect, Fig. 1d). This effect is most effective for larger IWC (optically thick clouds) and is less pronounced for clouds with smaller IWC.

~~Going beyond these~~ To go beyond these basic dependencies, the impact of each parameter is estimated by ~~varying each of them in turn~~fixing one parameter at a time, while the ~~remaining parameters are kept at a fixed reference value. Modifying each parameter separately~~ others can vary. For example, in case of r_{eff}, all simulations, for steps of r_{eff} given in Table 4, are extracted from the 8-D hypercube. The extracted sub-sample, in the example for a specific r_{eff}, is used to calculate the distributions of solar, TIR, and net ΔF. These distributions are then visualized by box plots and characterized by their minimum, maximum, median, as well as the 25^{th}- and 75^{th}-percentiles. This strategy can be interpreted as a type of ~~a sampling~~sub-sampling, by averaging all unfixed ~~values, to 'project '~~ parameters to project ΔF onto the one-dimensional space. The impact of each parameter is further quantified by the minimum and maximum RF. We define the full range of ΔF by:

$$R_{\Delta \mathrm{F}} = max\{\Delta F\} - min\{\Delta F\}, \tag{15}$$

with $max\{\Delta F\}$ and $min\{\Delta F\}$ the maximum and minimum of ΔF across the ~~94~~283,500 combinations of input parameters, respectively. As $R_{\Delta \mathrm{F}}$ is susceptible to outliers, we further characterize the width of a distribution by the inter-quartile range, which is defined as the difference between the 75^{th} ($Q_{75\%}$) and 25^{th} ($Q_{25\%}$) ~~percentile~~ percentiles of ΔF:

$$Q_{\Delta \mathrm{F}} = Q_{75\%}(\Delta F) - Q_{25\%}(\Delta F) \tag{16}$$

A reference cloud is created by selecting minimum or maximum values from the parameter space given by ~~$\theta = 0°$, $T_{\mathrm{cld,ice}} = 223$ K, $\alpha_{\mathrm{srf}} = 0$, $T_{\mathrm{srf}} = 313$ K, $r_{\mathrm{eff}} = 45$ µm, and $\tau_{\mathrm{wc}} = 0$~~ $\theta = 0°$, $T_{\mathrm{cld,ice}} = 219$ K, $\alpha_{\mathrm{srf}} = 0$, $T_{\mathrm{srf}} = 300$ K, $r_{\mathrm{eff}} = 85$ µm, and $\tau_{\mathrm{liq}} = 0$ (no liquid water cloud). ~~An exception is the selected IWC , which is set to a medium value of 0.024 g m^{-3}. This is done to ensure that~~ For IWC we do not use minimum or maximum but the value of 0.024 g m^{-3} because together with a dz of 1000 m and an r_{eff} of 85 µm this leads to a τ_{ice} of ~~the reference case, considering our fixed $\Delta z = 0.2$ km and reference $r_{\mathrm{eff}} = 45$ µm, is 0.18 at 640~~0.46 at 550 nm wavelength, which is representative for contrails and young cirrus ~~.~~ (Iwabuchi et al., 2012). The reference cloud is assumed to consist of rough-aggregates.

Figure 2a–c shows solar, TIR, and net ΔF, respectively, following Meerkötter et al. (1999). First, the influence of variations in θ is investigated in order to sample the diurnal cycle and its variation as a function of latitude. For ~~the~~ all Sun geometries, ΔF_{sol} is negative and, therefore, the cirrus has a cooling effect in the solar spectrum on the atmosphere-surface system. ΔF_{sol} intensifies (i.e., becomes more negative) with increasing θ as the length of the ~~photon path , $s = \Delta z / \cos\theta$,~~ optical path through the cloud, $s = \Delta z / \cos\theta$, increases, which is accompanied by enhanced scattering (and thus upward directed scattering) of the incoming radiation. In addition, a lower fraction of the incident radiation is scattered towards the surface but scattered upward ~~back into~~ to space. This is due to the strong forward peak in the ice crystal phase function $\mathcal{P}$ that decreases sharply

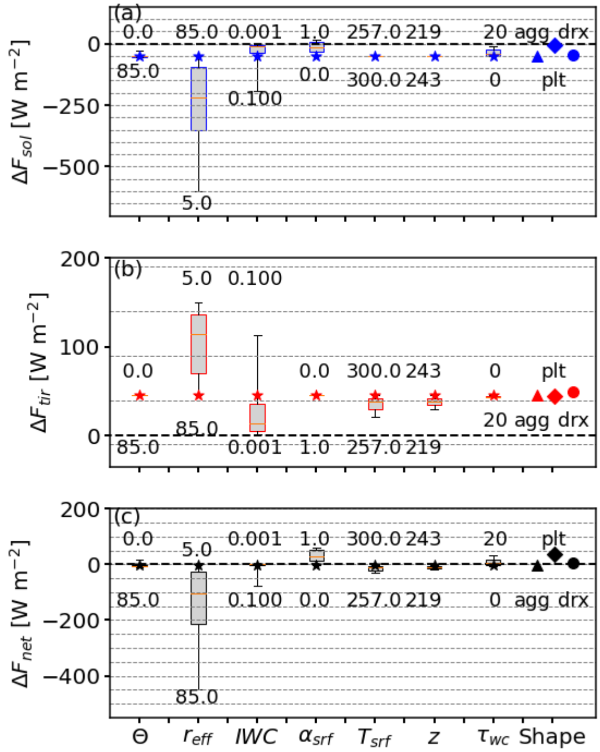

Figure 2. (a–c) Box and whisker plot of solar, TIR, and net ΔF (in $\mathrm{W\,m^{-2}}$) due to the variation of the parameters indicated as the x-axis$x$-axis. The boxes represent the 25 % $^{\mathrm{th}}$ – and 75 % $^{\mathrm{th}}$-percentilesand , while the whiskers indicate the minimum and maximum values. Median values are given in each box by horizontal, orange lines. The stars indicate the reference case with solar zenith angle $\theta = 0°$, effective radius r_{eff} = 585 μm, ice water content IWC = 0.024 $\mathrm{g\,m^{-3}}$, surface albedo $\alpha_{\mathrm{srf}} = 0$, T_{srf} = 313 Ksurface temperature T_{srf} = 300 K, z = 13 kmice cloud temperature $T_{\mathrm{cld,ice}}$ = 219 K, and τ_{wc} = 0. liquid water cloud optical thickness τ_{liq} = 0. Minimum and maximum of the parameter ranges are given by the numbers. Plot idea adapted from Meerkötter et al. (1999).

for $\Theta > 10°$ (see in Appendix Fig. D1). An exception appears for θ of 85°, where ΔF_{sol} is smallest. Variations in θ lead to ΔF_{sol} between $-$32.7 55.9 and $-$14.627.5 $\mathrm{W\,m^{-2}}$. As expected, ΔF_{tir} is unaffected by the Sun position with a constant ΔF_{tir} = 17.946.0 $\mathrm{W\,m^{-2}}$. The resulting sensitivity of ΔF_{net} is driven by ΔF_{sol} with ΔF_{net} between $-$14.8 and 3.39.9 and 18.5 $\mathrm{W\,m^{-2}}$. During nighttime there is no contribution from ΔF_{sol} leading to a constant, positive ΔF_{net} = 17.946.0 $\mathrm{W\,m^{-2}}$ (leading to a warming).

As expected, variations in r_{eff} have the largest effect on the solar, TIR, and net ΔF, as N_{ice} relates to r_{eff} by the power of -3 (see $-\beta$, which depends on the ice crystal shape (see Sec. 2.3 and Eq. 14). Increasing Reducing r_{eff} from 5 to 4585 to 5 μm leads to ΔF_{sol} between $-$162.5 599.5 and $-$14.650.2 $\mathrm{W\,m^{-2}}$. The distribution of ΔF_{tir} has a minimum and maximum of 17.9 and 74.246.0 and 149.8 $\mathrm{W\,m^{-2}}$, respectively. ΔF_{sol} dominates ΔF_{tir} and results in values of ΔF_{net} ranging from $-$88.3 to 3.3449.8 to -4.2 $\mathrm{W\,m^{-2}}$.

Variations in IWC affect solar, TIR, and net ΔF. Generally, an increase in IWC (increase in τ_{ice} for fixed r_{eff}), enhances total scattering and absorption particle ~~cross-section~~ cross-sections and, therefore, intensifies the cooling in the solar (more negative ΔF, cloud albedo effect) and the TIR heating (more positive ΔF). ΔF_{sol} ranges from $-$~~65.1~~ 191.1 to $-$~~0.9~~1.5 W m^{-2}, with $\Delta F_{\mathrm{sol}} = -$~~14.6~~50.2 W m^{-2} obtained for the reference IWC. The distribution of ΔF_{tir} spans values between ~~1.2 and 57.8~~1.8 and 112.7 W m^{-2}, leading to ΔF_{net} from $-$~~7.3 to 3.3~~78.4 to 1.1 W m^{-2}. The ~~given~~ ΔF ~~ranges, by varying IWC ,~~ given above correspond to a varying IWC and assume r_{eff} = ~~45~~85 μm. ~~Smaller~~ For smaller r_{eff} ~~increase~~ ΔF increases and thus increases the range of solar, TIR and net ΔF.

Variations in α_{srf} impact only the solar spectrum, as expected, with ΔF_{sol} between $-$~~14.6 and 5.9~~50.2 and 15.4 W m^{-2}. The most negative RE appears over non-reflective surfaces and decreases with increasing α_{srf}, due to the decrease in contrast between the surface and the cirrus. In cases where α_{srf} exceeds the ~~reflectivity of the cloud~~ cloud albedo, ΔF_{sol} becomes positive. For the optical thin reference cloud this is the case over a fully sea ice covered area with $\alpha_{\mathrm{srf}} \approx 1$. The TIR component remains ~~unaffected with $\Delta F_{\mathrm{tir}} = 17.9$ W m^{-2}~~almost unaffected with ΔF_{tir} between 39.5 and 46 W m^{-2}. Together with the decreasing cooling effect in the solar, the warming in the TIR mostly dominates and leads to ~~a net warming cirrus with~~ ΔF_{net} ranging between ~~3.3 and 23.8~~-4.2 and 55.0 W m^{-2}.

The influence of a varying surface temperature T_{srf} or cirrus temperature $T_{\mathrm{cld,ice}}$ (related to cloud base altitude), are investigated for a cloud scenario with a solar surface albedo α_{srf} set to 0. Varying surface temperature T_{srf} or cirrus temperature $T_{\mathrm{cld,ice}}$ (related to cloud base altitude), ΔF_{sol} remains almost constant with a minimum and maximum ΔF_{sol} for both parameters of $-$~~14.6~~ 50.2 and $-$~~14.4~~49.2 W m^{-2}, respectively. These small differences are due to changes in molecular absorption, which ~~result~~ results from the variations in the relative humidity profile as the profile depends on the selected T_{srf}. A noticeable effect is found for ΔF_{tir}, which is impacted by variations in $T_{\mathrm{cld,ice}}$ and T_{srf}. While decreasing $T_{\mathrm{cld,ice}}$ from 243 to ~~223~~219 K lowers ΔF_{tir} from ~~20.6 to 15~~46 to 29.9 W m^{-2}, a decrease in T_{srf} from ~~313 to 233~~300 to 257 K reduces ΔF_{tir} from ~~15 to 0.2~~46 to 20.8 W m^{-2}. Consequently, ΔF_{tir} determines the response of the resulting ΔF_{net}, which spans from ~~6 to 0.2~~ -4.2 to -19.4 W m^{-2} for $T_{\mathrm{cld,ice}}$ and $-$~~14.2 to 0.5~~28.7 to -4.2 W m^{-2} for T_{srf}. The greater influence of T_{srf} on ΔF_{tir} and ΔF_{net} can be explained simply by the greater variation of the input.

A second cloud layer is considered by inserting a liquid water cloud with a cloud ~~base altitude $z_{\mathrm{base}} = 3$ km~~ top altitude $z_{\mathrm{base}} = 1500$ m and a geometric thickness ~~$\Delta z = 200$ m~~d$z = 500$ m. Figure 2 shows that this second cloud influences both components ΔF_{sol} and ΔF_{tir}. Generally speaking, the liquid water cloud enhances the fraction of solar, upward directed radiation compared to a dark surface. With increasing ~~τ_{wc}~~ τ_{liq} (increase in LWC) $\alpha_{\mathrm{cld,ice}}$ exceeds α_{srf}, which lowers the albedo contrast between the ice cloud and the surface for most of the parameter combinations. This minimizes solar RE and leads to a minimum of $-$~~16.2~~51.1 W m^{-2} and a maximum of $-$~~3.6~~11.6 W m^{-2}. For the TIR part the increase in LWC masks the influence of the underlying surface by absorbing the upward TIR radiation from the surface and re-emitting radiation at the liquid water cloud temperature. This leads to ΔF_{tir} between ~~10.5 and 15~~43.2 and 46.0 W m^{-2}. The resulting ΔF_{net} is ~~almost equally impacted by the two wavelength ranges and the distribution is~~ characterized by a minimum and maximum of $-$~~3.7 and 6.9~~6.5 and 31.6 W m^{-2} primarily impacted by the solar component.

The parameter study is complemented by investigating the effect of prescribing three different ice crystal shapes. The variation in ΔF_{sol} due to the transition from almost spherical (droxtals) to non-spherical crystals (aggregates) leads to a relative change in ΔF_{sol} that is, in terms of RE, comparable to a variation in θ. The strongest cooling effect (negative ΔF_{sol}) is found for ~~droxtals~~ aggregates with $-$~~16.9~~50.2 W m^{-2} and decreases for ~~aggregates~~ droxtals and plates to $-$~~15~~ 44.3 and $-$~~6.8~~8.6 W m^{-2}, respectively. Ice crystal shape also impacts ΔF_{tir}. Aggregates lead to ΔF_{tir} of ~~17.9~~46 W m^{-2}, while plates and droxtals can cause a ΔF_{tir} of ~~20.2 and 22.7~~44.5 and 48.9 W m^{-2}, respectively. Consequently, the largest ΔF_{net} with ~~13.4~~35.8 W m^{-2} is found for plates and followed, in decreasing order, by droxtals and aggregates with ~~5.8 and 3.3~~4.5 and -4.2 W m^{-2}, respectively. As mentioned in the introduction, the uncertainty in the ice crystal shape causes uncertainties in the calculated ΔF. Nevertheless, using three different ice crystal shapes for the irradiance simulations shows that the shape-specific scattering properties are of lesser importance compared to other parameters like the ice crystal size (distribution), the IWC, or surface properties.

~~It must be~~ The presented analysis of solar, TIR, and net ΔF sensitivity on the selected input parameters generally agrees with the results from Meerkötter et al. (1999). We found differences in the importance of the parameters, which are explained by the fact that our simulations span a larger and different parameter range, for example in r_{eff} and T_{srf}. In addition, the sensitivity analysis in Fig. 2 is sensitive to the selection of the reference cloud.

It is further emphasized that the presented ΔF_{net} is representative for daytime situations only, ~~where θ is between 0° and 70°~~ when the Sun is above the horizon. In the absence of solar illumination during nighttime, the net effect is entirely determined by and equal to ΔF_{tir}, which is positive (warming effect) in all simulation cases. Accordingly, all simulated cloud cases do have a net warming effect at night. For a more in-depth analysis, the subsequent plots focus on the impact of each individual parameter.

3.1 Sensitivity on ice crystal shape

One difficulty of RT simulations in ice clouds is the uncertainty about the dominating ice crystal shape, which is commonly unknown and, therefore, a general ice crystal shape has to be assumed (Kahnert et al., 2008). Scattering and absorption by an ice crystal is characterized by its ~~shape, orientation, size,~~ orientation, complex refractive index of ice, ~~and~~ the wavelength of the incident light~~. To some extent, the dependence on the shapecan be partly condensed into the knowledge of the crystal aspect ratio, which is defined as the ratio of the width to the length of a non-spherical crystal (Macke et al., 1998). For non-spherical crystals the effective crystal diameter or radius (Eq. 6) is smaller than the geometrical crystal diameter or radius. Considering small crystals with $r_{\mathrm{eff}} \approx 50\,\mu$m, the aspect ratio is largest for spheres and followed, in descending order, by droxtals, solid columns, spheroids, hallow columns, plates, and aggregates (Yang et al., 2005). In this order, the crystals become less effective in the interaction with incident radiation for the same maximum dimension~~, shape, size, and the resulting asymmetry parameter. The asymmetry parameter is a measure of the asymmetry of the phase function $\mathcal{P}$ between forward and backward scattering (Macke et al., 1998; Fu, 2007). $\mathcal{P}$ provides the angular distribution of the scattered direction in relation to the incident light. For example, in case of idealized hexagonal ice crystals and wavelength below 1.4 μm, the asymmetry parameter is primarily determined by the ice crystal shape / aspect ratio but for wavelength larger then 1.4 μm the asymmetry parameter also depends on the ice crystal size (Fu, 2007; Yang and Fu, 2009; van Diedenhoven et al., 2012). Consequently, the assumption of an ice crystal habit , related ice crystal phase function (Fig. D1), and the and ice crystal sizedistribution , with related aspect ratio, are vital information to estimate the ice cloud RE. One caveat of Furthermore, the ice optical properties by Yang et al. (2010, 2013) , which are used for the RT simulations in ice clouds is the uncertainty about the dominating ice crystal shape, which is commonly unknown and , therefore, a general ice habit has to be assumed. The assumption of an ice crystal shaperepresents a fundamental uncertainty in the understanding of the present study, based on a coupling of the maximum diameter of the ice clouds (Kahnert et al., 2008)crystal and the aspect ratio, with the later one being different for each crystal shape. This further impacts the RT of different ice clouds.

Subsequently, the shape-effect is quantified using Eq. 15 and relative difference differences in ΔF are given with respect to crystals with the same r_{eff} in relation to the ΔF simulated for aggregates. Figure 3a–c show ΔF_{sol} as a function of IWC, separated for crystal shape, r_{eff}, and three selected θ. For simplicity α_{srf} and τ_{wc} τ_{liq} are set to zero in these simulationsthis discussion.

The strongest ΔF_{sol} is found for plate-like crystals aggregates with $r_{\mathrm{eff}} = 5\,\mu\mathrm{m}$ that are illuminated by with the Sun at zenith ($\theta = 0°$, Fig. 3a). A lower cooling effect in the solar spectrum is found for aggregates and droxtals droxtals and plates with same r_{eff}. The order of ΔF_{sol} changes with increasing r_{eff} and the strongest solar cooling is identified for aggregates and followed by droxtals. The re-ordering in the intensity of ΔF_{sol}, by keeping θ constant , is traced back to the size dependence of the absorption particle cross-section and $\mathcal{P}$ as can be seen in Fig. D1remains constant for increasing r_{eff}.

The spread in ΔF_{sol} across crystals crystal shapes with the same r_{eff} and IWC can be interpreted as the a potential uncertainty in ΔF_{sol} due to the ice habitcrystal shape. One has to keep in mind that the differences partially result from deviating crystal size distributions as these depend on the selected crystal shapethat goes into the calculation of the crystal number $n(r)$ (Eq. 4). Nevertheless, Macke and Großklaus (1998) showed thatthe crystal habit . Macke et al. (1998) showed that, in the solar wavelength range, the crystal shape is the main driver and the actual ice particle size distribution has only a minor effect on ΔF_{sol}. Nevertheless, Mitchell et al. (1996) and Mitchell et al. (2011) found that the particle size distribution also has a considerable impact on ΔF_{tir}, leading to differences of up to 48% in the single-scattering albedo, when switching between PSD.

To quantify the deviations , panels from the ice crystal shape, Fig. 3d–f show absolute and panels Fig. 3g–i present relative differences of ΔF_{sol} of droxtals (greenorange) and plates (blue) with respect to aggregates. In general, For $\theta = 0°$ the largest absolute and smallest relative deviations are found for the optically thickest clouds (highest IWC). Among all θ the largest absolute rangesdeviation is found for plates with r_{eff} of 25 μm and highest IWC with an absolute range, expressed in $R_{\Delta\mathrm{F,sol}}$, are found between aggregates and plates, where $R_{\Delta\mathrm{F,sol}}$ reaches up to −60of up to 250 W m^{-2} (5r_{eff} = 25 μm, $\theta = 0°$, $\tau_{\mathrm{ice}} = 7.1$ $\tau_{\mathrm{ice}} = 6.6$), corresponding to a relative difference of 1558 %. Relative deviations reach even larger values, e.g., when the cloud is optically thin thinner and ΔF_{sol} is smallgets smaller. In case of plates the relative deviations range from 35 −20 % (r_{eff} = 5 μm) to −5882 % (48r_{eff} = 85 μm). With increasing θ The large absolute and relative deviations between plates and aggregates in ΔF_{sol} and later ΔF_{net} appear because plates are characterized by the smallest reflectance and absorption efficiency (Key et al., 2002; Yang et al., 2005). The absolute differences among droxtals and aggregates are

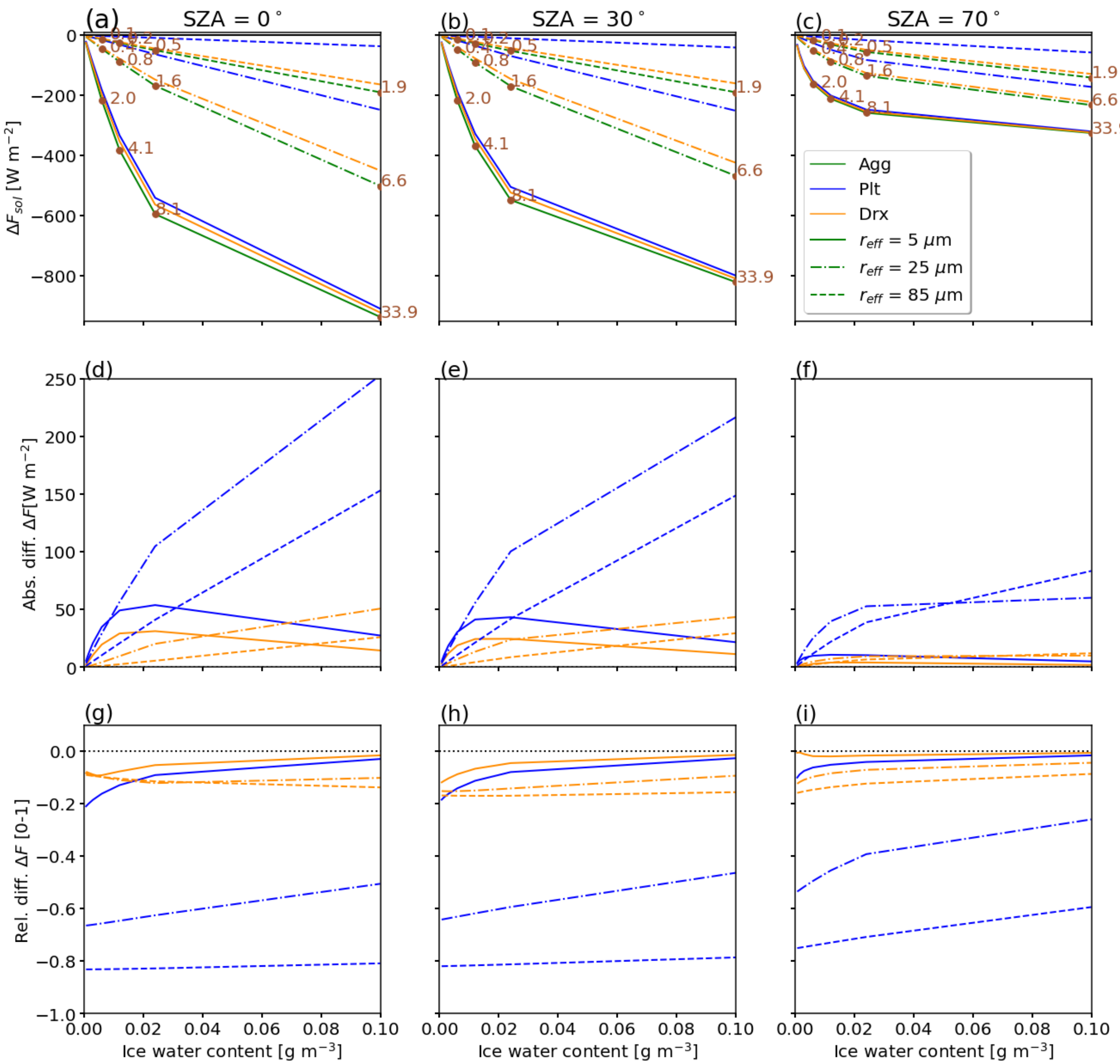

Figure 3. (a–c) Solar radiative effect ΔF_{sol} (in $\mathrm{W\,m^{-2}}$) as a function of ice water content IWC for three values of solar zenith angle θ of 0°, 30°, and 70°. Three ice crystal radii r_{eff} of 5 (solid), ~~30~~ 25 (dash-dot), and ~~48~~85 μm (dashed) are indicated. The ice crystal shape is color-coded with aggregates 'Agg', plates 'Plt', and droxtals 'drx' given in green, blue, and orange, respectively. **(d–f)** show absolute difference and **(g–i)** relative difference between ΔF_{sol} of droxtals and plates with respect to aggregates with the same crystal radius. The numbers indicate the optical thickness simulated for the reference cloud that contains ice aggregates.

smaller. With increasing IWC the absolute ranges in ΔF_{sol} become smaller . quickly reach a maximum of 50 W m^{-2} at IWC of 0.024 g m^{-3} and decrease towards the largest IWC. The associated relative deviations are also smaller compared to plates, ranging between -3 % (r_{eff} = 5 μm) and -18 % (r_{eff} = 85 μm).

Another characteristic of $R_{\Delta\mathrm{F,sol}}$ is the steep slope for $\theta = 0°$ over the entire range of IWC. For illumination geometries with the Sun closer to the horizon, particularly $\theta = 70°$, the behavior of absolute range in ΔF_{sol} is characterized by a rapid increase and convergence towards a maximum. At a certain IWC and related τ_{ice}, the slant light optical path and cloud-radiation interactions are dominated by multiple scattering that suppresses single-scattering effects of individual ice habitscrystal shape, hence, reducing the absolute and relative difference resulting from the choice of the ice habitcrystal shape.

Next, we consider the solar, TIR, and net ΔF at $\theta = 30°$ (Fig. 4). The left most column for ΔF_{sol} is identical with the center to the middle column in Fig. 3. In the TIR, the largest ΔF_{tir} is generally found for smallest crystals (5 μm) and highest IWC in decreasing order from droxtals, plates, and aggregates. The order remains constant of for all crystal sizes and the absolute values of ΔF_{tir} decrease with increasing crystal size. The largest ΔF_{tir} range of 10130 W m^{-2} is found for clouds with intermediate IWC between 0.02 and 0.06IWC between 0.024 and 0.1 g m^{-3} caused by droxtals. For thin clouds with IWC < 0.04 g m^{-3} the largest relative differences of 38absolute range $R_{\Delta\mathrm{F,tir}}$ of around 6.5 W % appear, e. g. , droxtals with m^{-2} appears for r_{eff} of 5 and 25 μm, which is shifting towards larger IWC with increasing r_{eff} and vanishes for the largest crystals with r_{eff} of 85 μm. The relative differences are largest for the optically thinnest clouds and decrease with increasing IWC. While droxtals are characterized by relative differences close to 0 % (r_{eff} = 5 μum; IWC = 0.1 g m^{-3}) and 18 % (r_{eff} = 15 μm, while deviations of 8 to 10; IWC = 0.007 g m^{-3}), plates lead to relative differences between 9 % are calculated for optically thick clouds containing plate-like crystals.

In case of (r_{eff} = 5 μm; IWC = 0.10.007 g m^{-3}) and -5 % (r_{eff} = 85 μm, IWC 0.007 g m^{-3}). The RE of the optically thickest cloud is independent on ice crystal shape, which is addressed to multiple scattering.

For all IWC and r_{eff}, ΔF_{sol} is larger by a factor of five generally larger than ΔF_{tir} and, therefore, dominates resulting ΔF_{net} (Figure 4c, f). In general, the range of ΔF_{tir} increases and the relative differences decrease towards the maximum of simulated IWC. In this case the value range of ΔF_{tir} is between -40 (10 %) and 40 W m^{-2} (10 %) for plates and droxtals with sizes Consequently, ΔF_{net} and absolute ranges among the ice crystal shapes follow the distributions from ΔF_{sol}. However, the relative deviations are largest for the optically thinnest clouds, where ΔF_{net} is generally small. While for the smallest crystals with r_{eff} of 5 μm , respectively. and optically thick clouds the relative differences approach zero, relative differences exceed the absolute value by a factor of 10.

It has to be added that , as shown in Fig 2, The analysis of all simulations shows that the shape assumption has only second-order implications of on the RE compared to other parameters . Nevertheless, the shape-effect is like IWC or r_{eff} (see Fig 2), which agrees with Meerkötter et al. (1999). However, the impact of shape and associated changes in PSD are of high importance in case of radiance simulations and cloud remote sensing applications.

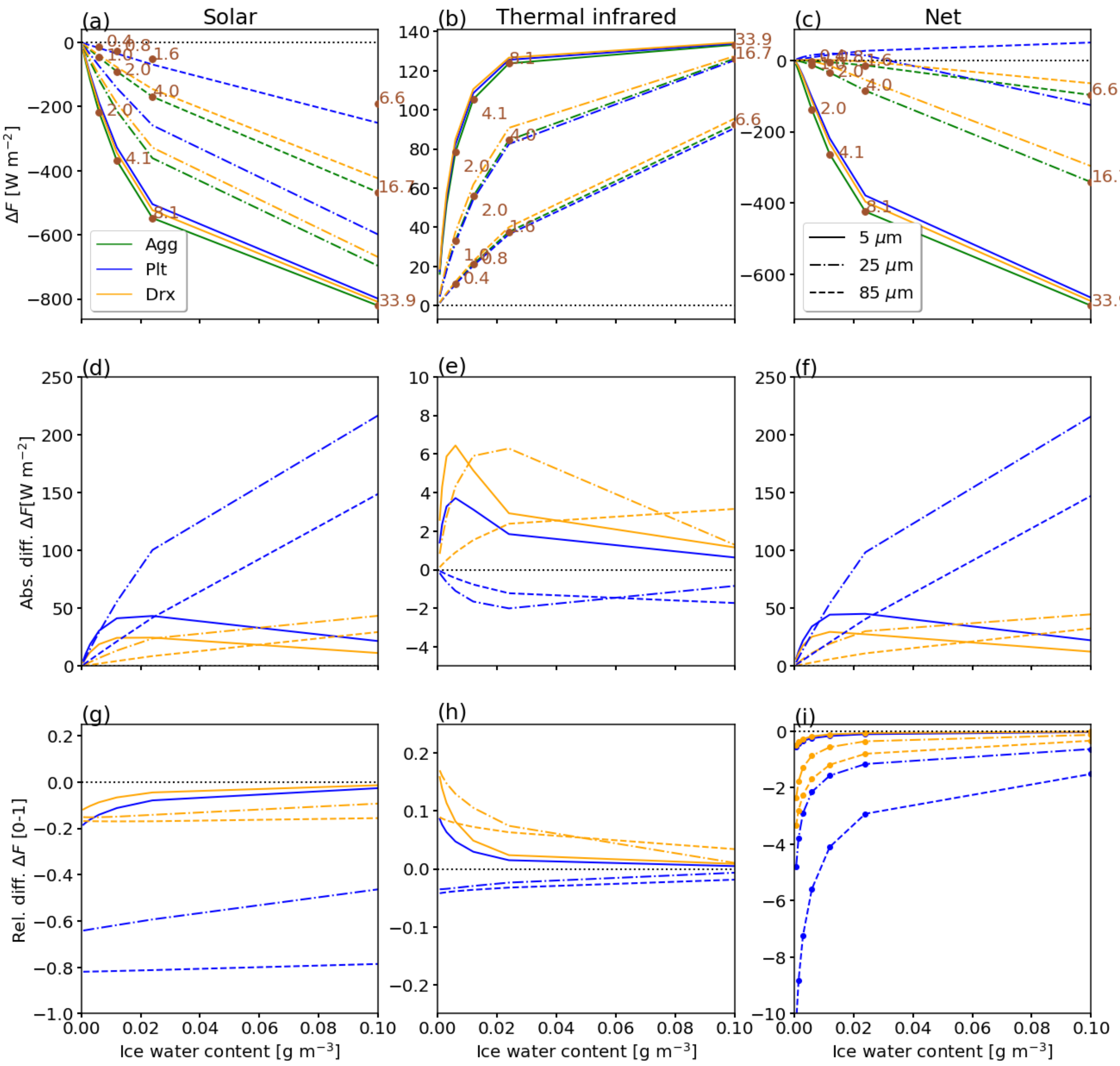

Figure 4. Same as Fig. 3 but for solar zenith angle $\theta = 30^{\circ}$, and ΔF_{sol} (left), ΔF_{tir} (middle), and ΔF_{net} (right).

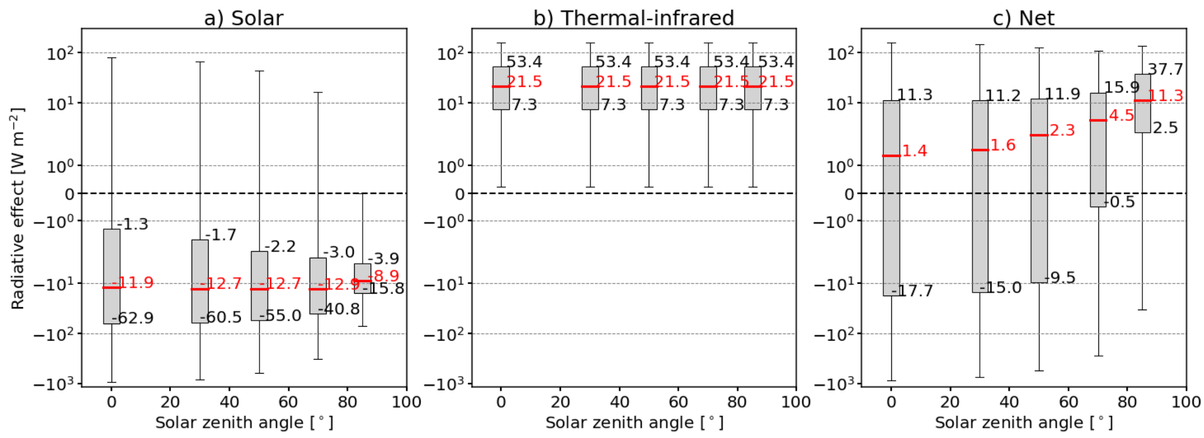

Figure 5. Box plots of **(a)** solar, **(b)** TIR, and **(c)** net ΔF (in W m^{-2}) as a function of the solar zenith angle θ. Median values are indicated in red, the 25 % – 75 % range is represented by the gray boxes, and the 10 % and 90 %-percentiles are given by the whiskers. Red and black numbers indicate the 25$^{\mathrm{th}}$- and 75$^{\mathrm{th}}$ percentiles, and the median value, respectively. Note the logarithmic scale on the y-axis.

3.2 Sensitivity to on solar zenith angle and surface albedo

Variations in θ are caused by the diurnal and seasonal cycle of the Earth, or variations along the longitude at a given time. Figure 5a shows solar ΔF_{sol} at for $\theta = 0°$ with distributions ranging , distributions range from $-$554.7 944.5 W m^{-2} (high IWC) to 35.7 78.0 W m^{-2} (high α_{srf}). For all simulated θ simulated $\theta < 85°$, the median values range from $-$4 11.9 to $-$7.1 12.9 W m^{-2} with an intensification of ΔF_{sol} towards larger θ. The upper boundaries At the same time, the upper maxima of ΔF_{sol} are shifted towards zero, which is a combination of three effects: i) a decreasing downward irradiance at TOA with increasing θ; ii) an increasing optical path length s through the cloud with increasing θ and accompanied the corresponding increase in scattering; and iii) an increased upward scattering increase in upward scattered radiation with increasing θ as the light rays get slanted and a larger fraction of the forward peak radiation from the forward scattering range is directed upwards. Effects i) and ii) compete and are dominated by effect iii). The combination of effects i) –iii to iii) also reduces the inter-quantile for larger θ and indicates a reduced influence of the other free parameters on ΔF_{sol}. However, the smallest ΔF_{sol} is calculated for θ of 85° and is caused by the reduced side-ward scattering of ice crystals.

ΔF_{tir} is unaffected by changes in The value of θ (where ΔF_{sol} is most intense depends on α_{srf} and is typically between 50° and 70° (Markowicz and Witek, 2011). The maximum in ΔF_{sol} and the corresponding θ are explained by the strong forward scattering peak of ice crystals and the resulting weak backscattering (Haywood and Shine, 1997; Myhre and Stordal, 2001). To further elaborate on the response of ΔF_{sol} on large θ, Fig. 5b) with a 6a shows ΔF_{sol} as a function of θ for selected τ_{ice} and α_{srf}. For an optically thick cirrus with $\tau_{\mathrm{ice}} = 1.6$ located over a surface with $\alpha_{\mathrm{srf}} = 0$ (blue, solid curve) the maximum ΔF_{sol} appears around $\theta = 50°$. For the same cloud above a more reflective surface with $\alpha_{\mathrm{srf}} = 0.3$ (blue, dashed curve) the maximum is shifted towards $\theta = 70°$. Further increasing α_{srf} to 1 (blue, dotted curve), solar cooling turns into a heating and the strongest solar cooling is found for the largest θ. Figure 6a also shows that the shift in θ with absolute, maximum ΔF_{sol} is

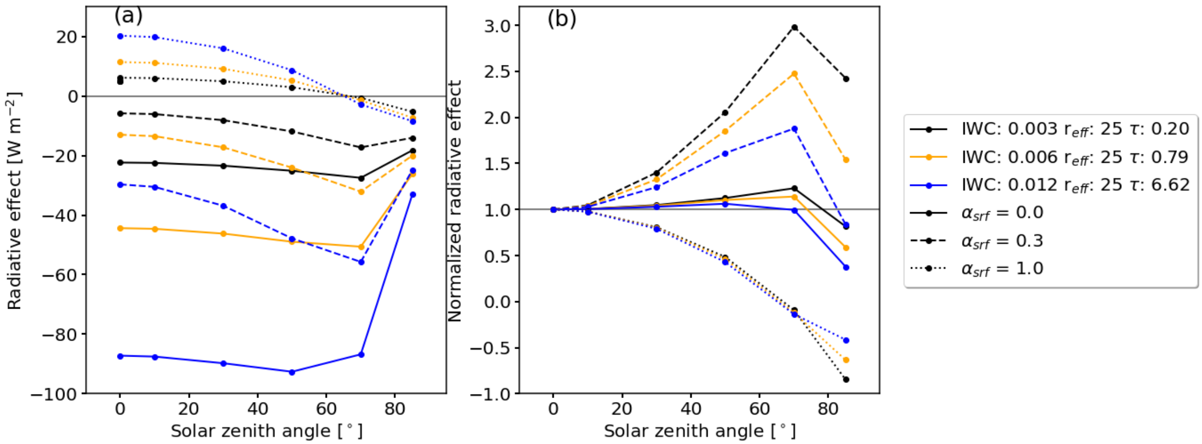

Figure 6. **(a)** Solar radiative effect ΔF_{sol} (in $\mathrm{W\,m^{-2}}$) as function of solar zenith angle θ for three ice clouds with cloud optical thickness τ_{ice} of 0.1, 0.4, and 1.6. Effective radius r_{eff} is given in units of μm and the ice water content IWC in units of $\mathrm{g\,m^{-3}}$. The cloud is located over surfaces with a surface albedo α_{srf} of 0, 0.3, and 1. **(b)** Same as **(a)** but normalized with ΔF_{sol} of each case at $\theta = 0°$.

most pronounced for optically thicker clouds. However, the largest relative change in ΔF_{sol} by varying θ appears for optically thin clouds (Coakley and Chylek, 1975).

Figure 6b shows ΔF_{sol} normalized with the respective ΔF_{sol} at $\theta = 0°$. The sensitivity of normalized ΔF_{sol} on θ is most pronounced for optically thin clouds with $\tau_{\mathrm{ice}} = 0.1$ over a moderately reflective surface ($\alpha_{\mathrm{srf}} = 0.3$) (dashed, black). For this combination, ΔF_{sol} at $\theta = 70°$ is a factor of 3 larger compared to a Sun overhead ($\theta = 0°$). The same cloud over a non-reflective surface ($\alpha_{\mathrm{srf}} = 0$) reduces the sensitivity leading to a factor of 1.2 in relation to ΔF_{sol} at $\theta = 0°$ (solid, black). A similar pattern but with a generally reduced sensitivity is found for the optically thicker cloud case with $\tau_{\mathrm{ice}} = 1.59$. In this case ΔF_{sol} is larger by a factor of 1.05 at $\theta = 50°$ (blue, solid) and larger by a factor of 1.7 at $\theta = 70°$ (blue dashed) with respect to a Sun at $\theta = 0°$. The large sensitivity for optically thin clouds is explained by the dominance of single-scattering, where scattering is strongly dependent on the value of the $\mathcal{P}$ at a given scattering angle. When the cloud becomes optically thicker, multiple-scattering processes start to dominate the RT and $\mathcal{P}$ is averaged over a range of scattering angles, reducing the sensitivity on θ. However, while the sensitivity might be largest for optically thin clouds, the absolute ΔF_{sol} of optically thin clouds is small compared to clouds with higher τ_{ice}.

Figure 5b shows that ΔF_{tir} is unaffected by θ leading to a constant median ΔF_{tir} of ~~8.3~~21.5 $\mathrm{W\,m^{-2}}$. The highest positive values of ΔF_{tir} (strongest warming effect) are found for clouds with maximal IWC. ~~Resulting~~ The resulting ΔF_{net}, ~~given~~ shown in Fig. 5c, is dominated by a warming in the TIR that leads to median ΔF_{net} ~~around 1.0~~between 1.4 $\mathrm{W\,m^{-2}}$ and 11.3 $\mathrm{W\,m^{-2}}$, with ~~minimum~~ a minimum of ΔF_{net} of $-$~~526.5~~872.8 $\mathrm{W\,m^{-2}}$ and maximum of ~~126.9~~160.1 $\mathrm{W\,m^{-2}}$. With increasing θ, ΔF_{net} increases. This is caused by the shift of the lower minima of ΔF_{sol} towards zero, compared to the maxima of ΔF_{sol}, which indicates that a larger fraction of the simulations have a reduced cooling effect. Thus, the fraction of simulations with a positive

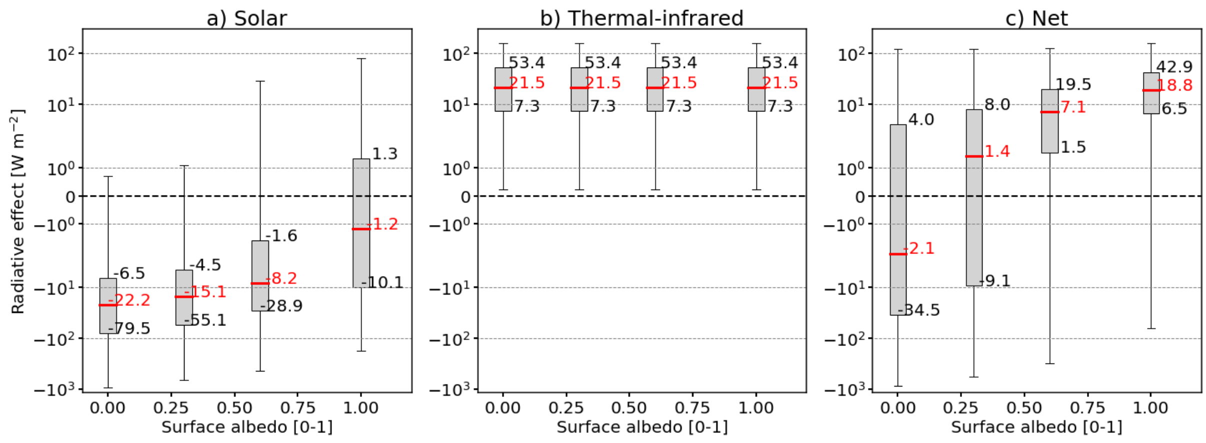

Figure 7. Same as Fig. 5 but as a function of the surface albedo α_{srf}.

ΔF_{net} (net warming) increase. The reduced variability of ΔF_{sol} with increasing θ propagates into the distribution and variability in ΔF_{net}, which is also reduced even though the variability in ΔF_{tir} increase with θ.

The influence of the underlying surface is shown in Fig. 7. For $\alpha_{\mathrm{srf}} = 0$ the surface absorbs the entire incident solar radiation creating the largest contrast between α_{srf} and the cloud albedo α_{cld}. As long as When the surface is fully absorbing ($\alpha_{\mathrm{srf}} = 0$), all simulated cloud combinations are characterized by a cooling in the solar with ΔF_{sol} ranging from $-$554 to 0944.5 to 80 $\mathrm{W\,m^{-2}}$. The cooling is reduced when the surface becomes more reflective and the contrast between surface and cloud is reduced, which shifts the distributions and their medians towards positive ΔF_{sol}. With α_{srf} approaching 0.66, around 25 % of the parameter combinations lead to a solar heating. This becomes even more pronounced towards $\alpha_{\mathrm{srf}} = 1$, where around 50 % of the simulations have yield a warming effect in the solar. ΔF_{tir} is unaffected by changes in α_{srf}, as expected, and remains constant for all α_{srf} with a median at 8.321.5 $\mathrm{W\,m^{-2}}$. Resulting The resulting ΔF_{net} is dominated by a net warming effect, indicated by mostly positive median values ranging from 0.31.4 $\mathrm{W\,m^{-2}}$ ($\alpha_{\mathrm{srf}} = 0.25$) to 8.118.8 $\mathrm{W\,m^{-2}}$ ($\alpha_{\mathrm{srf}} = 1$). An exception is $\alpha_{\mathrm{srf}} = 0$, where more than 50 % of the simulations lead to a net cooling with a median ΔF_{net} at $-$2.92.1 $\mathrm{W\,m^{-2}}$.

3.3 Sensitivity on ice water content and ice crystal radius

As presented in Fig. 2, the IWC is the primary second most influencing factor that controls ΔF. For a constant crystal number concentration the increase in IWC leads to an increase in r_{eff}, as well as the total particle scattering and absorption cross-sections, as well as r_{eff}. This enhances scattering and absorption along the light optical path though the cloud. Figure 8a reveals that with increasing IWC the median of ΔF_{sol} becomes more negative (intensification of the cooling effect in the solar part of the spectrum). The steepest increase is found for IWC < 0.040.012 $\mathrm{g\,m^{-3}}$, while for IWC $\geq$ 0.040.012 $\mathrm{g\,m^{-3}}$ the solar cloud RE saturates. At the same time $Q_{\Delta F,sol}$ $Q_{\Delta F,\mathrm{sol}}$, given by Eq. 16, increases, indicating an enhanced sensitivity of ΔF_{sol} on the free parameters. The minimum and maximum of ΔF_{sol} result from clouds over highly reflective surface (α_{srf} = 1) and clouds containing crystals with the smallest r_{eff} = 5 μm.

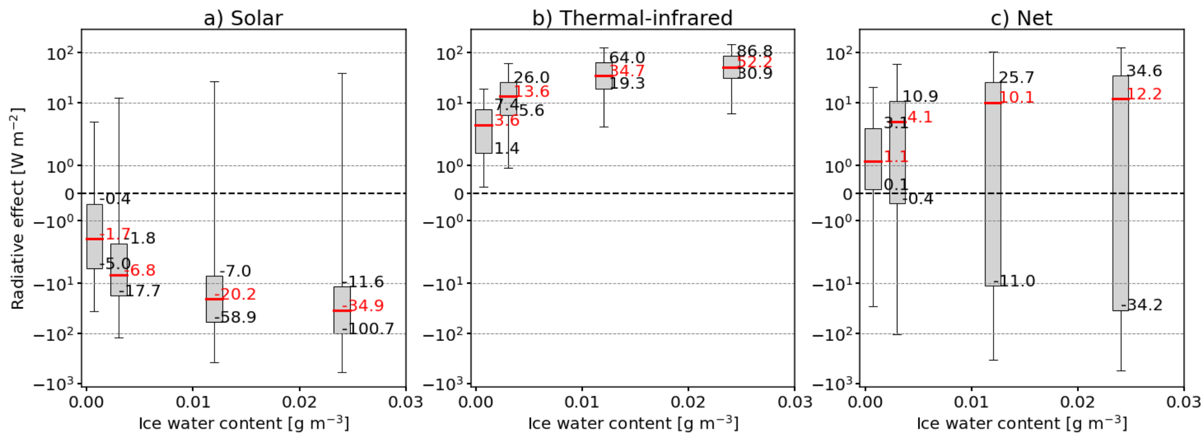

Figure 8. Same as Fig. 5 but as a function of ice water content IWC (in g m^{-3}). For better legibility only IWC up to 0.03 g m^{-3} are plotted.

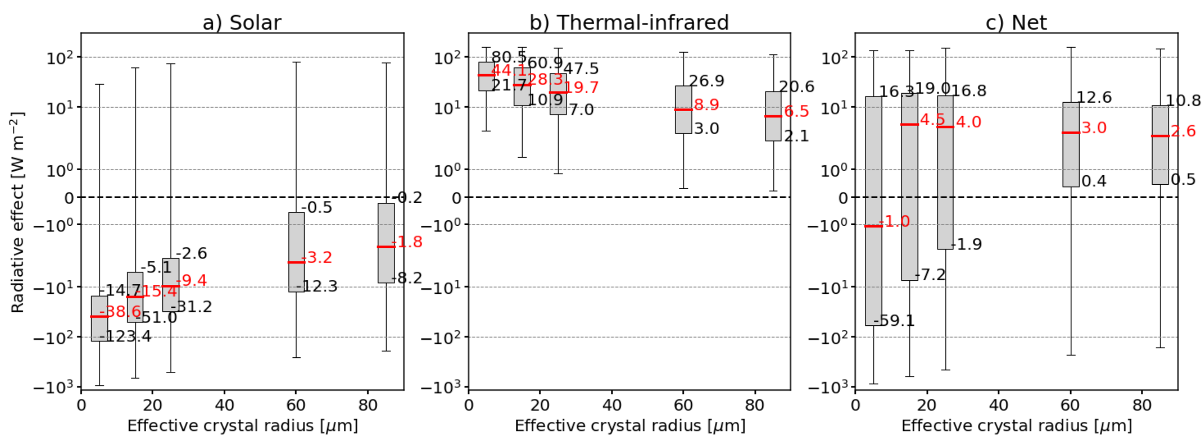

Figure 9. Same as Fig. 5 but as a function of effective crystal radius r_{eff} (in μm).

For ΔF_{tir} the increase in IWC leads to an intensified warming effect (Fig. 8b). Again, this is caused by the increase in the total particle scattering and absorption cross-sections. ~~Similar~~ Similarly to ΔF_{sol}, the steepest increase appears for IWC < ~~0.04~~0.012 g m^{-3}, while for larger IWC the medians approach an almost constant level and a further increase in IWC has only a limited effect on ΔF_{tir}. ~~Beyond an IWC of 0.04 g m^{-3} the photon mean free path in the cloud becomes smaller than the geometric thickness of the cloud and a further increase in IWC (τ_{ice}) has an almost negligible impact on the cloud RE in the solar and TIR.~~ The resulting ΔF_{net} (Fig. 8c) ranges from −~~526.5 to 126.9~~543.2 to 125.5 W m^{-2} and is skewed to positive ΔF_{net} with median values between ~~−2.8 and 3.6~~1.1 and 12.2 W m^{-2}.

The size of ice crystals also influence the cloud RE, with a larger sensitivity of ΔF_{sol} on r_{eff} than ΔF_{tir} (Baum et al., 2005b) . Figure 9 illustrates that cirrus with the smallest r_{eff} are associated with the most intense cooling effect in the solar, leading to ΔF_{sol} between −~~554.7 and 19.1~~944.5 and 80.0 W m^{-2}. Small crystals and high number concentrations lead to higher

$\alpha_{\text{cld,ice}}$ in the solar compared to fewer and larger crystals (Stephens et al., 1990; Zhang et al., 1994). For the smallest crystals in the simulations ~~a median value of~~ the median ΔF_{sol} is $-$~~24.4~~38.6 $\text{W}\,\text{m}^{-2}$ is determined. For increasing ~~crystal radius~~ r_{eff} the cooling effect in the solar range decreases and tends towards a ~~neutral~~ weak solar RE (ΔF_{sol} = $-$~~1.3~~1.8 $\text{W}\,\text{m}^{-2}$). Increasing r_{eff}, while keeping the IWC constant, ~~is directly linked~~ leads to a decrease in ~~the~~ ice crystal number concentration (cloud albedo effect). ~~Clouds~~ In addition, ice crystals with larger r_{eff} have an increased forward scattering. Hence, less radiation is scattered to the sides or backwards into space. Figure 9 shows that clouds with larger r_{eff} are found to be less sensitive to the effect of the free parameters as the inter-quartile range decreases ~~from $Q_{\Delta\text{F,sol}}(r_{\text{eff}} = 5\,\mu\text{m}) = 73.1\,\text{W}\,\text{m}^{-2}$ to $Q_{\Delta\text{F,sol}}(r_{\text{eff}} = 45\,\mu\text{m}) = 6.6\,\text{W}\,\text{m}^{-2}$~~ strongly from $Q_{\Delta\text{F,sol}}(r_{\text{eff}} = 5\,\mu\text{m}) = 108.7\,\text{W}\,\text{m}^{-2}$ to $Q_{\Delta\text{F,sol}}(r_{\text{eff}} = 85\,\mu\text{m}) = 8.0\,\text{W}\,\text{m}^{-2}$. Similarly, the strongest TIR heating occurs for the ~~smallest crystals as such small crystals~~ highest N_{ice} / smallest crystals. Such clouds have the largest ~~emissivity (Stephens et al., 1990; Zhang et al., 1994). An~~ total absorption cross-section and act almost as blackbodies (Stephens et al., 1990; Zhang et al., 1994). However, an increase in r_{eff} while fixing IWC leads to a reduction in ΔF_{tir}, which is caused by the lower total particle scattering and ~~particle~~ absorption cross-sections. $Q_{\Delta\text{F,tir}}$ decreases from 58.8 $\text{W}\,\text{m}^{-2}$ for ~~$r_{\text{eff}} = 5\,\mu\text{m}$ decreases from 37.9 to 11.3~~ $r_{\text{eff}} = 5\,\mu\text{m}$ to 18.5 $\text{W}\,\text{m}^{-2}$ for $r_{\text{eff}} = 85\,\mu\text{m}$. Median values of ΔF_{net} indicate only a net cooling for $r_{\text{eff}} = 5\ \mu\text{m}$ with $-$~~3.4~~1 $\text{W}\,\text{m}^{-2}$, whereby elsewhere a net warming is dominant with ΔF_{net} ~~around 1.4~~ between 2.6 and 4.5 $\text{W}\,\text{m}^{-2}$. Simultaneously, $Q_{\Delta\text{F,net}}$ slightly decreases, which indicates the reduced impact of the remaining free parameters. The presented dependencies, especially for small r_{eff}, of solar, TIR, and net ΔF on r_{eff} and IWC agree with previous studies, e.g., from Hansen and Travis (1974), but particularly Fu and Liou (1993) and Zhang et al. (1999).

3.4 Multi-dimensional dependencies on θ, α_{srf}, r_{eff}, and IWC

The previous analysis aimed to sample the 8D-hypercube in a series of 1D–cross-sections to focus on the general distribution of ΔF that result from a single parameter. This likely masks dependencies of ΔF on specific parameter combinations that are closely interconnected. Subsequently, we focus on a detailed analysis, particularly in the solar wavelength range, to highlight the dependencies among Sun geometry, surface albedo, and cloud properties - ~~namely~~ especially r_{eff} and IWC.

3.4.1 Solar radiative effect

Figure 10 shows ΔF_{sol} as a function of IWC and r_{eff} for combinations of α_{srf} (~~column~~columns) and θ (~~row~~rows). Moving from the left to the right column the surface becomes more reflective (increasing α_{srf}) and going from the top to the bottom row the Sun approaches the horizon (increasing θ). ~~The panels along the diagonal can be understood as a transition from the Equator ($\theta \approx 0°$, $\alpha_{\text{srf}} \approx 0$) towards the Poles with low Sun ($\theta \approx 70°$) with an increase in sea ice cover ($\alpha_{\text{srf}} \approx 1$).~~

Figure 10a represents non-reflective surfaces and a Sun at the zenith. In these cases and focusing on ice crystals with $r_{\text{eff}} >$ ~~20~~30 μm the contour lines are well separated. A wide spacing of the contour lines indicates a low sensitivity of ΔF_{sol} on IWC and r_{eff}. In those regions ΔF_{sol} ranges from 0 to $-$~~80~~450 $\text{W}\,\text{m}^{-2}$ (cooling), with an intensification of ΔF_{sol} for decreasing r_{eff}. Simultaneously, the contour lines ~~narrow~~ get closer and align with the x-axis, which indicates an increase in the sensitivity of ΔF_{sol}, particularly with respect to r_{eff}, as it is expected from Fig. 2.

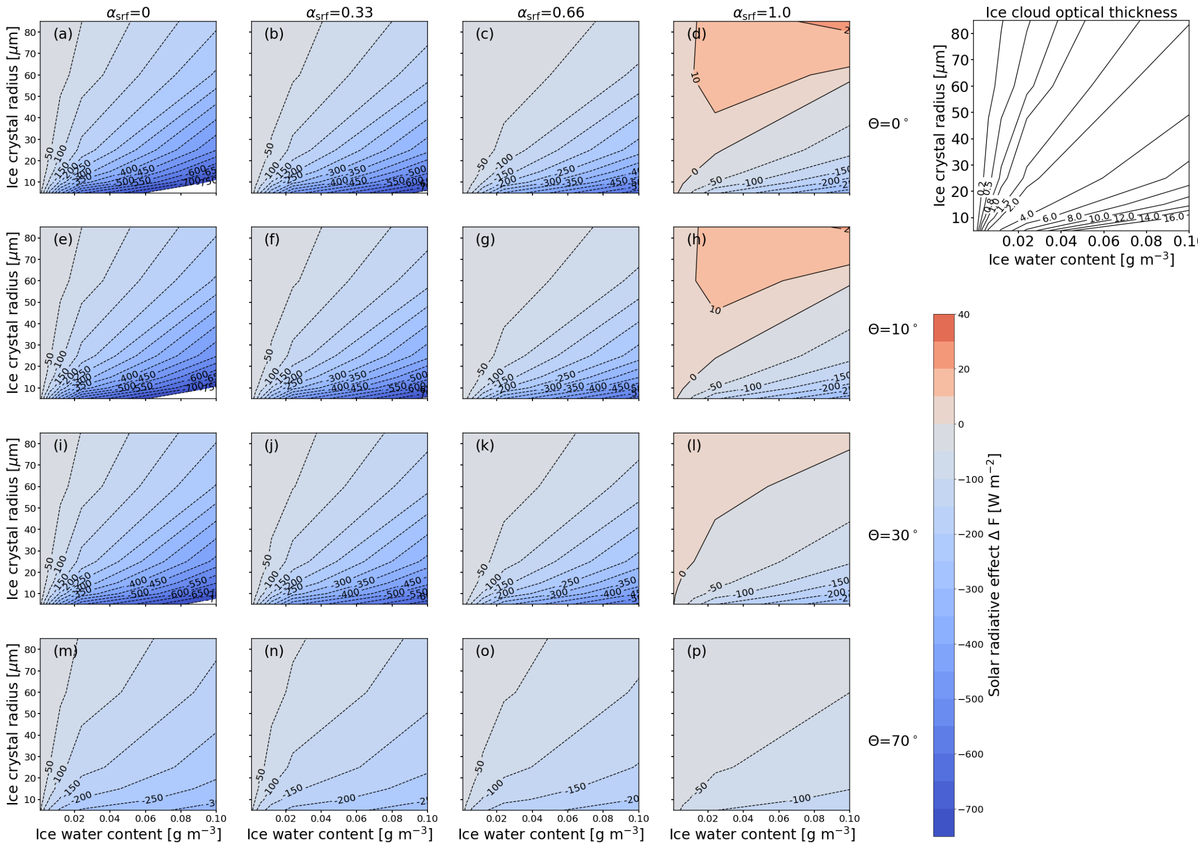

Figure 10. Solar cloud radiative effect ΔF_{sol} in $W\,m^{-2}$ sampled into two-dimensional parameter space of ice water content IWC (in $g\,m^{-3}$) and effective radius r_{eff} (in μm). Each panel represents combinations of surface albedo α_{srf} ~~at 550 nm~~ and solar zenith angle θ. Blue values indicate negative ΔF_{sol} (cooling) and red values indicate positive (warming) ΔF_{sol}. The contour lines provide a direct measure of the sensitivity to the indicated parameters. The top-right panel shows, for reference, the cloud optical depth that corresponds to the combinations of r_{eff} and IWC shown on the other panels.

For the Sun at zenith and cirrus above reflective surfaces ($0 < \alpha_{srf} < 1$), the sensitivity with respect to IWC and r_{eff} is generally reduced. This results from the increasing contribution of surface reflected, upward irradiance, which progressively dominates ΔF_{sol} of the cirrus. ΔF_{sol} is essentially a measure of the contrast between α_{srf} and $\alpha_{cld,ice}$, with $\alpha_{cld,ice}$ mostly dependent on r_{eff} and IWC. In case of a highly reflective surface ($\alpha_{srf} \geq 0.6$; Fig. 10d) the predominant cooling in the solar spectrum turns into a warming effect for most of the combinations with ΔF_{sol} up to 15–20 $W\,m^{-2}$. Only ice clouds with r_{eff} < ~~10~~20–30 μm and IWC ≈ ~~0.1~~0.04–0.1 $g\,m^{-3}$, i.e., high ~~$\tau > 3$, are still~~ $\tau_{ice} > 3$, are more reflective than the surface. Such combinations of r_{eff} < ~~10~~20 μm and IWC ≈ ~~0.1~~0.04–0.1 $g\,m^{-3}$ are associated with ice crystal number concentrations that are rarely observed in nature except for some cases of contrails (see Fig. 1 in Krämer et al. (2016)).

For cirrus over non-reflective or slightly reflective surfaces ($\alpha_{\mathrm{srf}} \leq 0.33$) and the Sun at intermediate SZA ($\theta \geq 30°$), the contour lines separate and the sensitivity of ΔF_{sol} on r_{eff} and IWC is reduced. For ~~sun~~ Sun positions closest to the horizon ($\theta = 70°$) and above highly reflective surfaces ($\alpha_{\mathrm{srf}} = 1$), ΔF_{sol} is characterized by a generally low sensitivity over the entire range of IWC and r_{eff} (Fig. 10p). In spite of the warming effect for $\alpha_{\mathrm{srf}} = 1$ and $\theta \leq 30°$, the slant optical path of the incident radiation through the cloud reduces the surface influence and leads to a cooling effect with ΔF_{sol} in the range of -5 to $-$~~80~~100 W m^{-2}.

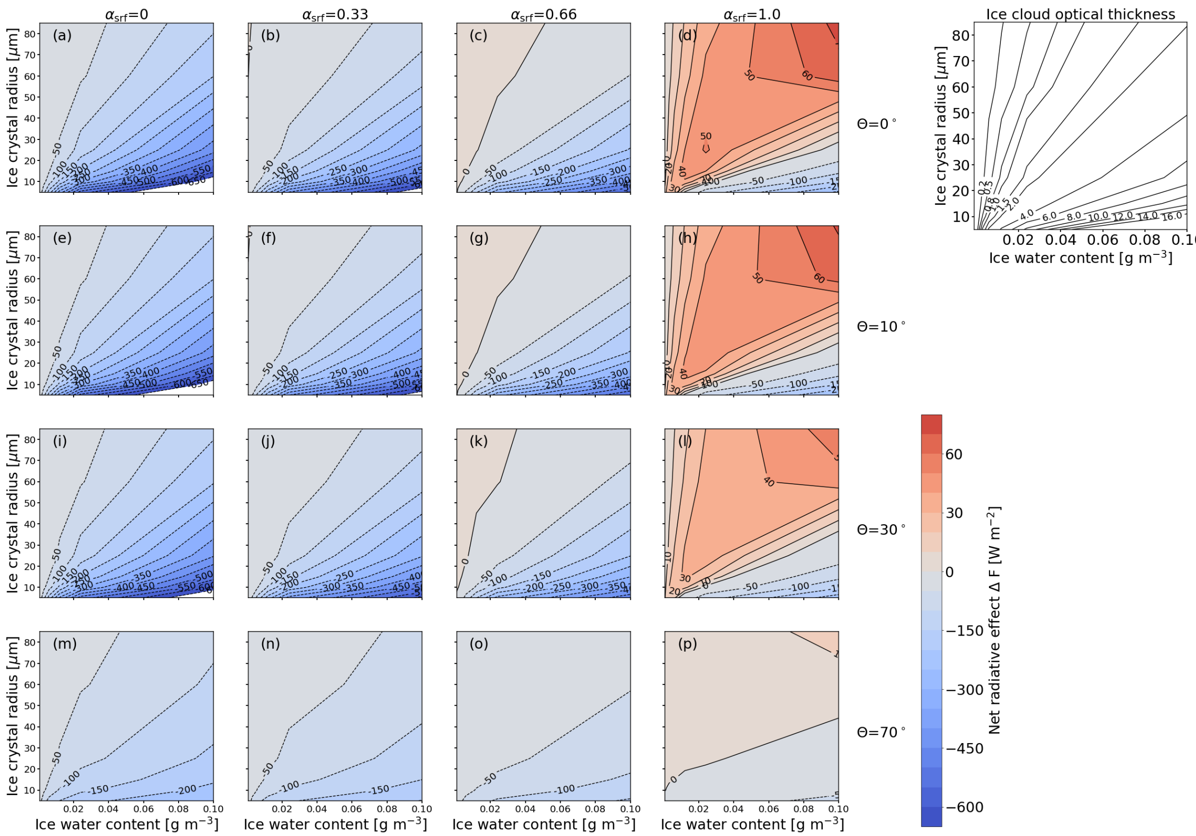

Figure 11. Same as Fig. 10 but for ΔF_{net} (in W m^{-2}).

3.4.2 Thermal-infrared and net radiative effect

The TIR component of ΔF is insensitive to changes in θ and α_{srf}, and only combinations of IWC and r_{eff} are of relevance. In the TIR, the surface is approximated by a blackbody with a wavelength independent emissivity equal to one. The resulting distributions of ΔF_{net}, shown in Fig. 11, are dominated by the contribution of ΔF_{sol} and, therefore, are characterized by similar sensitivities. The strongest gradient of ΔF_{net} on IWC and r_{eff} are found for $\theta \approx 0°$ and $\alpha_{\mathrm{srf}} = 0$ (Fig. 11a). With increasing α_{srf}, ΔF_{net} is positive for the majority of the combinations of IWC and r_{eff} (Fig. 11c). The net warming is most

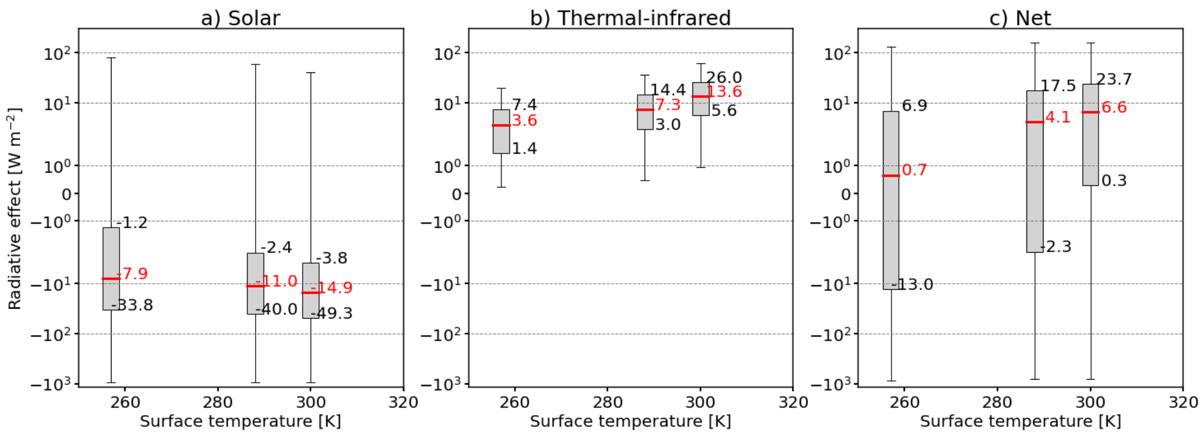

Figure 12. Same as Fig. 5 but for surface temperature T_{srf} (in K).

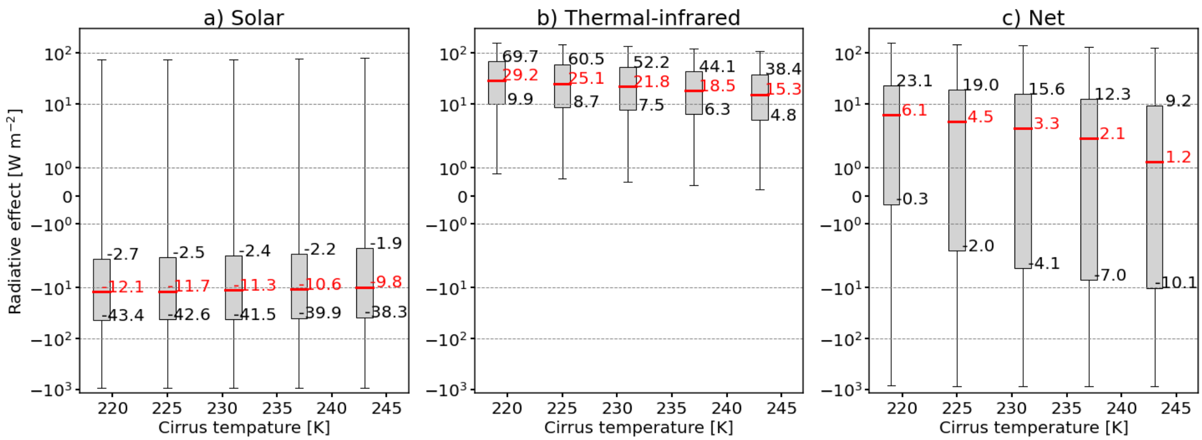

Figure 13. Same as Fig. 5 but for ice cloud temperature $T_{\mathrm{cld,ice}}$ (in K).

pronounced for $\alpha_{\mathrm{srf}} = 1$ (Fig. 11d). It is further noted that for $\alpha_{\mathrm{srf}} = 1$ and high Sun (~~$\theta \leq 40°$~~$\theta \lesssim 30°$), ΔF_{net} is positive and almost exclusively sensitive to IWC. Conversely, regions that have a net cooling effect, i.e., at high N_{ice} values, are exclusively sensitive to r_{eff}. The cloud can have a net cooling effect, when the Sun is close to horizon (Fig. 11p), with almost no sensitivity to r_{eff} and IWC.

3.5 Sensitivity on atmospheric profile, surface temperature~~and~~ , relative humidity, ice cloud altitude, and ice cloud geometric thickness

~~Any variations in the surface temperature T_{srf} or ice cloud temperature $T_{\mathrm{cld,ice}}$ (with associated cloud altitude z) leave ΔF_{sol} unaffected (Fig. 12a~~ Within this study, the atmospheric profiles, the surface temperatures T_{srf}, as well as the vertical location of the ice cloud are coupled. While T_{srf} are selected to match the lowermost T of the respective AP, the vertical position of the cloud depends on the temperature of the AP and the selected cloud top temperature $T_{\mathrm{cld,ice}}$ (see Appendix B and Fig. 13a). Negligible differences in the medians of B1a,b therein). Figure 12a shows that variations in the surface temperature T_{srf} have an effect on ΔF_{sol} with differences in median ΔF_{sol} of up to ± 27 $\mathrm{W\,m^{-2}}$are . These are traced back to: a) the different optical path length through the atmosphere because of variations in the cloud top altitude; and b) the different water vapor concentration due to the variation in the humidity profilethree applied APs. The two effects can be partly separated by varying T_{srf}. Figure 13a shows that ΔF_{sol} is slightly impacted by variations in the cirrus temperature with difference in median ΔF_{sol} of ± 2 $\mathrm{W\,m^{-2}}$. These differences solely result from different clout top altitudes and resulting optical path length through the atmosphere above the cloud.

Generally larger effects are found for the TIR component. Increasing T_{srf} andtherefore , therefore, the temperature difference between surface and cirrus leads to an intensification of the TIR heating effect (see Eq. ??)(Corti and Peter, 2009). The median is shifted from 1.2 to 4.53.6 to 13.6 $\mathrm{W\,m^{-2}}$ (Fig. 12b). Simultaneously, the distributions broaden with $Q_{\Delta \mathrm{F,tir}}$ ranging from 1.9 to 6.86.0 to 21.0 $\mathrm{W\,m^{-2}}$, which results from the warmer and moister tropical profile used in combination with $T_{\mathrm{srf}} = 313$$T_{\mathrm{srf}} = 300$ K compared to the dryer Arctic drier Subarctic profile. As a result of the almost constant ΔF_{sol} and the increase in ΔF_{tir}, the net heating effect is enhanced with medians ranging between 0.5 and 3.40.7 and 6.6 $\mathrm{W\,m^{-2}}$.

Same as Fig. 5 but for ice cloud temperature $T_{\mathrm{cld,ice}}$. A similar effect is found for the variation in $T_{\mathrm{cld,ice}}$ that is presented in Fig. 13. With decreasing $T_{\mathrm{cld,ice}}$ (increase in cloud base altitude), Increasing $T_{\mathrm{cld,ice}}$ reduces the temperature difference between $T_{\mathrm{cld,ice}}$ and T_{srf} is increased, and reinforces surface and ice cloud, and therefore the TIR heating effect. The median Median ΔF_{tir} increases from 5.3 to 11.9are reduced from 29.2 to 15.3 $\mathrm{W\,m^{-2}}$and for ΔF_{net} from 0.2 to 2.1 $\mathrm{W\,m^{-2}}$, when $T_{\mathrm{cld,ice}}$ is increased from 219 to 243 K. Compared to the impact of T_{srf}, which was varied over a range of 8047 K, shifting the cloud in the vertical has only a minor effect on ΔF_{tir} and ΔF_{net}, as the variation in $T_{\mathrm{cld,ice}}$ spanned only 2724 K. The resulting net effect from variations in T_{srf} and $T_{\mathrm{cld,ice}}$ ranges between medians of 0.7 and 6.6 $\mathrm{W\,m^{-2}}$ as well as 1.2 and 7.7 $\mathrm{W\,m^{-2}}$, respectively.

The effect of varying RH profiles are investigated by manipulating the original RH profiles by $\pm 20\,\%$ representing the variability in RH reported by Anderson et al. (1986). The RT simulations are performed for a sub-set of the parameter space with fixed $T_{\mathrm{cld,ice}} = 231$ K, $\alpha_{\mathrm{srf}} = 0$, and $\tau_{\mathrm{liq}} = 0$. The effects on solar, TIR, and net ΔF are quantified by their median values. Variations in RH have only a small effect on ΔF_{sol} with maximal ± 0.15 $\mathrm{W\,m^{-2}}$ ($\pm 0.4\,\%$). A slightly larger impact is found for ΔF_{tir} with up to ± 1.45 $\mathrm{W\,m^{-2}}$ ($\pm 4.1\,\%$) for the warmest and moist tropical profile (`afglt`). Less affected are the standard atmosphere (`afglus`), which varies by ± 0.9 $\mathrm{W\,m^{-2}}$ ($\pm 3.2\,\%$) and the dry Subarctic profile (`afglsw`) by ± 0.3 $\mathrm{W\,m^{-2}}$ ($\pm 2.4\,\%$). Consequently, `afglt` has the largest variation in ΔF_{net} of ± 0.8 $\mathrm{W\,m^{-2}}$ ($\pm 8\,\%$) and is followed by ± 0.6 $\mathrm{W\,m^{-2}}$ ($\pm 3.8\,\%$) for `afglus` and ± 0.2 $\mathrm{W\,m^{-2}}$ ($\pm 0.6\,\%$) for `afglsw`. Scaling the original RH profiles shows that variations on the RH profile explicitly influence the TIR wavelength range and have an even larger, relative impact on ΔF_{net} due to small absolute values. Note that the given absolute values in solar, TIR, and net ΔF are not directly comparable with the values given for the full set of the simulations as the samples from which the medians are calculated differ. Only the relative values provide a measure for the potential impact. This analysis suggests that the variations in RH have to be considered as potential source of variability, when using this publicly available data set.

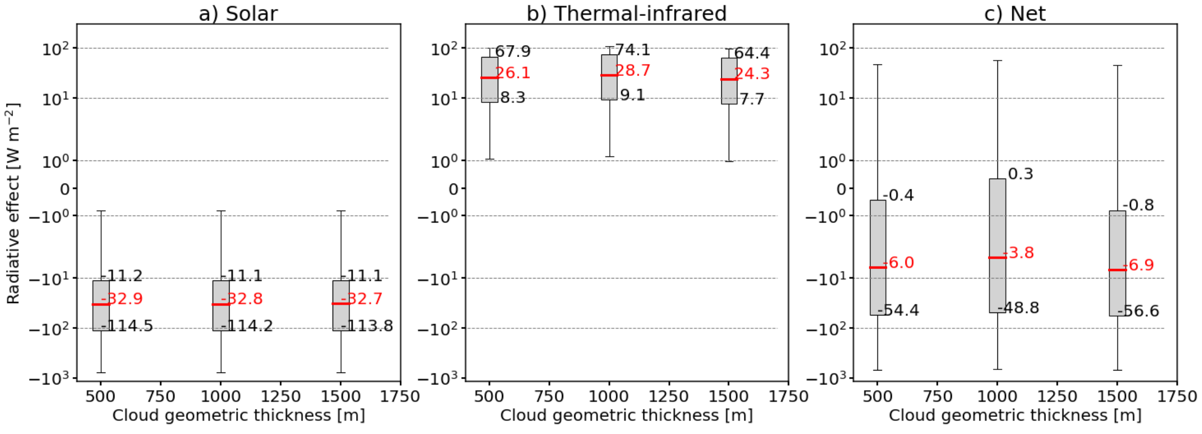

Figure 14. Same as Fig. 5 but for the cloud geometrical thickness dz (in m) and only for a sub sample of the parameter space. Values for ice cloud temperature T_{ice} = 231 K, surface temperature T_{srf} = 288 K, surface albedo $\alpha_{\mathrm{srf}} = 0.15$, and liquid water cloud optical thickness τ_{liq} = 0. Values for solar zenith angle θ, ice water content IWC, and effective radius r_{eff} are varied.

All simulations within this study are performed for a fixed cloud geometric thickness dz of 1000 m. In reality however, dz is likely to vary over the cirrus lifetime, for example due to sedimentation of ice crystals or vertical winds. The effect of changing dz is quantified by a dedicated sensitivity analysis of ΔF for a sub-sample of the full parameter range (Table 4). A similar sub-parameter space is used as for the RH sensitivity but additionally fixing T_{srf} = 288 K, i.e., using the `afglus` profile. With τ_{ice} being proportional to the IWP of the cloud (Eq. 10), the IWP of the 1000 m reference cloud and solar τ_{ice} are kept constant, and the IWC for the clouds with dz of 500 and 1500 m clouds is scaled accordingly.

As expected from Eq. 10, the resulting effect on median ΔF_{sol}, given in Fig. 14, is almost negligible with $\pm$0.1 W m^{-2} ($\pm$0.3 %). Differences in median ΔF_{tir} are up to $\pm$0.6 W m^{-2} ($\pm$3.5 %), which leads to differences in median ΔF_{net} of $\pm$0.6 W m^{-2} ($\pm$6.2 %). The relevant relative differences in ΔF_{tir} and ΔF_{net} are explained by the varying cloud base altitude, which modifies the vertical distribution of IWC and the temperature of the cloud base, which determines the amount of emitted radiation. In addition, geometrically thin clouds with low τ_{ice} act as gray bodies, while with an increase in dz cirrus become opaque and act as more efficient black bodies (Corti and Peter, 2009). Fu and Liou (1993) further reported that cirrus with small r_{eff} reflect solar radiation at the cloud top (solar cooling) but absorb TIR radiation at the cloud base (TIR warming), which creates a temperature gradient within the cloud that depends on dz. From the dz sensitivity analysis it is found that dz can be neglected in the solar wavelength range but is of relevance for ΔF_{tir} and especially ΔF_{net}, where absolute values are small. While Meerkötter et al. (1999) showed that solar, TIR, and net ΔF are only slightly sensitive to changes in dz – under the premise of a constant ice water path (IWP) – the present simulations indicate that the effects on ΔF_{tir} and particularly ΔF_{net} have to be considered.

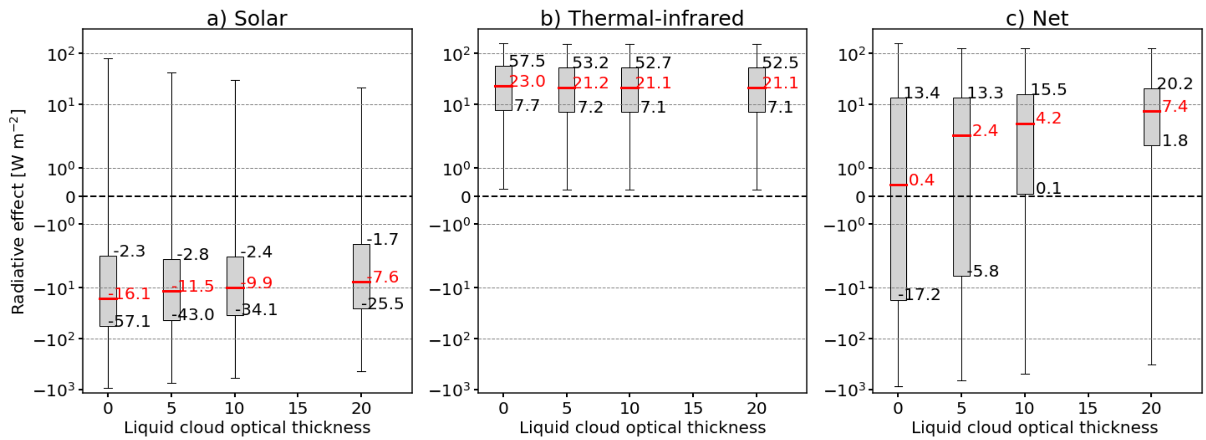

Figure 15. Same as Fig. 5 but for the underlying liquid water cloud optical thickness ~~τ_{wc}~~τ_{liq}.

3.6 Sensitivity on underlying liquid water cloud

The impact of an additional liquid water cloud on the cirrus ΔF is presented in Fig. 15. A liquid water cloud optical thickness ~~$\tau_{\text{wc}} = 0$~~ $\tau_{\text{liq}} = 0$ is equivalent to the absence of secondary clouds and such conditions lead to the strongest ΔF_{sol} with a median of $-$~~5.7~~16.1 W m^{-2}. By gradually increasing ~~τ_{wc}~~ τ_{liq} the reflected, upward irradiance overlays and masks the impact of the surface. In general, the response of ΔF_{sol} on ~~τ_{wc}~~ τ_{liq} is comparable to that of an increase in α_{srf}. Introducing a cloud with ~~$\tau_{\text{wc}} = 5$~~ $\tau_{\text{liq}} = 5$ slightly enhances the cooling in the solar spectrum ΔF_{sol} from $-$~~5.7~~ 11.5 to $-$~~6.5~~7.6 W m^{-2}. More ~~relevant~~ notable is the reduction in the variability of ΔF_{sol} with the distribution becoming narrower and reducing $Q_{\Delta\text{F,sol}}$ from $-$~~34.3~~54.8 W m^{-2} to ~~25.2 W m^{-2}. The smallest variance is found for $\tau_{\text{wc}} = 20$ with $Q_{\Delta\text{F,sol}} = -11.9$ W m^{-2} and a median of $-$2.9~~23.8 W m^{-2}~~as the cloud almost entirely suppresses any contribution from the underlying surface~~.

An increase in ~~τ_{wc}~~ τ_{liq} from 0 to ~~20 results in a minor response of ΔF_{tir}, shifting the median from 8 to 8.3~~5 shifts the median ΔF_{tir} from 21.1 to 23.0 W m^{-2}~~and decreasing~~. With a further increase in τ_{liq} the medians remain almost constant, while the $Q_{\Delta\text{F,tir}}$ ~~at the same time~~slightly decreases. The reduction of maximum ΔF_{tir} is a consequence of the attenuated temperature difference ΔT between the liquid water cloud and the ice cloud compared to the surface. The effect on ΔF_{tir} is small as the change in temperature from surface to liquid water cloud is small. In the case of the US standard atmosphere, where $\Delta T = 5$ K.

As a result of the reduced cooling in the solar spectrum and the stronger warming in the TIR spectrum, the net heating of the ice clouds intensifies with increasing τ_{liq}. The median ΔF_{net} is shifted from 0.4 to ~~3.0~~7.4 W m^{-2} with an accompanying decrease in the overall variance. While for ~~τ_{wc}~~ $\tau_{\text{liq}} < 5$ ~~about~~ slightly fewer than 50 % of the combinations ~~comprised~~ exert a potential net cooling by the cirrus, positive ΔF_{net} is dominating for larger ~~τ_{wc}~~τ_{liq}.

Figure 16 shows ΔF_{sol} depending on IWC and r_{eff} separated for α_{srf} (columns) and ~~τ_{wc}~~ τ_{liq} (rows). In the presented cases, a $\theta = 10°$ is selected as the influence of the surface and an additional cloud layer is of higher importance, when the Sun is close to the zenith. Due to the selection of θ, the top row in Fig. 16 is the same as the second row in Fig. 10 with similar characteristic

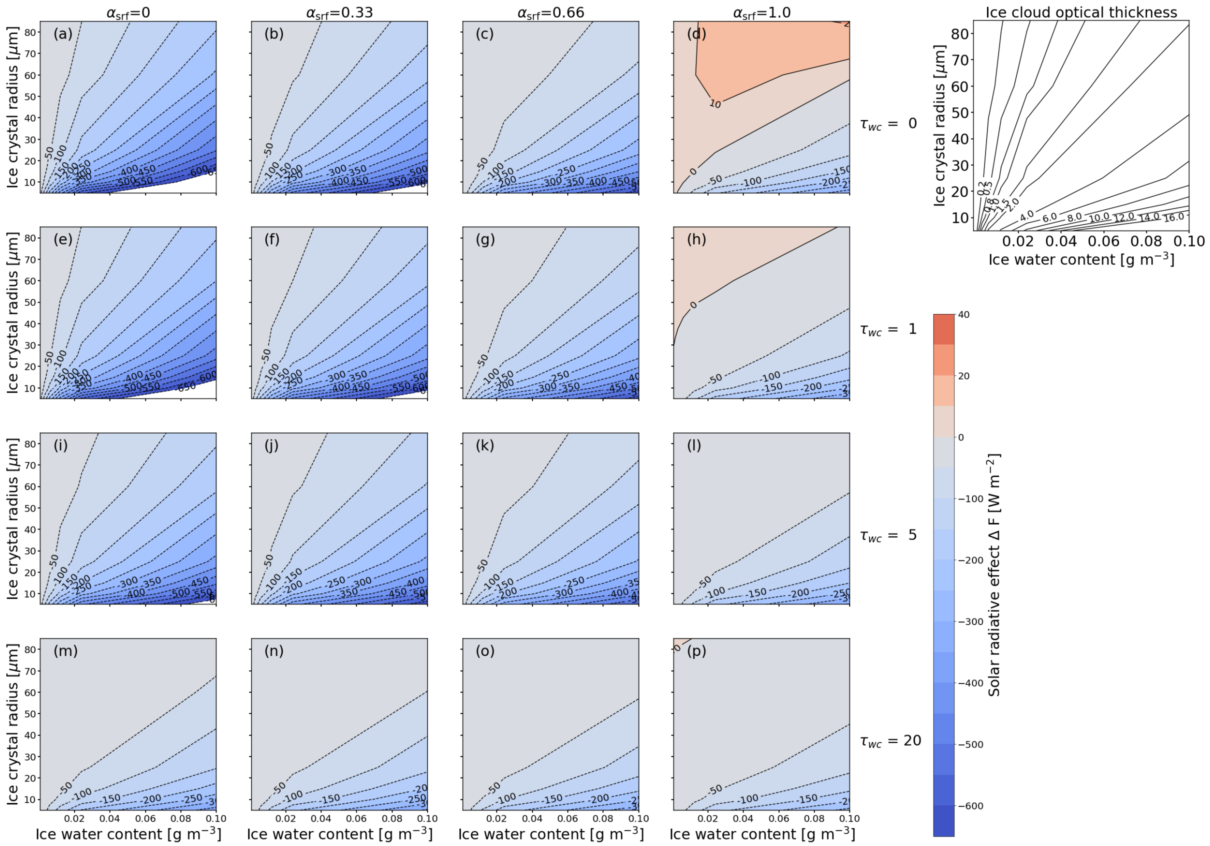

Figure 16. Same as Fig. ~~11~~ 10 but ΔF_{sol} (in $\mathrm{W\,m^{-2}}$) and combinations of surface albedo α_{srf} and cloud optical thickness τ_{liq} of the underlying liquid water cloud.

features in distribution and sensitivity: largest RE appears over dark surfaces ($\alpha_{\mathrm{srf}} = 0$) in combination with clouds containing the largest ice number concentrations N_{ice} due to small r_{eff} and larger IWC. ~~Over non-reflective surfaces, ΔF_{sol} is negative for all combinations and with increasing α_{srf} the warming in the solar range dominates (ΔF_{sol} up to 15 $\mathrm{W\,m^{-2}}$; Fig. 16d).~~ Introducing the second cloud layer and gradually increasing the ~~τ_{wc}~~ τ_{liq} turns the previous solar warming to a cooling effect of around $\Delta F_{\mathrm{sol}} = -15\ \mathrm{W\,m^{-2}}$ for the majority of the parameter combinations. Within those regions the second cloud layer also reduces the sensitivity on the ice cloud microphysical properties. Only cirrus with high N_{ice} can lead to a cooling of up to $\Delta F_{\mathrm{sol}} = -80\ \mathrm{W\,m^{-2}}$.

As shown in Fig. 15 the second cloud layer, at ~~$z = 3$ km~~ $z = 3000$ m modifies ΔF_{tir} only slightly and multi-dimensional dependencies with respect to IWC, r_{eff}, α_{srf}, and ~~τ_{wc}~~ τ_{liq} are weak leading to homogeneous distributions (not shown here). Figure 17 illustrates the variations in ΔF_{net}. For combinations of $\alpha_{\mathrm{srf}} \leq 0.66$ and $\tau_{\mathrm{ice}} \leq 5$, ΔF_{net} is determined by the solar component and its sensitivities. Special attention should be given to conditions with $\alpha_{\mathrm{srf}} > 0.66$ and $\tau_{\mathrm{ice}} > 5$, where ΔF_{net} turns from a cooling into a warming effect. This is due to the reduced ΔF_{sol} and the domination by ΔF_{tir}. In these situations

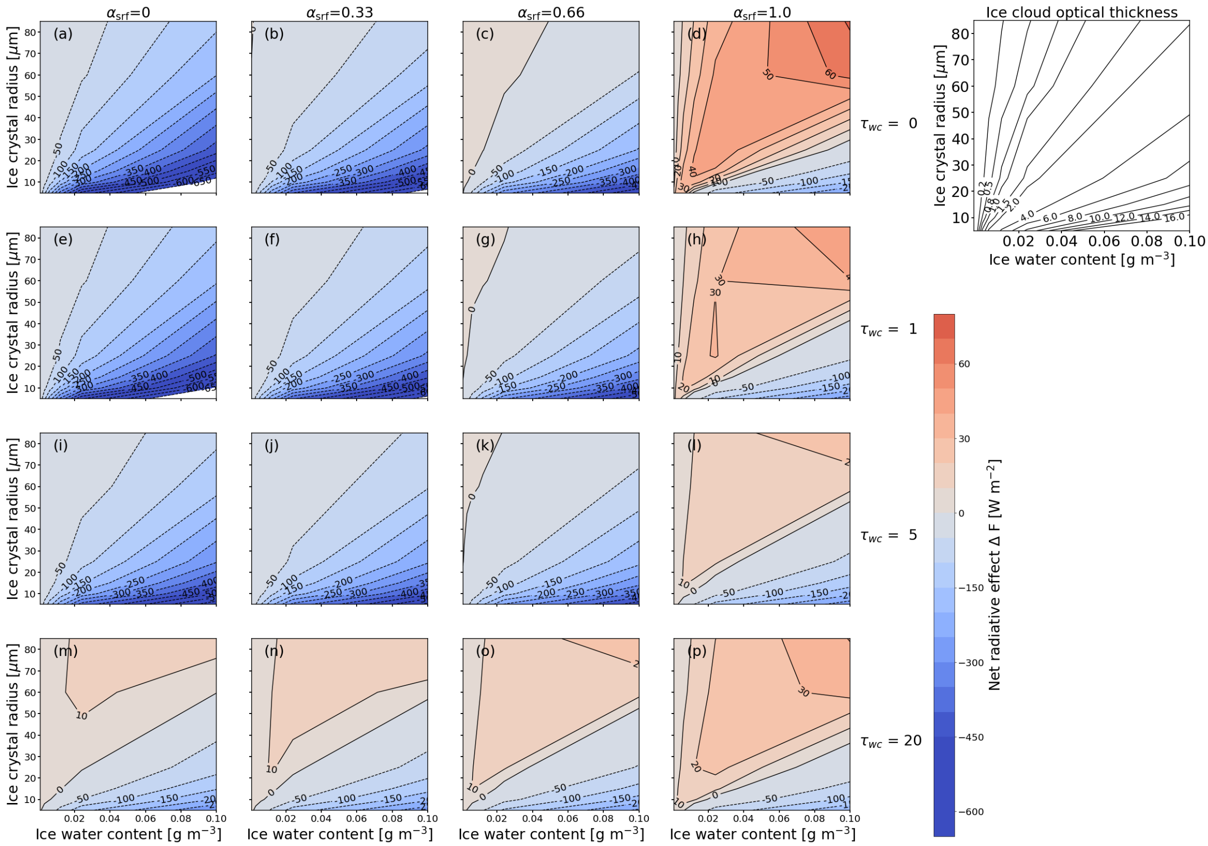

Figure 17. Same as Fig. 11 but for ΔF_{net} (in $\mathrm{W\,m^{-2}}$) and combinations of surface albedo α_{srf} and cloud optical thickness τ_{liq} of the underlying liquid water cloud.

ΔF_{net} ranges between 0 and 20 $\mathrm{W\,m^{-2}}$ and is characterized by a low sensitivity with respect to r_{eff} and IWC of the ice cloud. An exception are clouds with extreme N_{ice}, where an increased cooling effect in relation to r_{eff} occurs.

4 Discussion

For the sake of completeness and to raise awareness of potential uncertainties in the present simulations due to the effects of cloud heterogeneity and three-dimensional (3D) scattering on the estimated RE, we briefly mention the relevant literature. The majority of past cirrus and contrail studies that quantified the RE sensitivity were based on one-dimensional (1D) RT simulations (Strauss et al., 1997; Meerkötter et al., 1999; Fahey et al., 1999; Stuber et al., 2006). While aged and spread contrails might be approximated as thin plane-like layers within a homogeneous atmosphere (Minnis et al., 1999), younger contrails and cirrus are heterogeneous in their horizontal and vertical distribution of ice water content. The first study that investigated 3D-radiative effects was performed by Schulz (1998). This study was followed by Gounou and Hogan (2007) and Forster et al. (2012)

, who used 3D Monte Carlo simulations and found differences in contrail solar RE between 1D and 3D simulations of up to 40 %. These values were found for extreme cases, e.g., large solar zenith angle (Sun close to the horizon). With the Sun illuminating the contrail or cirrus from the side, extinction and absorption within the cloud increases and scattering at cloud sides becomes more important compared to an illumination from above. Enhanced scattering at cloud sides increases the likelihood that photons get scattered back into space instead of being absorbed. Such effects are not captured by 1D RT simulations. However, there is no systematic bias in solar, TIR, and net RE between 1D and 3D simulations and the deviations decrease with increasing cloud homogeneity. More specifically, the differences between 1D and 3D simulations changes in magnitude and sign depending on the cloud heterogeneity and the solar illumination geometry. We employ 1D simulations as the total number of simulations performed within this study and the computational cost for full 3D RT simulation is unpractical. Therefore, we highlight that the provided data set can be used for situations that can be approximated by plane-parallel clouds and solar zenith angles smaller than 70°. Results should be used considering that 3D radiative effects introduce uncertainties.

The parameter selection of this sensitivity study was motivated by Meerkötter et al. (1999), which was supported by previous studies, for example Fu and Liou (1993), Zhang et al. (1999), Yang et al. (2010), or Mitchell et al. (2011). Schumann et al. (2012) then parameterized the effects of the parameters identified by Meerkötter et al. (1999) on the cloud RE. Additional influences like aerosol layers, more complex surface albedo, or multiple overlapping cirrus and contrails have not been investigated here and represent additional degrees of freedom. For example, previous studies found that aerosols have only a minor influence on contrail RE (Meerkötter et al., 1999) and Sanz-Morère et al. (2021) reported that the impact of overlap between contrails on their RE is negligible. Nevertheless, the present study covers the parameters that most directly affect cirrus RE.

This study focused on the cloud RE of homogeneous, horizontally infinite ice cloud layers and neglected horizontal photon transport. The vertical and horizontal structure of ice clouds, i.e., distribution of ice water content, is typically heterogeneous, which is one reason for differences and uncertainties between 1D-simulated and the actual RE of such clouds (Fauchez et al., 2017, 2018) . Additional differences originate from the independent pixel approximation (Cahalan et al., 1994). Only few studies are available on cirrus 3D effects, e.g., Hogan and Kew (2005); Gounou and Hogan (2007).

5 Summary

The net RE of cirrus and contrails depends on multiple factors ~~mainly~~ related to the microphysical and macrophysical cloud properties, the ~~related~~ cloud optical properties, and radiative properties of the environment. The presented study aimed to separate the effect of eight selected parameters: solar zenith angle θ, ice water content IWC, ice crystal effective radius r_{eff}, cirrus temperature $T_{\mathrm{cld,ice}}$, surface albedo α_{srf}, surface temperature T_{srf}, liquid water cloud optical thickness τ_{liq} of an underlying cloud, and three ice crystal shapes on the cirrus RE. In total, ~~94~~283,500 simulations have been performed ~~that were constrained by their values and~~ with the libradtran radiative transfer code by varying the 8 parameters within the ranges that are typically associated with natural cirrus and contrails. Specific cases or sub-samples were selected and discussed, while the entire set of ~~simulations~~ results is made available as a ~~netCDF file that can be explored by the user (Wolf et al., 2023a)~~NetCDF file (Wolf et al., 2023b).

For the presented cases the cirrus RE was separated discussed separately for the solar ΔF_{sol} and TIR ΔF_{tir} part of the spectrum, but also for the combined net RE. Comparing to a chosen reference cloud with $\theta = 0°$, $T_{\mathrm{cld,ice}} = 223$ K $T_{\mathrm{cld,ice}} = 219$ K, $\alpha_{\mathrm{srf}} = 0$, $T_{\mathrm{srf}} = 313$ $T_{\mathrm{srf}} = 300$ K, IWC = 0.024 g m^{-3}, r_{eff} = 45 85 μm, τ_{wc} τ_{liq} = 0 (no liquid water cloud), and resulting τ_{ice} = 0.18 (at 640 0.46 (at 550 nm) it was found that r_{eff} has the largest impact on solar, TIR, and net RE. The second most important parameter is the IWC, which impacts ΔF_{sol} and ΔF_{tir} equally. In the selected case, ΔF_{sol} and ΔF_{tir} have opposite signs, meaning that the IWC has a relatively small impact on ΔF_{net}. It has to be noted that the counter-balancing effect only appears during daytime, when $\Delta F_{\mathrm{sol}} \neq 0$ W m^{-2}. At night, ΔF_{net} equals ΔF_{tir} and the cirrus heats the Earth-atmosphere-system. After r_{eff} and IWC, the solar RE of cirrus is determined by θ, α_{srf}, τ_{liq}, and the ice crystal shape in descending priority. The RE in the TIR spectrum is dominated by T_{srf}, $T_{\mathrm{cld,ice}}$, τ_{liq}, and the ice crystal shape. The combined net RE is controlled by α_{srf}, θ, and T_{srf}, sorted in decreasing importance. The relevance of the input selected parameters can differ for other τ_{ice} and ambient condition.

The impact of individual input parameter on the solar, TIR, and net RE was further investigated and quantified by sub-sampling the entire set for one fixed parameter, while the remaining parameters can were allowed to vary. This can be interpreted as a type of a sub-sampling, by averaging all unfixed values of RE, to project ΔF onto the one-dimensional space.

- For all As expected, variations in θ and have no influence on ΔF_{tir} but only on ΔF_{sol}. The majority of simulated ΔF_{sol} becomes more intense (stronger cooling) with increasing θ and reaches a maximum for θ between 50°–70°. For further increasing θ the cooling effect in the solar declines. The exact location of maximum ΔF_{sol} is primarily dependent on α_{srf}. However, the width and shape of the distributions of ΔF_{sol} become narrower with a tail towards small ΔF_{sol} with reduced cooling. Consequently, the majority of the simulations , with negative ΔF_{sol} is dominated by exceeded by positive ΔF_{tir} and leads to a positive median ΔF_{net} (warming).

- The projection of ΔF_{net} for varying α_{srf} showed that cirrus primarily cools in the solar, except for $\alpha_{\mathrm{srf}} = 1$ α_{srf} approaching 1, e.g., over ice covered regions. Contrarily, ΔF_{tir} is positive and unaffected by the variations in α_{srf}. ΔF_{tir} determines the resulting ΔF_{net}, which leads to a net heating effect, when α_{srf} exceeds the critical range of 0.25–0.3.

- An increase in IWC intensifies the cooling in the solar and the heating in the TIR. As both effects compete against each other and ΔF_{tir} dominates ΔF_{sol}, the resulting net RE is a warming. An exception appears for largest IWC, where median ΔF_{net} is negative. Simultaneously, the increase in IWC causes an enhanced impact of the free parameters and associated uncertainties.

- Clouds with similar IWC but larger r_{eff} are comprised of fewer ice crystals, which reduces the clouds cloud reflectivity. Over the entire range of r_{eff} the sub-sampled data set is characterized by a negative ΔF_{sol} that is most intense for the smallest crystals. Similarly, ΔF_{tir} is largest for small crystals and decreases for large crystals. While the solar and TIR ΔF become less intense with r_{eff}, the decrease is more pronounced for ΔF_{sol} such that cirrus primarily has a positive ΔF_{net}. An exception are clouds with the smallest r_{eff} and high IWC that occur only in contrails over non-reflective surfaces.

– The surface temperature T_{srf} and ice cloud temperature $T_{\mathrm{cld,ice}}$ only affect the TIR component of ΔF. Decreasing T_{srf} or $T_{\mathrm{cld,ice}}$ leads to an intensified TIR and net heating effect. Furthermore, T_{srf} and $T_{\mathrm{cld,ice}}$ can be considered as belonging together in which TIR and net heating becomes larger with increasing difference among T_{srf} and $T_{\mathrm{cld,ice}}$.

– An underlying liquid water cloud with an increasing ~~τ_{wc}~~ τ_{liq} leads to a reduction in solar ΔF_{sol}. Simultaneously, the TIR heating remains almost constant and the resulting ΔF_{net} increases with ~~τ_{wc}~~ τ_{liq}.

~~It has to be noted that this study focused on the cloud RE of homogeneous, infinite ice cloud layers and neglected horizontal photon transport. The vertical and horizontal structure of ice clouds, i.e., distribution of ice water content, is typically heterogeneous, which is one reason for differences and uncertainties between 1D-simulated and the actual RE of such clouds (Fauchez et al., 2017, 2018). Additional differences originate from the IPA (Cahalan et al., 1994). Both effects have been primarily investigated for liquid water clouds, for example by Marshak and Davis (2005), while only few studies are available on cirrus 3D effects, e.g., Hogan and Kew (2005). Therefore, a follow-up study, that aims to determine and separate both effects, is currently ongoing.~~

Data availability. The three data-sets with all simulated irradiances, the calculated cloud radiative effect, and the ice cloud optical thickness are given in separate NetCDF-files. Each file represents an individual ice crystal shape. The data is available on the zenodo platform as Wolf et al. (2023b)

Appendix A: Overview over the multi-parameter dependencies

Figures A1 and A2 show solar ΔF_{sol} and TIR ΔF_{tir} (above diagonal), and net ΔF_{net} (below diagonal) for combinations of parameters indicated along the x- and y-axis. Both plots are intended to provide an overview over the multi-parameter dependencies. Within each sub-panel ΔF is given as a function of the x- and y-axis, while the other parameters are set to constant values that are representative of contrails and cirrus clouds. For example, the 'IWC–SZA' panel shows ΔF as a function of IWC, with $\theta = 30°$, $T_{\mathrm{cld,ice}}$ = ~~233~~ 231 K, ~~$r_{\mathrm{eff}} = 15$~~ $r_{\mathrm{eff}} = 25$ μm, $\alpha = 0.15$, ~~$T_{\mathrm{srf}} = 273$~~ $T_{\mathrm{srf}} = 288$ K, and without a second liquid water cloud (~~$\tau_{\mathrm{wc}} = 0$~~ $\tau_{\mathrm{liq}} = 0$). This can be understood as a 2D–cross-section of the 8D hypercube. The black arrows indicate the gradient of the field. The gradient is computed with second order central differences and one-side differences at the boundaries of the field. The length of the arrow is only representative for an individual field and cannot be compared with the other fields as it depends on the units of the parameters. Therefore, the arrows are normalized and can only be interpreted for their direction and not for their length.

Appendix B: Atmospheric profiles of temperature and relative humidity

The radiative transfer simulations within the present study use the atmospheric profiles from Anderson et al. (1986) that are provided in the libRadtran package. To cover a wide range of temperature conditions, three atmospheric profiles were selected, which represent subarctic, mid-latitude, and tropical conditions given by the `afglsw`, `afglus`, and `afglt` profiles, respectively.

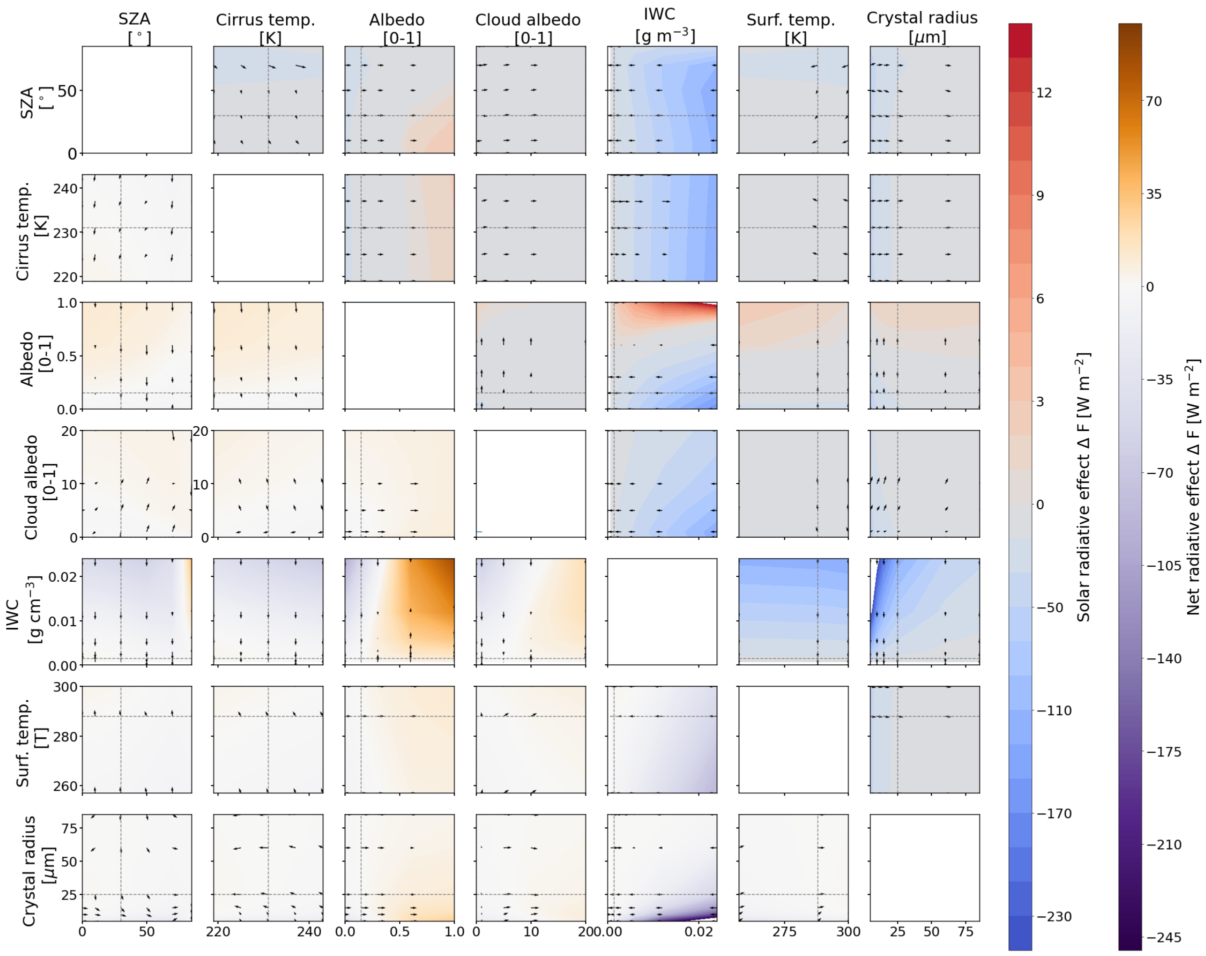

Figure A1. Above diagonal panels: Plot of median solar $\Delta F_{\rm sol}$ projected in two-dimensional parameter space. Blue colors indicate negative $\Delta F_{\rm sol}$ (cooling), while red colors indicate positive $\Delta F_{\rm sol}$ (warming). Below diagonal panels: Same as above diagonal but for median net $\Delta F_{\rm net}$. Purple shades indicate negative $\Delta F_{\rm net}$ (cooling), while orange shades indicate positive $\Delta F_{\rm net}$ (warming). All ΔF are given in $\mathrm{W\,m^{-2}}$. The black arrows point to the direction of the steepest slope.

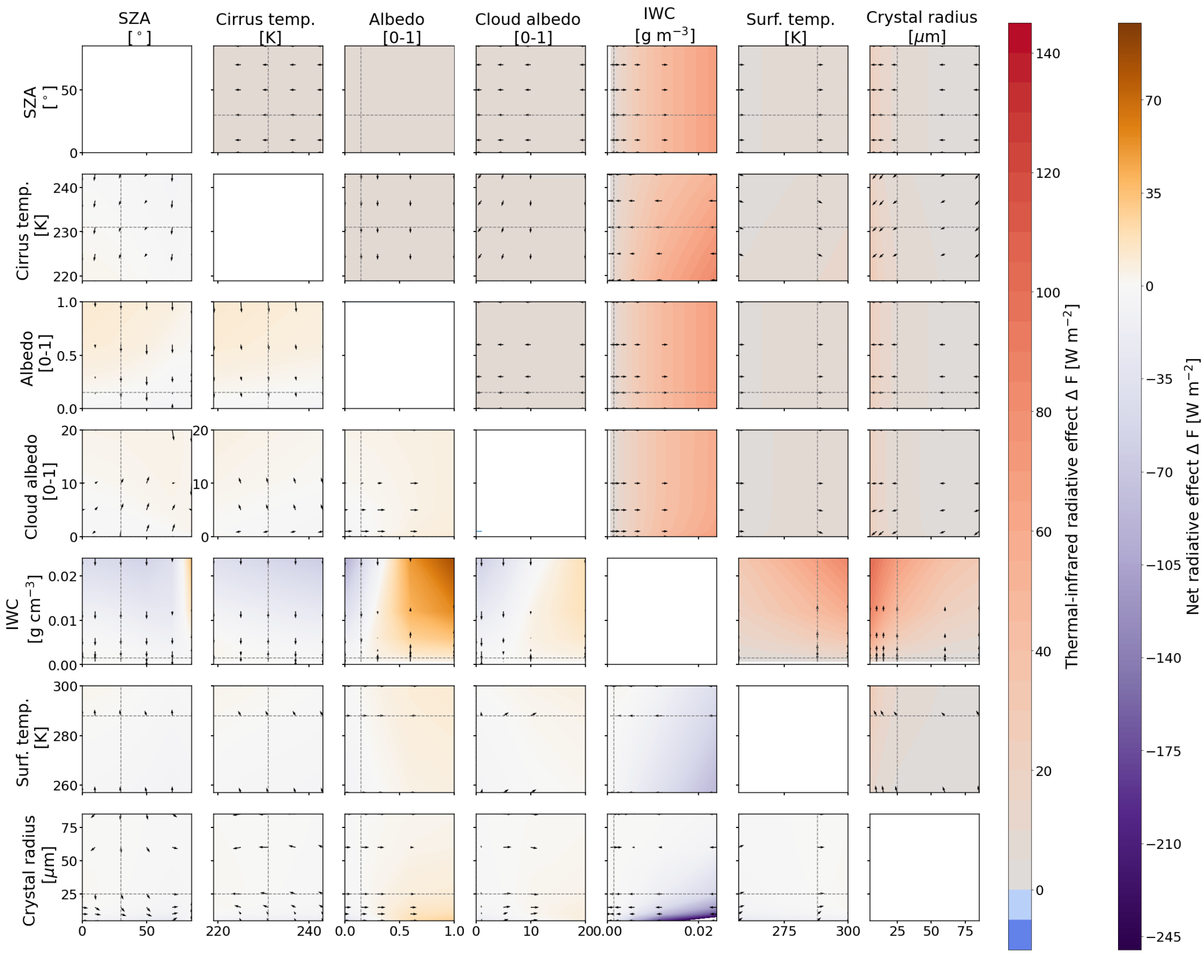

Figure A2. Same as Fig. A1 but above diagonal panels present median TIR ΔF_{tir}. All ΔF are given in W m^{-2}.

The vertical temperature profiles range from 0 to 120 km and are visualized in Fig. B1a. Figure B1b presents a close-up and Fig. B1c shows the relative humidity profile for 0 to 20 km. The position of the low-level liquid water cloud between 1000 and 1500 m is indicated by the gray shaded area. The positions of the ice cloud altitude are indicated by the colored dots.

According to Anderson et al. (1986) the presented profiles are subject to variations between 10 % and 30 %. Therefore, we multiplied the original profiles profiles by factors of 0.8 and 1.2 to: i) partly account for this variation and ii) to estimate the influence of variations in RH on the simulated solar, TIR, and net RE. The modified profiles with $\pm 20\,\%$ are indicated by pale colors in Fig B1c.

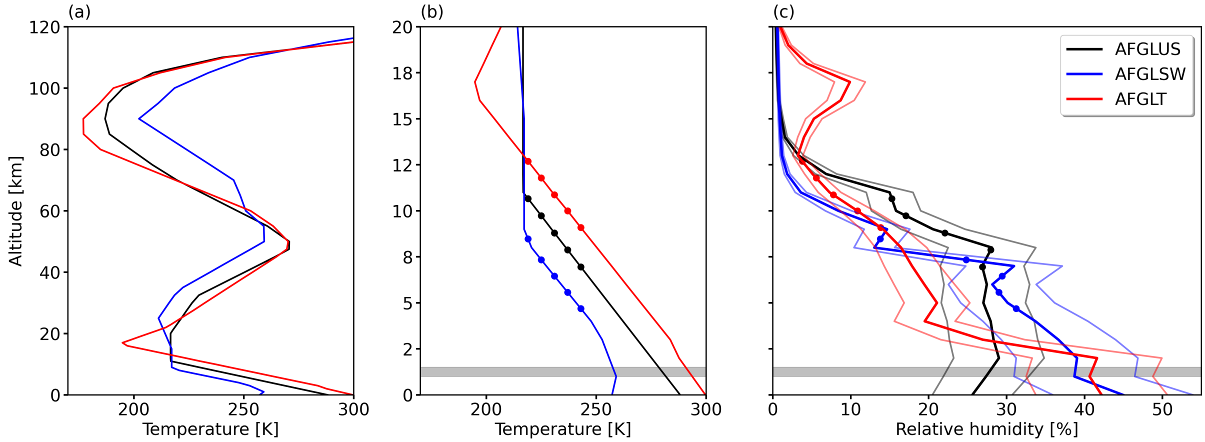

Figure B1. Profiles of temperature (a,b) and relative humidity (c) used for the radiative transfer simulations. The subarctic (`afglsw`), mid-latitude (`afglus`), and tropical (`afglt`) profiles are given in blue, black, and red, respectively. The modified profiles with $\pm 20\,\%$ are indicated by pale colors. The positions of the simulated ice water cloud are indicated by the colored dots for each profile. The position of the low-level liquid water cloud is indicated by the gray shaded area.

Appendix C: Simulation time and accuracy

The radiative transfer solver ~~fdisort2 (Stamnes et al., 2000)~~ DISORT (Buras et al., 2011) allows to select $2N$-number of streams to be used in the radiative transfer simulations. Higher number of streams increases the accuracy of the simulations but also the computational time. To obtain sufficient accuracy while keeping the computational time reasonable, the optimal trade-off was estimated by progressively increasing the number of streams from 4 to 48. The simulation with 48 streams is regarded here as the reference with the highest accuracy and computational time.

The number of streams and the timing of the RT simulations ~~is estimated on~~ are estimated on the basis of a specific parameter combination, representing a complex cloud scene that is characterized by cloud–cloud–surface-interactions. The simulations are run for a solar zenith angle $\theta = 70°$, a cirrus temperature $T_{\mathrm{cld,ice}}$ of 233 K, a surface albedo $\alpha_{\mathrm{srf}} = 1$, an ice water content ~~$IWC = 2.4 \cdot 10^{-3}\,\mathrm{g\,m^{-3}}$~~ IWC = 0.0024 $\mathrm{g\,m^{-3}}$, a surface temperature $T_{\mathrm{srf}} = 270$ K, an ice crystal effective radius $r_{\mathrm{eff}} = 5\,\mu\mathrm{m}$, and an additionally underlying liquid water cloud (cloud optical thickness τ_{liq} = 10).

The computational time that is required for the simulations depends on the available hardware. Therefore, we provide the fraction of ~~time that is required and relate it to the maximum duration using~~ the computational time required for n streams to a simulation with 48 streams. The accuracy is given as the relative difference between the cloud RE for a given number of streams with respect to the reference simulation.

Figure C1 shows that the relative difference in the RE decreases with increasing number of streams (higher accuracy). A significant gain in accuracy is achieved by switching from 4 to 10 streams. For simulations with 12 to 16 streams the relative difference remains constant at around 0.1 %. Further increasing to 24 streams provides only a slight gain in accuracy, whereas

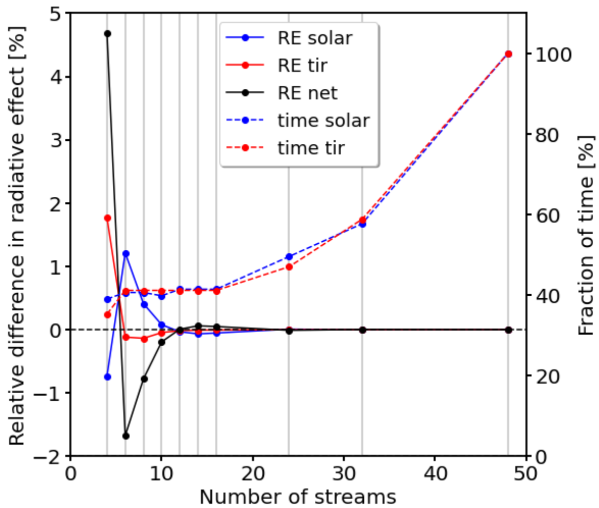

Figure C1. Relative deviation (in %) of solar (solid blue), TIR (solid red), and net (solid black) cloud radiative effect from the reference simulation calculated with 48 streams. The computational time is given as ~~the~~ a fraction of the ~~maximum duration~~ computational time needed for the solar (~~blue,~~ dashed blue) or TIR (~~red,~~ dashed red) simulations using the maximum number of 48 streams.

~~the~~ computational time increases disproportionaly. Therefore, the ~~simulations in this study were run with 16 streams as it provides the~~ optimal trade-off between accuracy and computational time is obtained with 16 streams, which is the configuration used in this study.

Appendix D: Single-scattering phase function $\mathcal{P}$

~~The selected ice crystal shape is an important factor in RT simulations. Kahnert et al. (2008) found that the shape-effect on the cloud RE is up to 20 $\mathrm{W\,m^{-2}}$, which is, in their study, equivalent to a change in surface albedo α_{srf} from 0.4 to 0.8 or altering the ice water content IWC of the cloud by a factor of 2.~~ The shape-effect is primarily caused by differences in the extinction of radiation and the asymmetry parameter~~, which itself depends on the scattering~~. The asymmetry parameter is a measure of the asymmetry of the phase function $\mathcal{P}$ ~~(Kahnert et al., 2008)~~between forward and backward scattering (Macke et al., 1998; Fu, 2007). $\mathcal{P}$ provides the angular distribution of the scattered direction in relation to the incident light. As an example, Fig. D1a–d shows $\mathcal{P}$ at 550 nm wavelength for columns, plates, droxtals, and a mixture of aggregated crystals (hollow column; bullets; rosettes), respectively. The phase functions are extracted from the post-processed libRadtran data set that is based on the ice optics computations from Yang et al. (2000).

All ice crystal shapes are characterized by a dominating peak in the forward direction, which drops by a factor of 10^4 sr^{-1}, when the scattering angle Θ increases from 0° to 10°. For $10° < \Theta < 160°$, $\mathcal{P}$ ~~remains mostly flat with values~~ varies between 10^{-1} sr^{-1} and 10^1 sr^{-1}. Towards $\Theta > 160°$ the phase function increases, showing enhanced backward scattering except for the complex shaped crystals (Fig. D1d). Further characteristics of $\mathcal{P}$ are local maxima at 22° and 46° scattering angles that appear

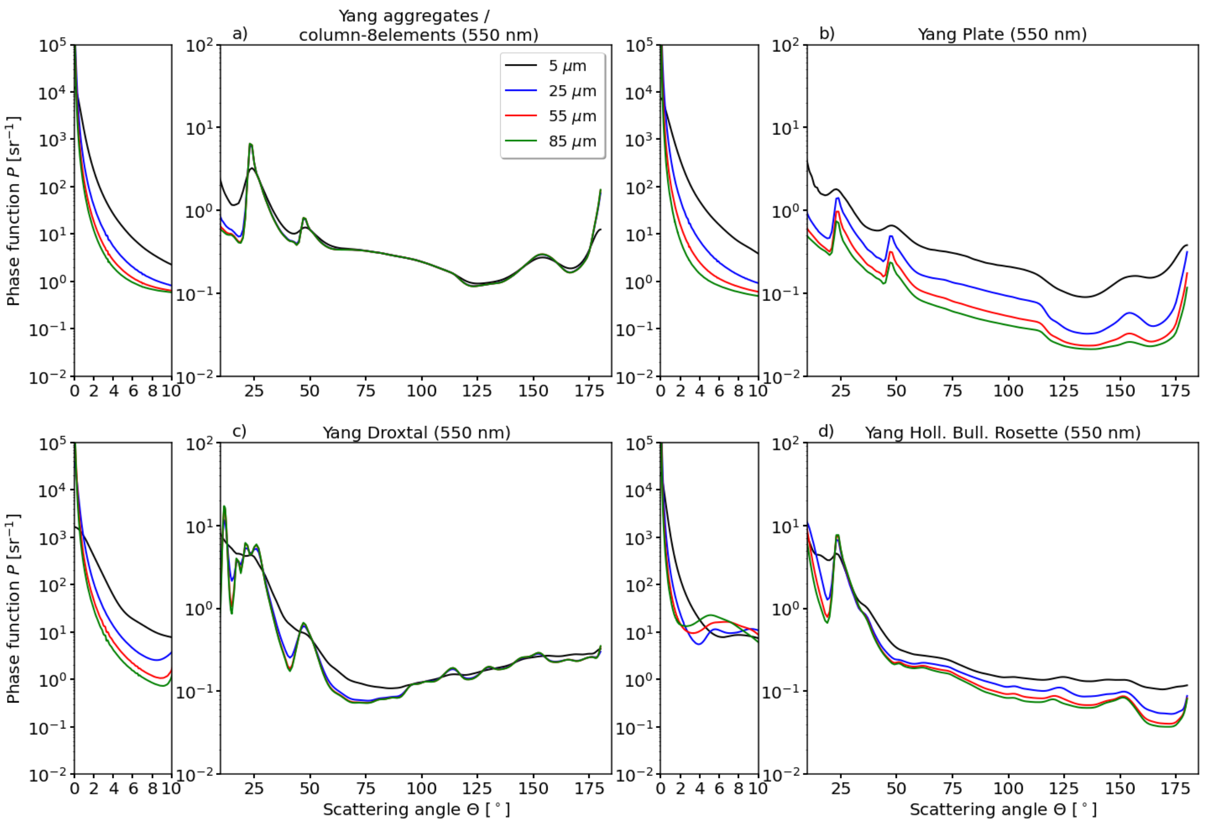

Figure D1. Phase function of four different ice crystal ~~habits~~ shapes and ~~three~~ four particle size distributions at 550 nm wavelength. Plot of the (1,1)-element of the scattering phase matrix. ~~Two~~ Please note the two different y-scales ~~are applied depending on~~ to account for the ~~size of~~ different magnitudes in the forward scattering peak. Plotted $\mathcal{P}$ are post-processed phase functions from Emde et al. (2016) that are based on ~~Yang et al. (2000)~~Yang et al. (2013). The phase functions from Emde et al. (2016) assume a crystal size distribution that follows a gamma function.

for columns, plates, and droxtals (Fig. D1a–c), and cause halo phenomena. For the crystal mixture and aggregated crystals (Fig. D1d) the second peak is barely noticeable as the surface roughness and shape complexity smooths angular-dependent scattering in $\mathcal{P}$. Additionally, non-spherical crystals (Fig. D1a,b,d) have enhanced sideward scattering compared to ice crystals with a roughly spherical shape, like droxtals (Fig. D1c) or water droplets. Another characteristic is the shift in the $\mathcal{P}$ from variations in the crystal radius r_{eff}, which is most prominent for plates and lowest for columns.

Author contributions. **KW** designed the model setup, conducted the experiments and the data analysis, and prepared the manuscript. **NB** and **OB** contributed equally to the analysis and the preparation of the manuscript.

Competing interests. The authors declare no competing interest.

Acknowledgements. The authors acknowledge support from the Direction Générale de l'Aviation Civile through the Convention N°2021-39 relative to "Aviation & Climate".

References

Anderson, G. P., Clough, S. A., Kneizys, F. X., Chetwynd, J. H., and Shettle, E. P.: AFGL atmospheric constituent profiles, Environ. Res. Pap, 954, 1–46, 1986.

Baldridge, A. M., Hook, S. J., Grove, C. I., and Rivera, G.: The ASTER spectral library version 2.0, Remote Sens. Environ., 113, 711–715, https://doi.org/10.1016/j.rse.2008.11.007, 2009.

Bauer, P., Thorpe, A., and Brunet, G.: The quiet revolution of numerical weather prediction., Nature, 525, 47–55, https://doi.org/10.1038/nature14956, 2015.

Baum, B. A., Heymsfield, A. J., Yang, P., and Bedka, S. T.: Bulk scattering properties for the remote sensing of ice clouds. Part I: microphysical data and models, J. Appl. Meteorol., 44, 1885–1895, https://doi.org/10.1175/JAM2308.1, 2005a.

Baum, B. A., Yang, P., Heymsfield, A. J., Platnick, S., King, M. D., Hu, Y.-X., and Bedka, S. T.: Bulk scattering properties for the remote sensing of ice clouds. Part II: narrowband models, J. Appl. Meteorol., 44, 1896–1911, https://doi.org/10.1175/JAM2309.1, 2005b.

Baum, B. A., Yang, P., Nasiri, S., Heidinger, A. K., Heymsfield, A., and Li, J.: Bulk scattering properties for the remote sensing of ice clouds. Part III: high-resolution spectral models from 100 to 3250 cm-1, J. Appl. Meteorol., 46, 423–434, https://doi.org/10.1175/JAM2473.1, 2007.

Bi, L., Yang, P., Liu, C., Yi, B., Baum, B. A., van Diedenhoven, B., and Iwabuchi, H.: Assessment of the accuracy of the conventional ray-tracing technique: Implications in remote sensing and radiative transfer involving ice clouds, J. Quant. Spectrosc. Radiat. Transfer, 146, 158–174, https://doi.org/10.1016/j.jqsrt.2014.03.017, 2014.

Bickel, M., Ponater, M., Bock, L., Burkhardt, U., and Reineke, S.: Estimating the effective radiative forcing of contrail cirrus, J. Climate, 33, 1991–2005, https://doi.org/10.1175/JCLI-D-19-0467.1, 2020.

Bräuer, T., Voigt, C., Sauer, D., Kaufmann, S., Hahn, V., Scheibe, M., Schlager, H., Diskin, G. S., Nowak, J. B., DiGangi, J. P., Huber, F., Moore, R. H., and Anderson, B. E.: Airborne measurements of contrail ice properties–dependence on temperature and humidity, Geophys. Res. Lett., 48, e2020GL092 166, https://doi.org/10.1029/2020GL092166, 2021.

Buras, R., Dowling, T., and Emde, C.: New secondary-scattering correction in DISORT with increased efficiency for forward scattering, J. Quant. Spectrosc. Radiat. Transfer, 112, 2028–2034, https://doi.org/10.1016/j.jqsrt.2011.03.019, 2011.

Burkhardt, U. and Kärcher, B.: Global radiative forcing from contrail cirrus, Nat. Clim. Change, 1, 54–58, https://doi.org/10.1038/nclimate1068, 2011.

Cahalan, R. F., Ridgway, W., Wiscombe, W. J., Bell, T. L., and Snider, J. B.: The albedo of fractal stratocumulus clouds, J. Atmos. Sci., 51, 2434–2455, https://doi.org/10.1175/1520-0469(1994)051<2434:TAOFSC>2.0.CO;2, 1994.

Campbell, J. R., Lolli, S., Lewis, J. R., Gu, Y., and Welton, E. J.: Daytime cirrus cloud top-of-the-atmosphere radiative forcing properties at a midlatitude site and their global consequences, J. Appl. Meteorology and Climatology, 55, 1667–1679, https://doi.org/10.1175/JAMC-D-15-0217.1, 2016.

Chen, T., Rossow, W. B., and Zhang, Y.: Radiative effects of cloud-type variations, J. Climate, 13, 264–286, https://doi.org/10.1175/1520-0442(2000)013<0264:REOCTV>2.0.CO;2, 2000.

Coakley, J. A. and Chylek, P.: The two-stream approximation in radiative rransfer: including the angle of the incident radiation, J. Atmos. Sci., 32, 409–418, https://doi.org/10.1175/1520-0469(1975)032<0409:TTSAIR>2.0.CO;2, 1975.

Corti, T. and Peter, T.: A simple model for cloud radiative forcing, Atmos. Chem. Phys., 9, 5751–5758, https://doi.org/10.5194/acp-9-5751-2009, 2009.

Deirmendjian, D.: Scattering and polarization properties of polydispersed suspensions with partial absorption, Tech. rep., RAND CORP SANTA MONICA CA, 1962.

Emde, C., Buras-Schnell, R., Kylling, A., Mayer, B., Gasteiger, J., Hamann, U., Kylling, J., Richter, B., Pause, C., Dowling, T., and Bugliaro, L.: The libRadtran software package for radiative transfer calculations (version 2.0.1), Geosci. Model Dev., 9, 1647–1672, https://doi.org/10.5194/gmd-9-1647-2016, 2016.

Evans, K. F.: The spherical harmonics discrete ordinate method for three-dimensional atmospheric radiative transfer, J. Atmos. Sci., 55, 429–446, https://doi.org/10.1175/1520-0469(1998)055<0429:TSHDOM>2.0.CO;2, 1998.

Fahey, D. W., Schumann, U., Ackerman, S., Artaxo, P., Boucher, O., Danilin, M. Y., Kärcher, B., Minnis, P., Nakajima, T., and Toon, O. B.: Aviation-produced aerosols and cloudiness. IPCC special report., pp. 65–120, 1999.

Fauchez, T., Platnick, S., Meyer, K., Cornet, C., Szczap, F., and Várnai, T.: Scale dependence of cirrus horizontal heterogeneity effects on TOA measurements – Part I: MODIS brightness temperatures in the thermal infrared, Atmos. Chem. Phys., 17, 8489–8508, https://doi.org/10.5194/acp-17-8489-2017, 2017.

Fauchez, T., Platnick, S., Várnai, T., Meyer, K., Cornet, C., and Szczap, F.: Scale dependence of cirrus heterogeneity effects. Part II: MODIS NIR and SWIR channels, Atmos. Chem. Phys., 18, 12 105–12 121, https://doi.org/10.5194/acp-18-12105-2018, 2018.

Forster, L. and Mayer, B.: Ice crystal characterization in cirrus clouds III: retrieval of ice crystal shape and roughness from observations of halo displays, Atmos. Chem. Phys., 22, 15 179–15 205, https://doi.org/10.5194/acp-22-15179-2022, 2022.

Forster, L., Emde, C., Mayer, B., and Unterstrasser, S.: Effects of three-dimensional photon transport on the radiative forcing of realistic contrails, J. Atmos. Sci., 69, 2243–2255, https://doi.org/10.1175/JAS-D-11-0206.1, 2012.

Forster, L., Seefeldner, M., Wiegner, M., and Mayer, B.: Ice crystal characterization in cirrus clouds: a sun-tracking camera system and automated detection algorithm for halo displays, Atmos. Meas. Tech., 10, 2499–2516, https://doi.org/10.5194/amt-10-2499-2017, 2017.

Freudenthaler, V., Homburg, F., and Jäger, H.: Contrail observations by ground-based scanning lidar: Cross-sectional growth, Geophys. Res. Lett., 22, 3501–3504, https://doi.org/10.1029/95GL03549, 1995.

Freudenthaler, V., Homburg, F., and Jäger, H.: Optical parameters of contrails from lidar measurements: Linear depolarization, Geophys. Res. Lett., 23, 3715–3718, https://doi.org/10.1029/96GL03646, 1996.

Fu, Q.: An accurate parameterization of the solar radiative properties of cirrus clouds for climate models, J. Climate, 9, 2058–2082, https://doi.org/10.1175/1520-0442(1998)011<2223:AAPOTI>2.0.CO;2, 1996.

Fu, Q.: A new parameterization of an asymmetry factor of cirrus clouds for climate models, J. Atmos. Sci., 64, 4140–4150, https://doi.org/10.1175/2007JAS2289.1, 2007.

Fu, Q. and Liou, K. N.: On the correlated k-distribution method for radiative transfer in nonhomogeneous atmospheres, J. Atmos. Sci., 49, 2139–2156, https://doi.org/10.1175/1520-0469(1992)049<2139:OTCDMF>2.0.CO;2, 1992.

Fu, Q. and Liou, K. N.: Parameterization of the radiative properties of cirrus clouds, J. Atmos. Sci., 50, 2008–2025, https://doi.org/10.1175/1520-0469(1993)050<2008:POTRPO>2.0.CO;2, 1993.

Gardner, A. S. and Sharp, M. J.: A review of snow and ice albedo and the development of a new physically based broadband albedo parameterization, J. Geophys. Res. Earth Surf., 115, F01 009, https://doi.org/10.1029/2009JF001444, 2010.

Gasteiger, J., Emde, C., Mayer, B., Buras, R., Buehler, S., and Lemke, O.: Representative wavelengths absorption parameterization applied to satellite channels and spectral bands, J. Quant. Spectrosc. Radiat. Transfer, 148, 99–115, https://doi.org/10.1016/j.jqsrt.2014.06.024, 2014.

Gayet, J.-F., Shcherbakov, V., Voigt, C., Schumann, U., Schäuble, D., Jessberger, P., Petzold, A., Minikin, A., Schlager, H., Dubovik, O., and Lapyonok, T.: The evolution of microphysical and optical properties of an A380 contrail in the vortex phase, Atmos. Chem. Phys., 12, 6629–6643, https://doi.org/10.5194/acp-12-6629-2012, 2012.

Goodman, J., Pueschel, R. F., Jensen, E. J., Verma, S., Ferry, G. V., Howard, S. D., Kinne, S. A., and Baumgardner, D.: Shape and size of contrails ice particles, Geophys. Res. Lett., 25, 1327–1330, https://doi.org/10.1029/97GL03091, 1998.

Gounou, A. and Hogan, R. J.: A sensitivity study of the effect of horizontal photon transport on the radiative forcing of contrails, J. Atmos. Sci., 64, 1706–1716, https://doi.org/10.1175/JAS3915.1, 2007.

Gueymard, C. A., Lara-Fanego, V., Sengupta, M., and Xie, Y.: Surface albedo and reflectance: Review of definitions, angular and spectral effects, and intercomparison of major data sources in support of advanced solar irradiance modeling over the Americas, Sol. Energy, 182, 194–212, https://doi.org/10.1016/j.solener.2019.02.040, 2019.

Hansen, J. E. and Travis, L. D.: Light scattering in planetary atmospheres, Space Sci. Rev., 16, 527—-610, https://doi.org/10.1007/BF00168069, 1974.

Haywood, J. M. and Shine, K. P.: Multi-spectral calculations of the direct radiative forcing of tropospheric sulphate and soot aerosols using a column model, Q. J. Royal Meteorol. Soc., 123, 1907–1930, https://doi.org/10.1002/qj.49712354307, 1997.

Haywood, J. M., Allan, R. P., Bornemann, J., Forster, P. M., Francis, P. N., Milton, S., Rädel, G., Rap, A., Shine, K. P., and Thorpe, R.: A case study of the radiative forcing of persistent contrails evolving into contrail-induced cirrus, J. Geophys. Res. Atmos., 114, D24 201, https://doi.org/10.1029/2009JD012650, 2009.

Heymsfield, A. J., Bansemer, A., Field, P. R., Durden, S. L., Stith, J. L., Dye, J. E., Hall, W., and Grainger, C. A.: Observations and parameterizations of particle size distributions in deep tropical cirrus and stratiform precipitating clouds: results from in situ observations in TRMM field campaigns, J. Atmos. Sci., 59, 3457–3491, https://doi.org/10.1175/1520-0469(2002)059<3457:OAPOPS>2.0.CO;2, 2002.

Hogan, R. J. and Kew, S. F.: A 3D stochastic cloud model for investigating the radiative properties of inhomogeneous cirrus clouds, Quarterly Journal of the Royal Meteorological Society, 131, 2585–2608, https://doi.org/10.1256/qj.04.144, 2005.

Hogan, R. J., Behera, M. D., O'Connor, E. J., and Illingworth, A. J.: Estimate of the global distribution of stratiform supercooled liquid water clouds using the LITE lidar, Geophys. Res. Lett., 31, https://doi.org/10.1029/2003GL018977, 2004.

Holz, R. E., Platnick, S., Meyer, K., Vaughan, M., Heidinger, A., Yang, P., Wind, G., Dutcher, S., Ackerman, S., Amarasinghe, N., Nagle, F., and Wang, C.: Resolving ice cloud optical thickness biases between CALIOP and MODIS using infrared retrievals, Atmos. Chem. Phys., 16, 5075–5090, https://doi.org/10.5194/acp-16-5075-2016, 2016.

Horváth, A. and Davies, R.: Comparison of microwave and optical cloud water path estimates from TMI, MODIS, and MISR, J. Geophys. Res. Atmos., 112, D01 202, https://doi.org/10.1029/2006JD007101, 2007.

Hu, Y., Rodier, S., Xu, K., Sun, W., Huang, J., Lin, B., Zhai, P., and Josset, D.: Occurrence, liquid water content, and fraction of supercooled water clouds from combined CALIOP/IIR/MODIS measurements, J. Geophys. Res. Atmos., 115, https://doi.org/10.1029/2009JD012384, 2010.

Iwabuchi, H., Yang, P., Liou, K. N., and Minnis, P.: Physical and optical properties of persistent contrails: Climatology and interpretation, J. Geophys. Res. Atmos., 117, D06 215, https://doi.org/10.1029/2011JD017020, 2012.

Järvinen, E., Jourdan, O., Neubauer, D., Yao, B., Liu, C., Andreae, M. O., Lohmann, U., Wendisch, M., McFarquhar, G. M., Leisner, T., and Schnaiter, M.: Additional global climate cooling by clouds due to ice crystal complexity, Atmos. Chem. Phys., 18, 15 767–15 781, https://doi.org/10.5194/acp-18-15767-2018, 2018.

Jensen, E. J., Kinne, S., and Toon, O. B.: Tropical cirrus cloud radiative forcing: Sensitivity studies, Geophys. Res. Let., 21, 2023–2026, https://doi.org/10.1029/94GL01358, 1994.

Jeßberger, P., Voigt, C., Schumann, U., Sölch, I., Schlager, H., Kaufmann, S., Petzold, A., Schäuble, D., and Gayet, J.-F.: Aircraft type influence on contrail properties, Atmos. Chem. Phys., 13, 11 965–11 984, https://doi.org/10.5194/acp-13-11965-2013, 2013.

Kahnert, M., Sandvik, A. D., Biryulina, M., Stamnes, J. J., and Stamnes, K.: Impact of ice particle shape on short-wave radiative forcing: A case study for an arctic ice cloud, J. Quant. Spectrosc. Radiat. Transfer, 109, 1196–1218, https://doi.org/10.1016/j.jqsrt.2007.10.016, 2008.

Kärcher, B.: Formation and radiative forcing of contrail cirrus, Nat. Commun., 7, https://doi.org/10.1038/s41467-018-04068-0, 2018.

Key, J. R., Yang, P., Baum, B. A., and Nasiri, S. L.: Parameterization of shortwave ice cloud optical properties for various particle habits, J. Geophys. Res. Atmos., 107, AAC 7–1–AAC 7–10, https://doi.org/https://doi.org/10.1029/2001JD000742, 2002.

Krämer, M., Rolf, C., Luebke, A., Afchine, A., Spelten, N., Costa, A., Meyer, J., Zöger, M., Smith, J., Herman, R. L., Buchholz, B., Ebert, V., Baumgardner, D., Borrmann, S., Klingebiel, M., and Avallone, L.: A microphysics guide to cirrus clouds – Part 1: Cirrus types, Atmos. Chem. Phys., 16, 3463–3483, https://doi.org/10.5194/acp-16-3463-2016, 2016.

Krämer, M., Rolf, C., Spelten, N., Afchine, A., Fahey, D., Jensen, E., Khaykin, S., Kuhn, T., Lawson, P., Lykov, A., Pan, L. L., Riese, M., Rollins, A., Stroh, F., Thornberry, T., Wolf, V., Woods, S., Spichtinger, P., Quaas, J., and Sourdeval, O.: A microphysics guide to cirrus – Part 2: Climatologies of clouds and humidity from observations, Atmos. Chem. Phys., 20, 12 569–12 608, https://doi.org/10.5194/acp-20-12569-2020, 2020.

Kurucz, R. L.: Synthetic infrared spectra, Infrared solar physics: proceedings of the 154th Symposium of the International Astronomical Union, 1992.

Lawson, R. P., Heymsfield, A. J., Aulenbach, S. M., and Jensen, T. L.: Shapes, sizes and light scattering properties of ice crystals in cirrus and a persistent contrail during SUCCESS, Geophys. Res. Lett., 25, 1331–1334, https://doi.org/10.1029/98GL00241, 1998.

Lee, D. S., Fahey, D. W., Skowron, A., Allen, M. R., Burkhardt, U., Chen, Q., Doherty, S. J., Freeman, S., Forster, P. M., Fuglestvedt, J., Gettelman, A., De León, R. R., Lim, L. L., Lund, M. T., Millar, R. J., Owen, B., Penner, J. E., Pitari, G., Prather, M. J., Sausen, R., and Wilcox, L. J.: The contribution of global aviation to anthropogenic climate forcing for 2000 to 2018, Atmos. Environ., 244, 117 834, https://doi.org/10.1016/j.atmosenv.2020.117834, 2021.

Liou, K.-N.: Influence of cirrus clouds on weather and climate processes: A global perspective, Mon. Weather Rev., 114, 1167–1199, https://doi.org/10.1175/1520-0493(1986)114<1167:IOCCOW>2.0.CO;2, 1986.

Liou, K. N.: Radiation and cloud processes in the atmosphere. Theory, observation, and modeling, Oxford University Press, 1992.

Liu, C., Yang, P., Minnis, P., Loeb, N., Kato, S., Heymsfield, A., and Schmitt, C.: A two-habit model for the microphysical and optical properties of ice clouds, Atmos. Chem. Phys., 14, 13 719–13 737, https://doi.org/10.5194/acp-14-13719-2014, 2014.

Lohmann, U. and Roeckner, E.: Influence of cirrus cloud radiative forcing on climate and climate sensitivity in a general circulation model, J. Geophys. Res. Atmos., 100, 16 305–16 323, https://doi.org/https://doi.org/10.1029/95JD01383, 1995.

Luebke, A. E., Afchine, A., Costa, A., Grooß, J.-U., Meyer, J., Rolf, C., Spelten, N., Avallone, L. M., Baumgardner, D., and Krämer, M.: The origin of midlatitude ice clouds and the resulting influence on their microphysical properties, Atmos. Chem. Phys., 16, 5793–5809, https://doi.org/10.5194/acp-16-5793-2016, 2016.

Luebke, A. E., Ehrlich, A., Schäfer, M., Wolf, K., and Wendisch, M.: An assessment of macrophysical and microphysical cloud properties driving radiative forcing of shallow trade-wind clouds, Atmos. Chem. Phys., 22, 2727–2744, https://doi.org/10.5194/acp-22-2727-2022, 2022.

Lynch, D. K., Sassen, K., Starr, D. O., and Stephens, G.: Cirrus, chap. 2, Oxford University Press, 1 edn., 2002.

Macke, A. and Großklaus, M.: Light scattering by nonspherical raindrops: Implications for lidar remote sensing of rainrates, J. Quant. Spectrosc. Radiat. Transfer, 60, 355–363, https://doi.org/10.1016/S0022-4073(98)00011-9, 1998.

Macke, A., Mishchenko, M. I., and Cairns, B.: The influence of inclusions on light scattering by large ice particles, J. Geophys. Res. Atmos., 101, 23 311–23 316, https://doi.org/10.1029/96JD02364, 1996a.

Macke, A., Mueller, J., and Raschke, E.: Single scattering properties of atmospheric ice crystals, J. Atmos. Sci., 53, 2813–2825, https://doi.org/10.1175/1520-0469(1996)053<2813:SSPOAI>2.0.CO;2, 1996b.

Macke, A., Francis, P. N., McFarquhar, G. M., and Kinne, S.: The role of ice particle shapes and size distributions in the single scattering properties of cirrus clouds, J. Atmos. Sci., 55, 2874–2883, https://doi.org/10.1175/1520-0469(1998)055<2874:TROIPS>2.0.CO;2, 1998.

Markowicz, K. M. and Witek, M. L.: Simulations of contrail optical properties and radiative forcing for various cystal shapes, J. Appl. Meteor. Climatol., 50, 1740–1755, https://doi.org/10.1175/2011JAMC2618.1, 2011.

Marshak, A. and Davis, A., eds.: 3D radiative transfer in cloudy atmospheres, Springer Berlin, Heidelberg, first 1 edn., https://doi.org/10.1007/3-540-28519-9, 2005.

McFarquhar, G. M., Zhang, G., Poellot, M. R., Kok, G. L., McCoy, R., Tooman, T., Fridlind, A., and Heymsfield, A. J.: Ice properties of single-layer stratocumulus during the mixed-phase Arctic cloud experiment: 1. Observations, J. Geophys. Res. Atmos., 112, D24 201, https://doi.org/10.1029/2007JD008633, 2007.

Medeiros, B., Nuijens, L., Antoniazzi, C., and Stevens, B.: Low-latitude boundary layer clouds as seen by CALIPSO, J. Geophys. Res. Atmos., 115, D23 207, https://doi.org/10.1029/2010JD014437, 2010.

Meerdink, S. K., Hook, S. J., Roberts, D. A., and Abbott, E. A.: The ECOSTRESS spectral library version 1.0, Remote Sens. Environ., 230, 111 196, https://doi.org/10.1016/j.rse.2019.05.015, 2019.

Meerkötter, R., Schumann, U., Doelling, D. R., Minnis, P., Nakajima, T., and Tsushima, Y.: Radiative forcing by contrails, Ann. Geophys., 17, 1080–1094, https://doi.org/10.1007/s00585-999-1080-7, 1999.

Mie, G.: Beiträge zur Optik trüber Medien, speziell kolloidaler Metallösungen, Ann. Phys., 330, 377–445, https://doi.org/10.1002/andp.19083300302, 1908.

Minnis, P., Schumann, U., Doelling, D. R., Gierens, K. M., and Fahey, D. W.: Global distribution of contrail radiative forcing, Geophys. Res. Lett., 26, 1853–1856, https://doi.org/10.1029/1999GL900358, 1999.

Mishchenko, M. I.: Comprehensive thematic T-matrix reference database: a 2017–2019 update, J. Quant. Spectrosc. Radiat. Transfer, 242, 106 692, https://doi.org/10.1016/j.jqsrt.2019.106692, 2020.

Mitchell, D., Huggins, A., and Grubisic, V.: A new snow growth model with application to radar precipitation estimates, Atmos. Res., 82, 2–18, https://doi.org/10.1016/j.atmosres.2005.12.004, 14th International Conference on Clouds and Precipitation, 2006.

Mitchell, D. L.: Use of mass- and area-dimensional power laws for determining precipitation particle terminal velocities, J. Atmos. Sci., 53, 1710–1723, https://doi.org/10.1175/1520-0469(1996)053<1710:UOMAAD>2.0.CO;2, 1996.

Mitchell, D. L.: Effective diameter in radiation transfer: general definition, applications, and limitations, J. Atmos. Sci., 59, 2330–2346, https://doi.org/10.1175/1520-0469(2002)059<2330:EDIRTG>2.0.CO;2, 2002.

Mitchell, D. L., Liu, Y., and Macke, A.: Modeling cirrus clouds. Part II: Treatment of radiative properties, J. Atmos. Sci., 53, 2967–2988, https://doi.org/10.1175/1520-0469(1996)053<2967:MCCPIT>2.0.CO;2, 1996.

Mitchell, D. L., Lawson, R. P., and Baker, B.: Understanding effective diameter and its application to terrestrial radiation in ice clouds, Atmos. Chem. Phys., 11, 3417–3429, https://doi.org/10.5194/acp-11-3417-2011, 2011.

Muhlbauer, A., McCoy, I. L., and Wood, R.: Climatology of stratocumulus cloud morphologies: microphysical properties and radiative effects, Atmos. Chem. Phys., 14, 6695–6716, https://doi.org/10.5194/acp-14-6695-2014, 2014.

Myhre, G. and Stordal, F.: On the tradeoff of the solar and thermal infrared radiative impact of contrails, Geophys. Res. Let., 28, 3119–3122, https://doi.org/10.1029/2001GL013193, 2001.

Nazaryan, H., McCormick, M. P., and Menzel, W. P.: Global characterization of cirrus clouds using CALIPSO data, J. Geophys. Res. Atmos., 113, D16 211, https://doi.org/10.1029/2007JD009481, 2008.

Noël, V. and Haeffelin, M.: Midlatitude cirrus clouds and multiple tropopauses from a 2002–2006 climatology over the SIRTA observatory, J. Geophys. Res. Atmos., 112, https://doi.org/10.1029/2006JD007753, 2007.

Petty, G. W. and Huang, W.: The modified gamma size distribution applied to inhomogeneous and nonspherical particles: Key relationships and conversions, J. Atmos. Sci., 68, 1460–1473, https://doi.org/10.1175/2011JAS3645.1, 2011.

Petzold, A., Busen, R., Schröder, F. P., Baumann, R., Kuhn, M., Ström, J., Hagen, D. E., Whitefield, P. D., Baumgardner, D., Arnold, F., Borrmann, S., and Schumann, U.: Near-field measurements on contrail properties from fuels with different sulfur content, J. Geophys. Res. Atmos., 102, 29 867–29 880, https://doi.org/10.1029/97JD02209, 1997.

Platnick, S., Meyer, K. G., King, M. D., Wind, G., Amarasinghe, N., Marchant, B., Arnold, G. T., Zhang, Z., Hubanks, P. A., Holz, R. E., Yang, P., Ridgway, W. L., and Riedi, J.: The MODIS cloud optical and microphysical products: Collection 6 updates and examples from Terra and Aqua, IEEE Trans. Geosci. Remote. Sens., 55, 502–525, https://doi.org/10.1109/TGRS.2016.2610522, 2017.

Quaas, J., Gryspeerdt, E., Vautard, R., and Boucher, O.: Climate impact of aircraft-induced cirrus assessed from satellite observations before and during COVID-19, Environ. Res. Let., 16, 064 051, https://doi.org/10.1088/1748-9326/abf686, 2021.

Ramanathan, V., Cess, R. D., Harrison, E. F., Minnis, P., Barkstrom, B. R., Ahmad, E., and Hartmann, D.: Cloud-radiative forcing and climate: Results from the Earth radiation budget experiment, Science, 243, 57–63, http://www.jstor.org/stable/1703174, 1989.

Rémillard, J., Kollias, P., Luke, E., and Wood, R.: Marine boundary layer cloud observations in the Azores, J. Clim., 25, 7381–7398, https://doi.org/10.1175/JCLI-D-11-00610.1, 2012.

Sanz-Morère, I., Eastham, S. D., Allroggen, F., Speth, R. L., and Barrett, S. R. H.: Impacts of multi-layer overlap on contrail radiative forcing, Atmos. Chem. Phys., 21, 1649–1681, https://doi.org/10.5194/acp-21-1649-2021, 2021.

Sassen, K.: Contrail-cirrus and their potential for regional climate change, Bull. Am. Meteorol. Soc., 78, 1885–1904, https://doi.org/10.1175/1520-0477(1997)078<1885:CCATPF>2.0.CO;2, 1997.

Sassen, K. and Campbell, J. R.: A midlatitude cirrus cloud climatology from the facility for atmospheric remote sensing. Part I: macrophysical and synoptic properties, J. Atmos. Sci., 58, 481–496, https://doi.org/10.1175/1520-0469(2001)058<0481:AMCCCF>2.0.CO;2, 2001.

Sassen, K., Wang, Z., and Liu, D.: Global distribution of cirrus clouds from CloudSat/Cloud-Aerosol Lidar and Infrared Pathfinder Satellite Observations (CALIPSO) measurements, J. Geophys. Res. Atmos., 113, D00A12, https://doi.org/10.1029/2008JD009972, 2008.

Schröder, F., Kärcher, B., Duroure, C., Ström, J., Petzold, A., Gayet, J.-F., Strauss, B., Wendling, P., and Borrmann, S.: On the transition of contrails into cirrus clouds, J. Atmos. Sci., 57, 464–480, https://doi.org/10.1175/1520-0469(2000)057<0464:OTTOCI>2.0.CO;2, 2000.

Schulz, J.: On the effect of cloud inhomogeneity an area averaged radiative properties of contrails, Geophys. Res. Lett., 25, 1427–1430, https://doi.org/10.1029/98GL51098, 1998.

Schumann, U.: On conditions for contrail formation from aircraft exhausts, Meteorologische Zeitschrift, 5, 1996.

Schumann, U.: A contrail cirrus prediction model, Geosci. Model Dev., 5, 543–580, https://doi.org/10.5194/gmd-5-543-2012, 2012.

Schumann, U. and Heymsfield, A. J.: On the life cycle of individual contrails and contrail cirrus, Meteorol. Monogr., 58, 3.1–3.24, https://doi.org/10.1175/AMSMONOGRAPHS-D-16-0005.1, 2017.

Schumann, U., Mayer, B., Gierens, K., Unterstrasser, S., Jessberger, P., Petzold, A., Voigt, C., and Gayet, J.-F.: Effective radius of ice particles in cirrus and contrails, J. Atmos. Sci., 68, 300–321, https://doi.org/10.1175/2010JAS3562.1, 2011.

Schumann, U., Mayer, B., Graf, K., and Mannstein, H.: A parametric radiative forcing model for contrail cirrus, J. Appl. Meteorol. Clim., 51, 1391–1406, https://doi.org/10.1175/JAMC-D-11-0242.1, 2012.

Schumann, U., Penner, J. E., Chen, Y., Zhou, C., and Graf, K.: Dehydration effects from contrails in a coupled contrail–climate model, Atmos. Chem. Phys., 15, 11 179–11 199, https://doi.org/10.5194/acp-15-11179-2015, 2015.

Schumann, U., Bugliaro, L., Dörnbrack, A., Baumann, R., and Voigt, C.: Aviation contrail cirrus and radiative forcing over europe during 6 months of COVID-19, Geophys. Res. Lett., 48, https://doi.org/https://doi.org/10.1029/2021GL092771, e2021GL092771 2021GL092771, 2021.

Stamnes, K., Tsay, S.-C., Wiscombe, W., and Laszlo, I.: DISORT, a general-purpose Fortran program for discrete-ordinate-method radiative transfer in scattering and emitting layered media: Documentation of methodology., Tech. rep., Stevens Institute of Technology Dept. of Physics and EngineeringPhysics Tech., 2000.

Stapf, J., Ehrlich, A., and Wendisch, M.: Influence of thermodynamic state changes on surface cloud radiative forcing in the Arctic: A comparison of two approaches using data from AFLUX and SHEBA, J. Geophys. Res. Atmos., 126, e2020JD033 589, https://doi.org/10.1029/2020JD033589, 2021.

Stephens, G. L.: Radiation profiles in extended water clouds. II: Parameterization schemes, J. Atmos. Sci., 35, 2123–2132, https://doi.org/10.1175/1520-0469(1978)035<2123:RPIEWC>2.0.CO;2, 1978.

Stephens, G. L., Tsay, S.-C., Stackhouse, P. W., and Flatau, P. J.: The relevance of the microphysical and radiative properties of cirrus clouds to climate and climatic feedback, J. Atmos. Sci., 47, 1742–1754, https://doi.org/10.1175/1520-0469(1990)047<1742:TROTMA>2.0.CO;2, 1990.

Stephens, G. L., Gabriel, P. M., and Tsay, S.-C.: Statistical radiative transport in one-dimensional media and its application to the terrestrial atmosphere, Transp. Theory Stat. Phys., 20, 139–175, https://doi.org/10.1080/00411459108203900, 1991.

Stephens, G. L., Wood, N. B., and Gabriel, P. M.: An assessment of the parameterization of subgrid-scale cloud effects on radiative transfer. Part I: Vertical overlap, J. Atmos. Sci., 61, 715–732, https://doi.org/10.1175/1520-0469(2004)061<0715:AAOTPO>2.0.CO;2, 2004.

Stevens, B. and Bony, S.: What are climate models missing?, Science, 340, 1053–1054, https://doi.org/10.1126/science.1237554, 2013.

Stevens, B., Farrell, D., Hirsch, L., Jansen, F., Nuijens, L., Serikov, I., Brügmann, B., Forde, M., Linne, H., Lonitz, K., and Prospero, J. M.: The Barbados Cloud Observatory: Anchoring investigations of clouds and circulation on the edge of the ITCZ, Bull. Am. Meteorol. Soc., 97, 787–801, https://doi.org/10.1175/BAMS-D-14-00247.1, 2016.

Strauss, B., Meerkötter, R., Wissinger, B., Wendling, P., and Hess, M.: On the regional climatic impact of contrails: microphysical and radiative properties of contrails and natural cirrus clouds, Ann. Geophys., 15, 1457–1467, https://doi.org/10.1007/s00585-997-1457-4, 1997.

Stuber, N., Forster, P., Rädel, G., and Shine, K.: The importance of the diurnal and annual cycle of air traffic for contrail radiative forcing, Nature, 441, 864—867, https://doi.org/10.1038/nature04877, 2006.

Takano, Y. and Liou, K.-N.: Solar radiative transfer in cirrus clouds. Part I: Single-scattering and optical properties of hexagonal ice crystals, J. Atmos. Sci., 46, 3–19, https://doi.org/10.1175/1520-0469(1989)046<0003:SRTICC>2.0.CO;2, 1989.

Unterstrasser, S. and Stephan, A.: Far field wake vortex evolution of two aircraft formation flight and implications on young contrails, The Aeronaut. J., 124, 667—702, https://doi.org/10.1017/aer.2020.3, 2020.

van de Hulst, H. C.: Light scattering by small particles, Courier Corporation, first edn., 1981.

van Diedenhoven, B., Fridlind, A. M., Ackerman, A. S., Eloranta, E. W., and McFarquhar, G. M.: An evaluation of ice formation in large-eddy simulations of supercooled Arctic stratocumulus using ground-based lidar and cloud radar, J. Geophys. Res. Atmos., 114, https://doi.org/10.1029/2008JD011198, 2009.

van Diedenhoven, B., Cairns, B., Geogdzhayev, I. V., Fridlind, A. M., Ackerman, A. S., Yang, P., and Baum, B. A.: Remote sensing of ice crystal asymmetry parameter using multi-directional polarization measurements – Part 1: Methodology and evaluation with simulated measurements, Atmos. Meas. Tech., 5, 2361–2374, https://doi.org/10.5194/amt-5-2361-2012, 2012.

Wang, Y., Yang, P., Hioki, S., King, M. D., Baum, B. A., Di Girolamo, L., and Fu, D.: Ice cloud optical thickness, effective radius, and ice water path inferred from fused MISR and MODIS measurements based on a pixel-level optimal ice particle roughness model, J. Geophys. Res. Atmos., 124, 12 126–12 140, https://doi.org/10.1029/2019JD030457, 2019.

Wendisch, M., Yang, P., and Pilewskie, P.: Effects of ice crystal habit on thermal infrared radiative properties and forcing of cirrus, J. Geophys. Res. Atmos., 112, D08 201, https://doi.org/10.1029/2006JD007899, 2007.

Wilber, A. C.: Surface emissivity maps for use in satellite retrievals of longwave radiation, NASA, https://ntrs.nasa.gov/citations/19990100634, last access: 16 January 2023, 1999.

Wolf, K., Bellouin, N., and Boucher, O.: Simulated top-of-atmosphere (15 km) downward and upward solar and thermal-infrared irradiances and ice cloud optical thickness; calculated solar, TIR and net cloud radiative effect. Simulated with ice crystal properties for aggregates, droxtals, and plates based on Yang (2000)., https://doi.org/10.5281/zenodo.7593464, 2023a.

Wolf, K., Bellouin, N., and Boucher, O.: Simulated top-of-atmosphere (15 km) downward and upward solar and thermal-infrared irradiances and ice cloud optical thickness; calculated solar, TIR and net cloud radiative effect. Simulated with ice crystal properties for aggregates, droxtals, and plates based on Yang (2000)., https://doi.org/10.5281/zenodo.7918443, 2023b.

Wylie, D. P. and Menzel, W. P.: Eight years of high cloud statistics using HIRS, J. Climate, 12, 170–184, https://doi.org/10.1175/1520-0442(1999)012<0170:EYOHCS>2.0.CO;2, 1999.

Yang, P. and Fu, Q.: Dependence of ice crystal optical properties on particle aspect ratio, J. Quant. Spectrosc. Radiat. Transfer, 110, 1604–1614, https://doi.org/10.1016/j.jqsrt.2009.03.004, 2009.

Yang, P., Liou, K. N., Wyser, K., and Mitchell, D.: Parameterization of the scattering and absorption properties of individual ice crystals, J. Geophys. Res. Atmos., 105, 4699–4718, https://doi.org/10.1029/1999JD900755, 2000.

Yang, P., Baum, B. A., Heymsfield, A. J., Hu, Y. X., Huang, H.-L., Tsay, S.-C., and Ackerman, S.: Single-scattering properties of droxtals, J. Quant. Spectrosc. Radiat. Transfer, 79–80, 1159–1169, https://doi.org/10.1016/S0022-4073(02)00347-3, 2003.

Yang, P., Wei, H., Huang, H.-L., Baum, B. A., Hu, Y. X., Kattawar, G. W., Mishchenko, M. I., and Fu, Q.: Scattering and absorption property database for nonspherical ice particles in the near- through far-infrared spectral region, Appl. Opt., 44, 5512–5523, https://doi.org/10.1364/AO.44.005512, 2005.

Yang, P., Hong, G., Dessler, A. E., Ou, S. S. C., Liou, K.-N., Minnis, P., and Harshvardhan: Contrails and induced cirrus: optics and radiation, Bull. Am. Meteorol. Soc., 91, 473–478, https://doi.org/10.1175/2009BAMS2837.1, 2010.

Yang, P., Bi, L., Baum, B. A., Liou, K.-N., Kattawar, G. W., Mishchenko, M. I., and Cole, B.: Spectrally consistent scattering, absorption, and polarization properties of atmospheric ice crystals at wavelengths from 0.2 to 100 μm, J. Atmos. Sci., 70, 330–347, https://doi.org/10.1175/JAS-D-12-039.1, 2013.

Zhang, Y., Laube, M., and Raschke, E.: Numerical simulations of cirrus properties, Contrib. Atmos. Phys., 67, 109–120, 1994.

Zhang, Y., Macke, A., and Albers, F.: Effect of crystal size spectrum and crystal shape on stratiform cirrus radiative forcing, Atmos. Res., 52, 59–75, https://doi.org/10.1016/S0169-8095(99)00026-5, 1999.